Title

Nanoparticle Matter: Synthesis, Characterization, Control, and Application of YSZ, CZTS, and ZrN

Author

Exarhos, Stephen Anthony

Publication Date

2018

UNIVERSITY OF CALIFORNIA
RIVERSIDE

Nanoparticle Matter: Synthesis, Characterization, Control, and Application of YSZ, CZTS, and ZrN

A Dissertation submitted in partial satisfaction
of the requirements for the degree of

Doctor of Philosophy

in

Mechanical Engineering

by

Stephen Exarhos

September, 2018

Dissertation Committee:
  Dr. Lorenzo Mangolini, Chairperson
  Dr. Suveen Mathaudhu
  Dr. Sinisa Coh

The Dissertation of Stephen Exarhos is approved:

Committee Chairperson

University of California, Riverside

ACKNOWLEDGEMENTS:

I acknowledge the use of work published previously in the journal **Chemical Communications**, Volume 50, Issue 77 (August, 2014) titled, “Spray Pyrolysis of CZTS Nanoplatelets.” I am the primary contributor for this article, while Dr. Krassimir Bozhilov (University of California, Riverside, Materials Science and Engineering Program, Central Facility for Advanced Microscopy and Microanalysis) and Dr. Lorenzo Mangolini (University of California, Riverside, Department of Mechanical Engineering and Materials Science and Engineering Program) are also acknowledged as contributors.

I also acknowledge the use of work published previously in the journal **RSC Advances**, Volume 7, Issue 41 (May, 2017) titled, “Oxide-Induced Grain Growth in CZTS Nanoparticle Coatings.” I am the primary contributor for this article, while Edgar Palmes and Rui Xu are acknowledged as contributing undergraduate research assistants, and Dr. Lorenzo Mangolini is acknowledged as a contributor.

I also acknowledge financial support provided by Dr. Mangolini via NSF BRIGE award number 1125660, NSF CAREER award number 1351386, and NSF PIRE-SOMBRERO award number 1545852.

DEDICATION:

To my partner, my wife, my best friend, M: You are grounded so deeply in the Earth, and your torus is always big enough for me to find my root. Allusions aside, the strength you have to not only carry so many talents in science and art but to carry our relationship as well is inspiring, and I am privileged to dedicate my life and my work to you (and the cats).

To my family, a family of Doctors Exarhos (those who aren't there officially have certainly done enough to earn the title): I started out following the same path you laid for me, feeling like a follower and a less-than. This guided me well for the first 25 years of my life, but now I've diverged somewhat and sought my own path where I can craft my work around the identity I've found in just the last several years. Nevertheless, the late and frantic calls demanding "DOES THIS MAKE SENSE??" and the never-ending sets of eyes willing to read a very wordy and over-written and run-on-and-on-and-on first draft put me in the position to succeed, and I attribute a lot of the success outlined in this work to you.

To my advisor: I disagree with you about a lot of things, namely about what is really important as an academic. But I have boundless respect for you as a scientist and the way you encouraged me to succeed in lab. And you were always willing to let me explore my own path in graduate school, which allowed me to keep coaching soccer, and when I couldn't do that anymore, you let me join the graduate school of education "on the side," you let me seek out mentorship and education opportunities, and you let me work in the writing center. You let me, no matter how much you thought I was wasting my time – you could have easily laughed at me and ordered me back into the lab. For this I am grateful.

To my colleagues with whom I’ve worked closely and not so closely with over the years: I ascribe my professional identity to our interactions – the good and the bad. And in truth, very few of the results I discuss in this dissertation would be possible without your input or your curiosity. I built my identity around the ideas of mutual respect and collegiality, and I hope I have had even a small amount of the impact on your lives as you have had on mine.

To everyone else, you know who you are, and I am privileged and honored to have had your support.

ABSTRACT OF THE DISSERTATION

Nanoparticle Matter: Synthesis, Characterization, Control, and Application of YSZ, CZTS, and ZrN

by

Stephen Exarhos

Doctor of Philosophy, Graduate Program in Mechanical Engineering
University of California, Riverside, September, 2018
Dr. Lorenzo Mangolini, Chairperson

As a material is reduced down to sub-100 nm dimensions, its interaction with light, with heat, and with other matter changes due in part to increased confinement of free charges and to an increased surface area relative to volume. In practice, different materials and their characteristics can be tuned to control bulk-system properties like optical transparency, free charge generation, electric field enhancement, and localized thermal enhancement. In this dissertation, I will discuss the controlled synthesis and characterization of three different nanoparticle material systems: yttria-stabilized zirconia (YSZ), copper-zinc-tin-sulfide (CZTS), and zirconium nitride (ZrN). I will additionally discuss the viability of using the produced materials in proposed applications, namely: YSZ as the basis material for transparent sintered ceramic disks for use as cranial implants; CZTS as the basis material for earth-abundant, inexpensive, polycrystalline thin film photovoltaics; and ZrN as a visible spectrum plasmonic absorbing material for use in light-induced localized field enhancement applications.

Table of Contents

List of Figures

Chapter 1: Introduction

Chapter 2: Synthesis and Characterization of YSZ Nanoparticles

Chapter 3: Review of CZTS and Photovoltaic Literature

Chapter 4: CZTS Synthesis

Chapter 5: *In Situ* Raman Characterization of CZTS Nanoparticle Sintering

Chapter 6: Zirconium Nitride Nanoparticle Synthesis and Characterization

List of Tables

Chapter 2: Synthesis and Characterization of YSZ Nanoparticles

Chapter 4: CZTS Synthesis

List of Equations

Chapter 2: Synthesis and Characterization of YSZ Nanoparticles

Chapter 3: Review of CZTS and Photovoltaic Literature

Chapter 5: *In Situ* Raman Characterization of CZTS Nanoparticle Sintering

Chapter 1: Introduction

1.1: Importance of Nanotechnology

Why is important to make things small? In the most basic sense, making things small makes them more practical. Take, for example, the evolution of the computer in the last 70 years. We now have more computing power in our pockets than could then be crammed into large buildings. This is due in part to engineering complex and ingenious data management and storage schemes, but in equally significant part to the miniaturization of solid state electronics. For decades, scientists and engineers reduced the size of silicon-based transistors from 10s of µm to 10s of nm,[1] with the Intel Corporation now producing 14-nm transistors, while even smaller devices are already in advanced-stage development. Scientific research has facilitated this development in accordance with "Moore's Law" — which predicts that every year the number of transistors produced on a chip would double [2] — by introducing new processing techniques allowing the shrinking of material features, by implementing new transistor geometries, and by introducing new materials to replace or enhance silicon.[1]

In the same time, scientists have developed a strong understanding of how physical characteristics of materials change with a reduction to the nanoscale through the application of complex characterization techniques and computationally demanding theoretical models. Mankind, however, has leveraged nanoscale science for much longer than we have been able to comprehend it. One of the most alluring examples — to nano-scale scientists, at least — of humans leveraging nanotechnology is the Lycurgus Cup, a goblet dated to the fourth century A.D. from the Roman Empire.[3] Not only is the artistic detail in this goblet fascinatingly detailed, the glass used in the cup is dichroic, *i.e.* its color appears different depending on the direction of illumination. The goblet appears an opaque green under standard lighting conditions, but if illuminated from the inside, it appears translucent red (Fig. 1). The dichroic character of the glass is attributed to inclusions of metal alloy nanoparticles consisting of ~30% gold, ~70% silver, and minute inclusions of copper and antimony.[3] Though the inclusion of these meals was intentional, the process appears to have been very difficult to control, indicating a limited understanding of the physics of the system.[3]

In the mid-19th century, Michael Faraday called for intense studies on the interactions of gold and other metal nanomaterials with light.[4] Faraday, a self-professed staunch experimentalist, had developed a repeatable chemical synthesis technique for the production of colloidal gold nanoparticles.[4] Faraday also observed that upon thinning

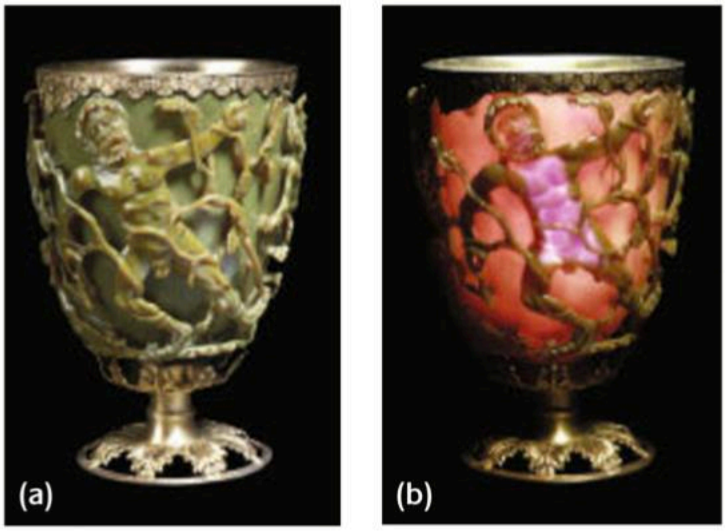

Figure 1: Image of Lycurgus Cup using (a) direct illumination and (b) transmission illumination. Image from Freestone et al.,[3] © British Museum.

gold foil to ~1 µm by his estimation (in reality it was likely around an order of magnitude thinner), the material no longer appeared like the foil he started with; it transmitted green light, reflected yellow light, and absorbed some light.[4] Faraday also observed that changing the composition of the foil by introducing some silver as an alloy in turn changed the colors of light he observed through the thinned foil.[4] Over the course of the next century through the application of Maxwell's new theories on electromagnetism to confined nanoscale systems with a given concentration of bound free charges, physicists developed models to describe why interactions with light are different for nanomaterials than for their bulk counterparts.

In 1959, Richard Feynman gave his seminal lecture calling for yet more investigations on nanoscale materials, noting that the technology did already exist to both produce and characterize nanoscale materials, but there had not yet been a concerted effort aimed at developing the science.[5] Since then, experimental and theoretical techniques both of contributed to our understanding of a very simple but powerful principle: materials with sizes less than ~100 nm exhibit different properties than their larger counterparts. This is primarily due to the particles being smaller than the wavelengths associated with visible light (~400-700 nm), and to the increase in significance of surface science effects as the surface area (~r^2) to volume (~r^3) ratio increases with a reduction in size (~r). This, in turn, leads to changes in optical, mechanical, chemical, electronic, and thermodynamic properties in different nanomaterials.

1.2: Nanoparticle Synthesis Techniques

Nanoparticles can be produced using a variety of techniques, including chemical, electrodynamic, mechanical, and radiative processes. In general, these techniques fall into two categories: “bottom-up” production or “top-down” production. In a top-down process, nanoparticles are produced by breaking apart large pieces of a material into smaller pieces. This can be done by mechanical milling, ablation, explosion, or lithographic techniques, to name a few. Material produced using these techniques is rarely useful for practical nanoparticle science. Particles are often produced with either a very large size inhomogeneity — sometimes spanning three orders of magnitude, or a very small rate of production. Mechanical milling is an attractive technique because it is efficient in these regards; however it is difficult to process very fine particles because the mechanical process depends on the milling media — commonly cubic zirconia or stainless steel balls. Further, the milling is a thermal attrition process; it is difficult to balance crystal grain-refining dynamics with crystal grain-growth dynamics in this kind of process. Lithography or lithographic etching are also attractive, though it is limited in size resolution and in the breadth of materials that may be processed.

Bottom up approaches are desirable for controllably producing sub-100 nm particles with desired properties. In these processes, particles are synthesized chemically at the atomic scale and grown to reach the desired nanoparticle state. Solution-based processes are the most common methods for nanoparticle synthesis in this manner, in which a reaction is controlled based on molecular structure and intermolecular chemistry and thermodynamic energy. Michael Faraday’s gold particle sols (Fig. 2) are a prime

Figure 2: Image of gold colloid solution produced by Michael Faraday in 1857. Credit: Paul Wilkinson via The Royal Institution, 2014.

example of material produced via this kind of technique.[4] These processes are generally limited by temperature — reaction temperatures cannot exceed those that would volatilize the solvent medium. This limits the utility of these processes for high-energy materials like ceramics.

To alleviate limiting factors like those in solution-based processes, vapor-phase techniques are commonly applied in nanoparticle synthesis. Of these techniques, spray pyrolysis is the best known, having been used to commercially produce ceramic oxide nanoparticles for the last several decades. In spray pyrolysis, a solution consisting generally of metal-salt precursors dissolved in a solvent is aerosolized into fine droplets. This aerosol is flowed through a thermal region, in which the solvent in each droplet evaporates, the precursor molecules decompose, and the desired material nucleates thermodynamically. This is an extremely practical process, as it can be operated in air at atmospheric pressure.

Additional vapor-phase techniques include plasma processes. The electronic energy accessible in a plasma, a state of matter in which electrons have been stripped from atoms to generate a sustained slurry of charged species, allows for an additional mechanism of energy delivery that can be used to process precursor molecules. The most widely recognizable mechanism of material processing by plasma exists in stars, in which there is substantial thermal energy generated from the chemical and electronic interactions associated with fusion. In this kind of thermal plasma, electrons and ions exist in thermodynamic equilibrium, meaning there is a comparable amount of energy in both the electrons and ions constituting the plasma. Plasmas can also be generated in non-equilibrium conditions, in which the electrons are highly energetic and the ions are not. These are termed non-thermal or non-equilibrium plasmas. This kind of plasma is applied in fluorescent lamps, in which a non-thermal plasma is excited to generate light from atomic ionization and recombination and electron energy transitions, while the fixture remains at or only slightly above room temperature.

Non-thermal plasmas have been used to produce high-thermal stability materials like silicon, silicon carbide, graphitic carbon, germanium, zinc oxide, titanium nitride, and more using an effectively room-temperature process. The electrostatic charge that builds up on the surface of particles produced by non-thermal plasmas limits crystal growth above a critical value (contingent on the chemical reaction and ambient parameters), and electrostatically repels particles from each other, preserving their structure after production.

1.3: Nanoparticle Characterization

Nanoparticle characterization techniques are equally as crucial as synthesis techniques. With effective characterization techniques, ancient Romans may have been able to refine the production of dichroic glasses like that used in the Lycurgus Cup. Experimental nanoparticle scientists now must characterize material structure, morphology, optical properties, mechanical properties, etc. in order to validate the synthesis and viability of different material systems in proposed applications, or to demonstrate new fundamental nanoscale properties.

Nanoparticle characterization is a significant challenge, because visible light-based techniques are often insufficient in resolving physical features smaller than the wavelength of the light. For this reason, high-energy electromagnetic waves like X-Rays and electron beams with sub-nanometer wavelengths are used to characterize nanomaterials morphologically, compositionally, chemically, and structurally. Visible and near-infrared light can be used to probe different material properties, like atomic bond frequencies in crystals, optical absorption and scattering, and electrical transition energies. Not only are there a broad variety of nanoparticle characterization techniques, each technique can be applied in different ways to yield different information about different properties of nanoscale material. For example, the electron beam utilized in transmission electron microscopy can be use not only to characterize the morphology of features down to sub-nm dimensions, it can be used to generate a diffraction pattern to provide structural information, and it can be used to quantify atomic composition as well.

1.4: Dissertation Direction

In this dissertation, I will discuss the synthesis, characterization, control, and proposed applications for three different nanoparticle material systems: yttria-stabilized zirconia (YSZ), copper-zinc-tin-sulfide (CZTS), and zirconium nitride (ZrN).

I developed an atmospheric pressure process for the synthesis of YSZ and CZTS nanoparticles based on the scalable and well-studied technique aerosol spray pyrolysis. This process allows for the production of nanoparticles without the need for organic ligands that are used in many solution-based processes, which is important for these two material systems in their proposed applications. In my system a precursor solution composed generally of some metal-salts dissolved in a solvent is aerosolized and passed through a furnace at high temperature. Within the furnace, the solvent is evaporated, and the precursor molecules in each droplet thermally decompose and coalesce into the desired nanoparticle material. This system is not especially novel in any regard, but it allows me to synthesize a broad variety of nanoparticle materials with relative ease — with this system I have made CZTS, YSZ, SnS_2, Cu_2S, ZnS, MoS_2, WS_2, ZnO, NiO, and Al_2O_3 nanoparticles as well as different heterostructured-nanoparticle materials (core/shell, yolk/shell, and highly-porous scaffold particles) simply by varying the precursor solution used and optimizing the processing temperature and carrier gas flow rate.

In Ch. 2, I introduce my optimized spray pyrolysis technique for the mass-production of YSZ nanoparticles with sub-10 nm crystallite size at a rate of ~100 mg/hr. The technique provides straightforward control of the yttria-dopant content in the zirconia material system, which in turn allows the tuning of structural, mechanical, and optical properties. In this project, the nanoparticles are intended to be the basis material for transparent sintered YSZ disks for use in biomedical applications. Optical transparency in this material is dependent primarily on the crystal grain size, with smaller crystal grains leading to increased transparency in the bulk sintered disk. Control of crystal size, morphology, yttria-dopant concentration, and organic contamination in the synthesis and post-processing of this material have been extensively characterized to demonstrate the viability of this material in the proposed application.

I have also applied the spray pyrolysis system to produce CZTS nanostructures with controllable composition, morphology, and structure, as discussed in Ch. 3 and Ch. 4. This material is of interest to the photo-energy conversion community due to its high absorption coefficient and band gap that aligns well with the energy spectrum of the sun. The constituent materials are also inexpensive, earth-abundant, and non-toxic. CZTS in nanoparticle form is of interest primarily for use in scaled-up photovoltaic device processing. The nanoparticles may be incorporated into a printable ink, which guarantees the compatibility of the material with a roll-to-roll printing platform enabling large-area, low-cost fabrication of photovoltaic panels. My work demonstrates a scalable technique for the processing of CZTS nanoparticles into uniform large-grain CZTS thin films for eventual use as absorber layers in thin film photovoltaic devices.

Starting from coatings of organic-ligand-free CZTS nanoparticles produced by the spray pyrolysis process, I demonstrate control over defect and morphology characteristics during thermal annealing in a low-pressure sulfur atmosphere via the incorporation of sodium or oxygen at the nanoscale-level. The omission of organic ligands in the nanoparticle synthesis process eliminates the formation of graphitic-carbon aggregates in the film during thermal annealing that are commonly observed in the field.

I additionally showcase in Ch. 5 a novel apparatus for the *in situ* characterization of this material during thermal processing via *in situ* Raman spectroscopy, which allows an understanding of how the material structure and disorder evolves during the annealing process contingent on processing parameters. This technique is unique and provides a viable facsimile of the sulfur annealing process, which is unattainable using standard *in situ* characterization stages. My technique, in conjugation with other work describing theoretical and *ex situ* characterization of the material during the sulfur annealing process allows for the refinement of the processing parameters to optimize the material properties for use in photovoltaic devices.

In Ch. 6, I introduce the scientifically-exciting but as yet under-explored material, plasmonic ZrN nanoparticles. This material is difficult to synthesize using thermal techniques, requiring temperatures above 1,200 ºC, but I have developed a non-thermal plasma process to synthesize the material effectively at room temperature, making experimental studies of the material's plasmonic properties attainable. ZrN not only is a refractory ceramic material that has been used in aerospace applications for highly-mechanically stable coatings, but it also possesses a high free-electron density, making it behave electronically similar to conductive metals. When reduced to the nanometer-scale, this metal-like character translates to a localized surface plasmon resonance (LSPR) in the visible spectrum, similar to the phenomenon that has been long observed in gold and silver nanoparticles. I confirm that the material produced exhibits LSPR in the visible spectrum, though the resonance exists at a lower energy than predicted by Mie Theory modeling. I attribute this discrepancy to partial oxidation of the material and have developed a method to reduce the oxidation and push the LSPR closer to that which has been theoretically predicted. I additionally show preliminary data demonstrating the viability of this material system in plasmonics applications including thermo-photovoltaics, localized cellular thermolysis, and surface enhanced Raman scattering to a lesser extent.

1.5: References

(1) Thompson, S. E.; Parthasarathy, S. Moore's Law: The Future of Si Microelectronics. *Materials Today*, **2006**, *9*(6), 20-25.

(2) Moore, G. E. Cramming More Components onto Integrated Circuits. *Proceedings of the IEEE*, **1998**, *86*(1), 82-85.

(3) Freestone, I.; Meeks, N.; Sax, M.; Higgitt, C. The Lycurgus Cup — A Roman Nanotechnology. *Gold Bulletin*, **2007**, *40*(4), 270-277.

(4) Faraday, M. The Bakerian Lecture: Experimental Relations of Gold (and Other Metals) to Light. *Philosophical Transactions of the Royal Society of London*, **1857**, *147*, 145-181.

(5) Feynman, R. P. There's Plenty of Room at the Bottom. *SPIE MILESTONE SERIES MS*, **2006**, *182*, 3.

Chapter 2: Synthesis and Characterization of YSZ Nanoparticles

2.1: Introduction to the "Window to the Brain"

Yttria stabilized zirconia ($(ZrO_2)_{1-x}(Y_2O_3)_x$; YSZ) is a ceramic material with high mechanical strength, high thermal stability, good biocompatibility properties, and can be made optically translucent or transparent.[1] YSZ has been studied extensively for dental applications, as the material can be used for dental implants or dental restoration with only subtly different color and appearance from teeth.[2] The same properties that make YSZ desirable for dental applications also make it desirable for use in other biological implants in place of bone. In addition, the ability to control optical transparency in the material offers unique capabilities. The work described in this chapter is part of a broad interdisciplinary research effort to design transparent YSZ disks made from sintered YSZ nanoparticles. These disks are studied for potential use as cranial implants, effectively providing non-invasive optical access to the brain, hence, the device is called the "Window to the Brain."

Neurological and trauma-related injuries are common — it is estimated that approximately 1.7 million people sustain a traumatic brain injury (TBI) each year,[3] while much of the brain's function and utility as an organ remains poorly understood.[4] In current medical practice, titanium is the material of choice for synthetic bone implants, including craniotomy,[5-7] however these devices are purely structural; they impede efforts at characterization and diagnosis of TBIs. A transparent cranial implant would allow physicians and neurologic-researchers to monitor, diagnose, and potentially treat different brain-related maladies like TBI without invasive cranial excisions required beyond an initial surgery to install the implant.

My collaborators have successfully fabricated translucent YSZ disks using a technique called current-activated pressure-assisted densification (CAPAD).[8] This technique applies a very high pressure and temperature to a compacted puck of nanoparticles in order to sinter the particles into a solid, bulk-nanostructured disk. For these disks, a commercial 8-YSZ (meaning $x = 8$ in $(ZrO_2)_{1-x}(Y_2O_3)_x$) powder was used (TOSOH-ZIRCONIA TZ-8Y; Tosoh Corporation). The sintered disks exhibit some optical translucency in the desired range — the "biological transparency window" in which most human soft tissue is transparent, ~700-1,000 nm in wavelength — but further improvement of optical properties is impossible with these commercially acquired nanoparticles.

In bulk-nanostructured YSZ, optical transparency is directly correlated with crystal grain size.[9] The basis powder material used in previous studies has a pre-sintered crystal grain size of ~50 nm, nearing the upper bound size limit for transparency, and even an optimized sintering procedure results in a small degree of grain growth.[8] Reducing the crystal grain size of the basis YSZ nanoparticles, then, is a solution to improving the optical properties of bulk-sintered disks.[10] As well as crystal grain size, controlling the yttria-dopant composition in YSZ allows for control of mechanical properties in the bulk phase.[10] For the proposed cranial implant application, a high degree of mechanical strength is ideal. In effect, higher compositions of yttria lead to reduced mechanical hardness.

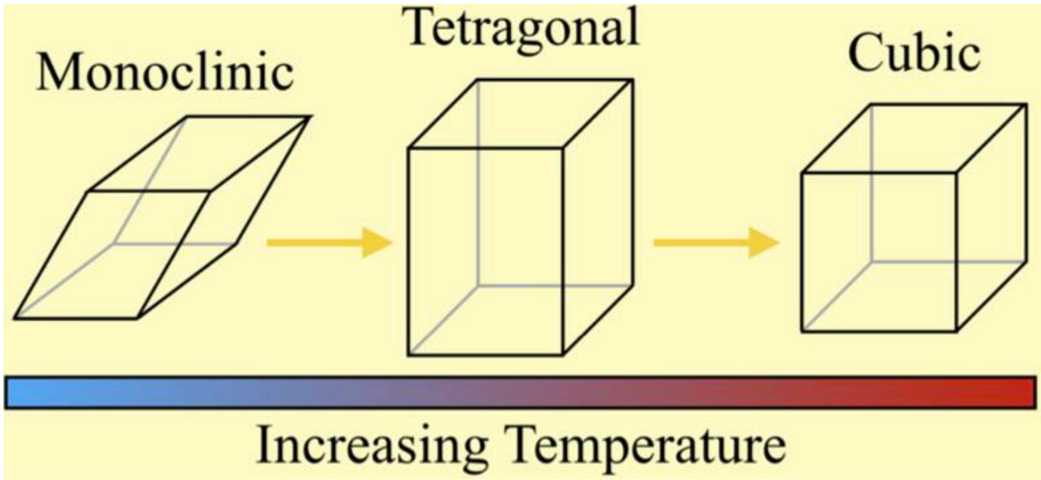

Figure 1: Schematic representation of the three stable crystal structure configurations of YSZ. The temperature bar is intended to show that monoclinic phase has the lowest energy equilibrium stability, followed by tetragonal phase, followed by cubic phase with the highest energy equilibrium stability.

A final characteristic of YSZ that must be carefully controlled is the crystalline phase. ZrO_2 may exist in any of three stable phases: monoclinic, tetragonal, or cubic (diagrammed in Fig. 1). The monoclinic phase possesses the lowest configuration energy, meaning it is the most likely phase to exist at temperatures up to ~950 ºC. The tetragonal phase possesses the median configuration energy, having equilibrium stability between 950 ºC and 1,150 ºC. The cubic phase possesses the highest configuration energy, having equilibrium stability above 1,150 ºC.[11] Mechanical and optical properties correlate with crystal structure as well, with the cubic phase possessing the highest mechanical strength and the best potential for achieving optical transparency.[9] Yttria is a common dopant used to synthetically stabilize these high-energy configuration phases with lower thermal equilibria, though with the caveat that increased stabilization leads to a reduction in mechanical hardness.[11] Ultimately, it is necessary to control the yttrium dopant composition, the crystal grain size, and the crystal structure of YSZ nanoparticles in order to fabricate bulk-nanostructured YSZ disks for use as cranial implants with optimal transparency and mechanical hardness.

I have developed a scalable protocol for the controllable synthesis of YSZ nanoparticles using aerosol spray pyrolysis. This technique allows for straightforward control of dopant-composition, crystal structure, and crystal grain size by tuning different parameters during material production (namely relative precursor dilution, carrier gas flow rate, and processing temperature). In the work below, I demonstrate the controlled synthesis of ZrO_2 nanoparticles and three different target dopant compositions of YSZ nanoparticles: 3-YSZ, 6-YSZ, and 8-YSZ . I conclude with a short discussion on the prospect of using this material as the basis for the proposed cranial implant application.

2.2: YSZ Nanoparticle Synthesis

YSZ nanoparticles are synthesized controllably and scalably using aerosol spray pyrolysis. The technique is well known to industry and is commonly used for the mass production of oxide nanoparticles such as zinc oxide, titania, or alumina.[12-15] Spray pyrolysis is a continuous flow process, and this system is operated at atmospheric pressure with a tube furnace as a radiative heat source instead of the commonly used direct flame.[12] In spray pyrolysis, a precursor solution, typically consisting of metal salts dissolved in a solvent, is aerosolized and passed through a heat source. Inside the thermal region, the solvent droplets evaporate, and the precursor molecules thermally decompose to form the desired nanoparticulate material.[12] By varying precursor molecular structure, precursor dilution, precursor solvent, aerosol flow rate, aerosol droplet size, and heat, the composition, structure, morphology, and size of the product material can be controlled.[12]

A schematic of the aerosol spray pyrolysis apparatus used to synthesize the YSZ nanoparticles used in this work is shown in Fig. 2. The proposed application of this work guided my selection of precursor materials and processing conditions. For example, using organic precursor molecules like zirconium acetylacetonate ($Zr(C_5H_7O_2)_4$) and yttrium acetate ($Y(CH_3COO)_3$) yield uniform, small, and highly crystalline YSZ nanoparticles, however the product is contaminated with amorphous carbon, which is a byproduct of the decomposition of the organic molecules. This organic contamination would be detrimental to the processing of transparent bulk-YSZ disks, so an inorganic alternative to these precursors was found.

The YSZ nanoparticles used in this work were synthesized from a precursor solution of anhydrous $ZrCl_4$ (AlfaAesar) and YCl_3*6H_2O (Sigma Aldrich) dissolved in

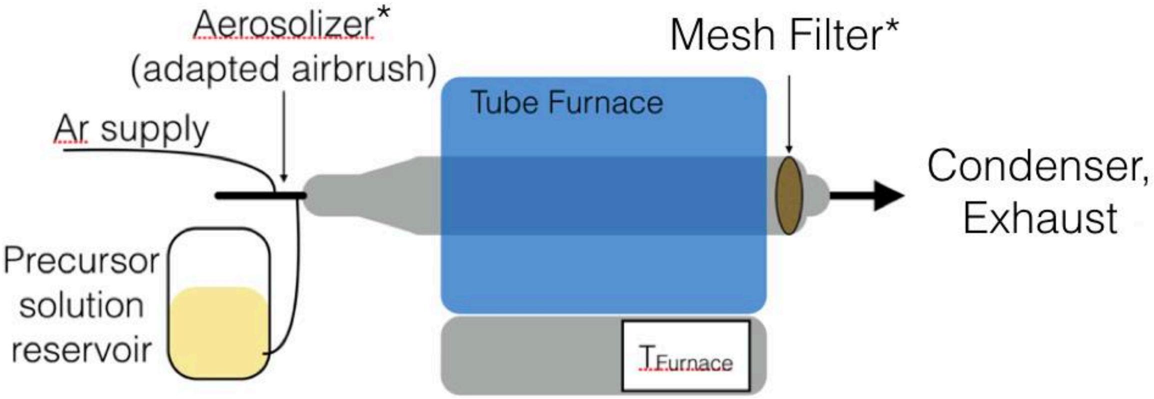

Figure 2: Schematic representation of the aerosol spray pyrolysis apparatus used to synthesis YSZ nanoparticles. Prepared precursor solution is poured into the reservoir, and an argon carrier gas is used to generate an aerosol of the solution. This aerosol is pushed through the furnace at high temperature, within which the solvent evaporates, the precursor molecules decompose, and the desired product is formed. The product is collected on a stainless steel mesh filter.

deionized (DI) water. The product composition is tuned by varying the relative $ZrCl_4$:YCl_3 ratio in the precursor solution. The precursor solution is aerosolized using an argon carrier gas flow of 18 SCFH (7,000 SCCM) through a six-jet Collison-type nebulizer (BGI/Mesa Labs), which generates uniform aerosol droplets of ~5 µm. The droplets are then carried through the 2” diameter tube furnace (MTI OTF-1200X) held at a temperature between 600 and 1,000 ºC, with the given flow rate and atmospheric pressure yielding a residence time inside the furnace on the order of 10^{-1} s. The product is then collected on a stainless steel mesh directly downstream of the furnace, which is cooled to quench the product.

After production, the mesh filter is ultra-sonicated in 50 mL of DI water to collect the powder in suspension. Then, to clean undesired byproducts from the precursor decomposition reaction, the powder is centrifuged at 3,400 RPM for 10 minutes. The supernatant is removed, the powder is re-suspended in DI water, ultra-sonicated for 10 minutes, and centrifuged again. This process is repeated five times. The powder is then suspended once more, transferred to a vial for storage, and dried under air on a hot plate at 120 ºC.

I have developed two post-processing steps to optimize the powder for the eventual sintering of transparent disks. For replication in this work, these processes were included prior to cell culture experiments. First, to reduce any potential carbon contamination or oxygen vacancy defects, the dried powder is annealed in air at 650 ºC for three hours. Second, to reduce agglomeration of the powder resulting from the synthesis process and subsequent thermal treatments, YSZ ball-milling media is added to the powder, and the material is ball milled for 24 hours with a revolution rate of 60 RPM. Following these steps, the powder is characterized and ready for use in further studies.

The YSZ nanoparticle product is characterized with X-Ray diffraction (XRD), transmission electron microscopy (TEM), Raman spectroscopy, and scanning electron microscopy (SEM) with energy dispersive X-Ray spectroscopy (EDS). XRD was performed on a PANalytical Empyrean X-Ray system using Cu Kα radiation with a wavelength of 1.54 Å. TEM was performed using a Tecnai12 instrument with a standard accelerating voltage of 120 kV. Raman measurements were performed with a 532 nm probe laser and a Horiba LabRam HR Raman spectrometer. The power used was 60 mW, the objective used was 100x, the grating was 1,800 lines/mm, and the spectra were acquired for 30 seconds with five averages. SEM was performed on an FEI Nova NanoSEM450 Scanning Electron Microscope equipped with Oxford Instruments Aztec Synergy software and an Oxford Instruments Energy Dispersive X-Ray Spectrometer. Samples were prepared by drop-casting a dense suspension of nanoparticles on copper foil and evaporating the solvent.

2.3: Control of YSZ Nanoparticle Composition, Structure, and Morphology

Being that the intended application of the YSZ nanoparticles discussed in this work is to serve as the basis for sintered polycrystalline disks with optical transparency, there are certain characteristics the powder must possess. To achieve optical transparency in polycrystalline YSZ, the samples must be fully dense, phase pure in either the cubic or tetragonal structure, and maintain uniformly small grain size.[1,9,10] Zirconia can exist stably in three separate crystal structures: monoclinic, tetragonal, and cubic. Cubic zirconia is the highest energy configuration, though it is the most desirable as an optical material – single crystal cubic zirconia is often used as an inexpensive alternative for diamonds in jewelry. To easily produce stable cubic or tetragonal zirconia, the crystal can be doped with other ceramic phases like yttria, ceria, or alumina. These dopants effectively lower the energy configuration of the cubic and tetragonal phases, making them easier to produce.[11] With increasing dopant, the material is more likely to be "fully stabilized" in the pure cubic phase.

Some of the characteristics needed for a polycrystalline YSZ disk to be optically transparent or translucent, like bulk density, are dependent on the nanoparticle sintering process and subsequent post-processing, and so are not considered in detail in this chapter. Instead the nanoparticle material discussed in this work is optimized to have controlled composition with minimal phase inhomogeneity and crystal grain size. This is the fundamental material with which transparent disks can be produced. This section details our control over the production of YSZ nanoparticles.

The composition of the YSZ nanoparticle samples is determined by EDS analysis. I have shown the ability to control the composition – meaning the amount of yttria dopant relative to zirconia – of the samples by changing the relative amount of yttria precursor (YCl_3*6H_2O) relative to zirconia precursor ($ZrCl_4$) in the precursor solution. With the spray pyrolysis system being a thermal process, there is not perfect throughput of precursor into the powder. The precursor molecules inherently require different amounts of energy to decompose, so they will be processed at different rates in the isothermal

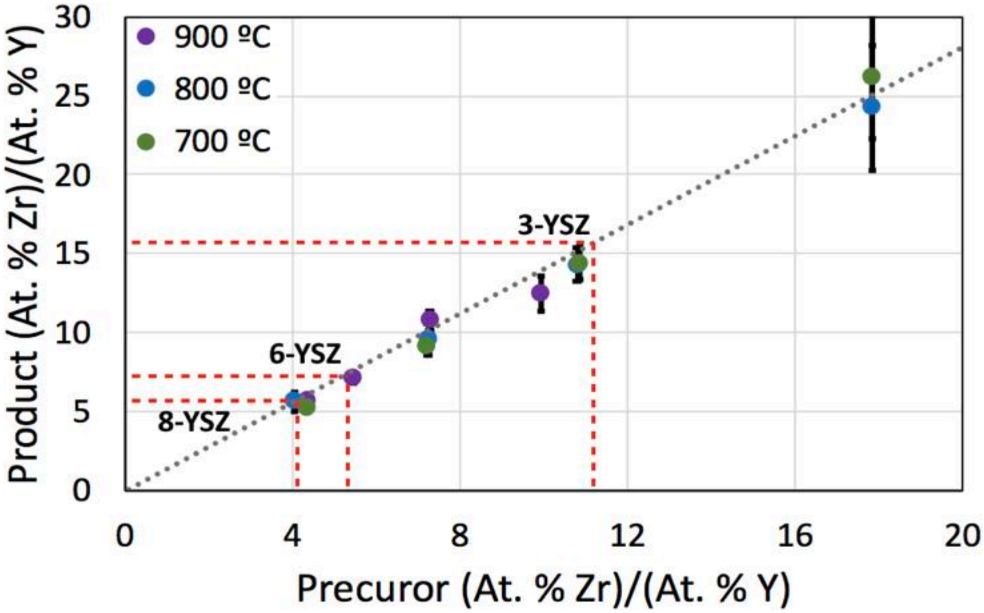

Figure 3: Demonstration of control over yttria-dopant composition in YSZ powder produced using aerosol spray pyrolysis. The vertical axis is the relative atomic ratio of Zr to Y in the product as measured by EDS, and the horizontal axis is the relative atomic ratio of Zr to Y according to the mass of each precursor used. Values are represented at three different temperatures showing the reproducibility of this trend.

reactor. This is indicated in Fig. 3, which shows the atomic ratio of Zr:Y in the produced material (as determined by EDS) against the ratio of Zr:Y in the precursor solution (as determined by precursor masses used). There is a linear trend showing that the addition of more yttria precursor leads to more yttria in the product, but the slope is less than 1. This implies that the processing of YCl_3*6H_2O is less efficient than of $ZrCl_4$. Using a calibration plot like that which is shown in Fig. 3, I am able to extrapolate the precursor composition needed to produce a desired product composition, and I reproducibly produce material with controlled composition.

Fig. 4 shows representative TEM characterization of the YSZ nanoparticle product. Figure 4a shows the material as-produced from the spray pyrolysis system. The

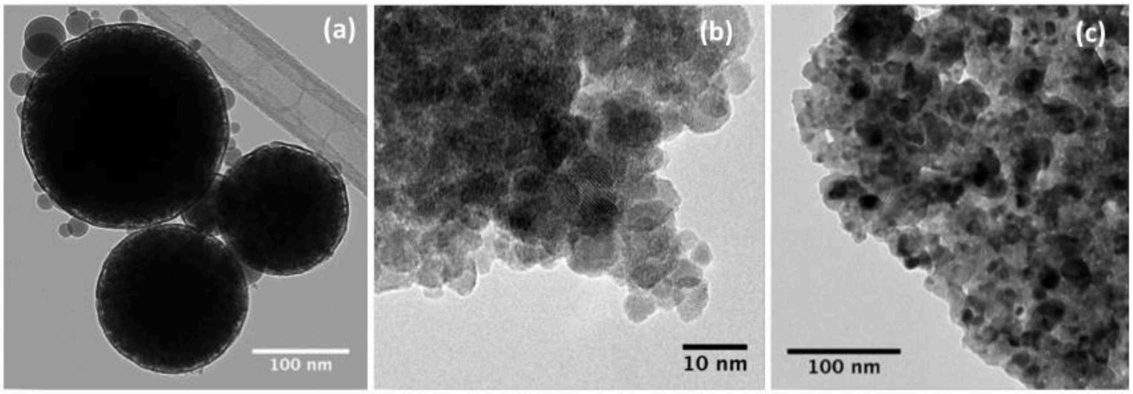

Figure 4: TEM images of YSZ powder. a) Image showing the extent of agglomeration in YSZ powder as-produced from the spray pyrolysis system, prior to any post-production processing. b) High magnification image of dis-agglomerated particles after post-production processing steps, and c) low magnification image of the same.

nanoparticles are agglomerated into large spherical bodies of nonuniform size. This morphology is undesirable for the eventual sintering of fully dense bulk materials. Shown in Figs. 4b and 4c are the nanoparticles as they appear after both air annealing and ball milling. The large spherical agglomerates in Fig. 4a are broken up into loosely packed bodies of distinct monocrystalline nanoparticles, which are clearly distinguishable in the high magnification image in Fig. 4b. This demonstrates the morphology of the material used in the studies in this work.

In XRD, it is difficult to distinguish between the cubic and tetragonal phases of YSZ, particularly when the material has sub-20 nm grain size, as diffraction peaks broaden with decreasing crystallite size. Using the Bragg equation (Eq. 1) to calculate diffraction angles based on standard lattice parameters for cubic phase (a = b = c = 5.090 Å) and tetragonal phase (a = b = 3.595 Å; c = 5.182 Å), cubic and tetragonal planes overlap at the angles indicated in Table 1.

$$2d \sin \theta = n\lambda \qquad \text{(Eq. 1)}$$

Table 1: Comparison of crystal lattice spacing (d) and diffraction angle (2θ) for cubic and tetragonal-phase YSZ.

Cubic YSZ:	$d = \frac{a}{\sqrt{(h^2 + k^2 + l^2)}}$	Diffraction Angle:	*Tet.* YSZ:	$\frac{1}{d^2} = \frac{h^2 + k^2}{a^2} + \frac{l^2}{c^2}$	Diffraction Angle:
(111)	2.94 Å	30.38°	(101)	2.95 Å	30.27°
(200)	2.55 Å	35.16°	(002) (110)	2.59 Å 2.54 Å	34.60° 35.30°
(220)	1.80 Å	50.67°	(112) (200)	1.81 Å 1.80 Å	50.37° 50.67°
(311)	1.53 Å	60.46°	(103) (211)	1.56 Å 1.54 Å	59.18° 60.03°

Here, *n* is the integer number of planes (1 for all planes in the diffraction pattern in Fig. 5a), *λ* is the X-Ray wavelength (Cu Kα is used, *λ*=1.54 Å), *d* is the interplanar spacing, calculated geometrically for different crystal structures (cubic and tetragonal equations for *d* are shown in Table 1), and *θ* is the diffraction angle. In the powder diffraction patterns for all the samples used in this work, the cubic and tetragonal phases are indistinguishable in XRD due to the small size of the crystallites, but all samples are determined to be either cubic or tetragonal phase according to the diffraction pattern, an example of which is shown in Fig. 5a.

From this diffraction pattern, one may also approximate the crystallite size of the sample using the Scherrer approximation derived from the width of the first peak. For the diffraction pattern in Fig. 5a, the crystallite size estimated from the Scherrer equation is ~7.2 nm, which correlates well with the apparent size of the individual particles shown in Fig. 4b, indicating that each nanoparticle is an independent crystal. By changing the composition of the product or changing the temperature used to synthesize the product, I exhibit reasonable control over the crystallite size (Fig. 5b). For all temperatures used, the

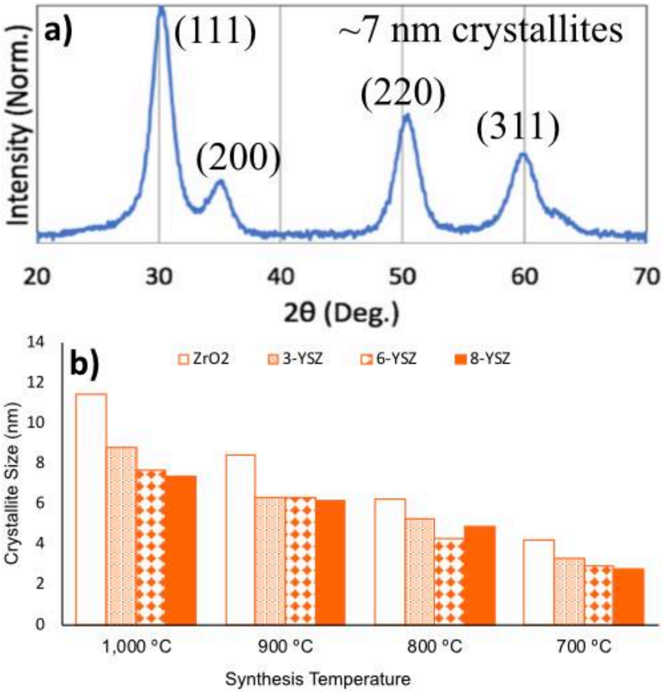

Figure 5: a) Representative XRD pattern of YSZ nanoparticles. This sample appears to be pure cubic-phase YSZ, but it is not a trivial conclusion using solely XRD with particles this small. Scherrer first peak analysis estimates these particles to have an average crystallite size of 7.2 nm. b) Trend in crystallite size as calculated from Scherrer first peak estimation from XRD patterns produced at the four target compositions (ZrO_2, 3-YSZ, 6-YSZ, and 8-YSZ) and at four different temperatures (1,000, 900, 800, and 700 ºC). Crystallite size is controlled from ~3 nm to ~12 nm in these samples.

crystallite size of the product decreases with increasing yttria content, and the crystallite size also decreases with reduced temperatures. However, at reduced temperatures, the precursor processing efficiency is also reduced, meaning less YSZ product is made.

In contrast to XRD, with Raman spectroscopy it is straightforward to distinguish contributions to the scattering spectrum from monoclinic, tetragonal, and cubic-phase zirconia simultaneously. It is more difficult, however, to quantify the phase content and grain size of the material based on a Raman spectrum, though a few statistically valid models have been proposed for deconvolving the relative monoclinic, tetragonal, and cubic-phase contributions to Raman spectra.[16,17]

Fig. 6 shows my ability to control the structure of the produced nanoparticles from approximately fully tetragonal to fully cubic – the two desirable phases for producing bulk transparent/translucent YSZ disks. The nanoparticle samples represented in Fig. 6 were produced under the same conditions except for the precursor solution composition. With increasing yttria content in the powder, I observe a more significant contribution to the Raman spectrum from cubic phase than from tetragonal phase. This trend allows us to make a qualitative estimate of the phase composition of the material based on the peak position between 615 and 640 cm^{-1}. Similar to Kontoyannis and Orkoula [16] and Tabares and Anglada,[17] we can approximate the phase as 100% cubic if

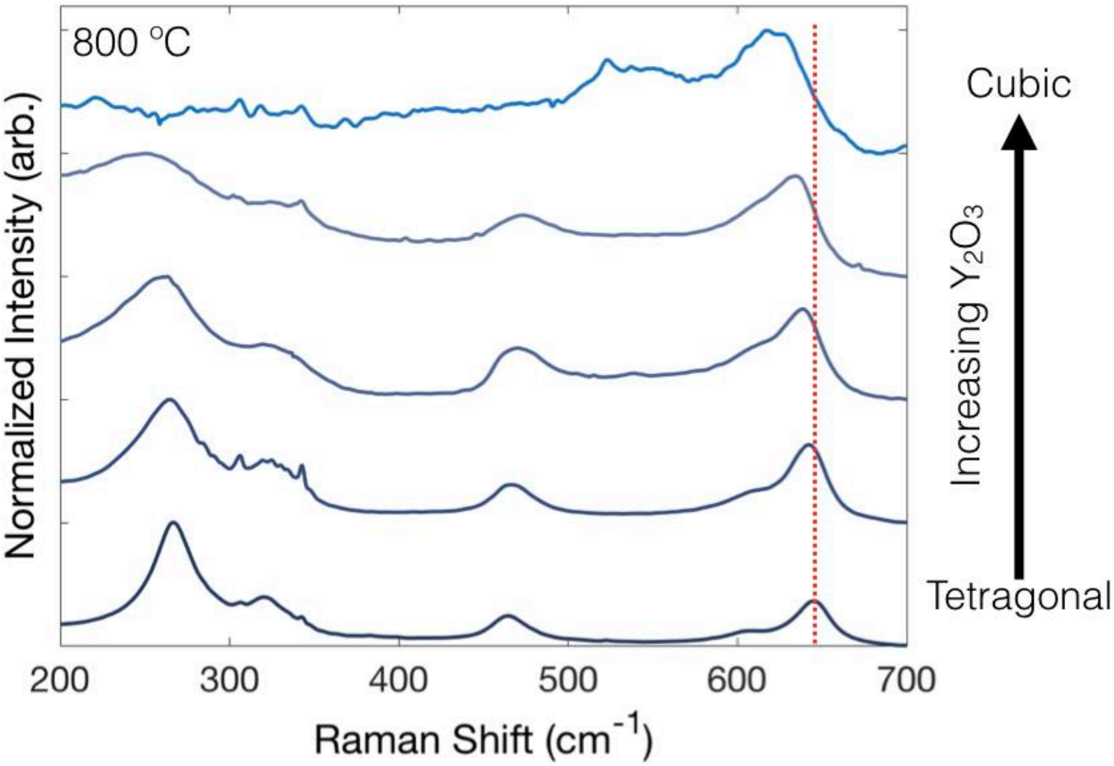

Figure 6: Raman spectra from YSZ nanoparticle samples produced at 800 ºC with varied yttria-composition. With increasing yttria-content, the cubic structure dominates, and with less, the tetragonal structure dominates.

the peak is at 615 cm^{-1}, and 100% tetragonal if the peak is at 640 cm^{-1}, then we can extrapolate the phase composition with the apparent peak position between those two extremes. Ultimately, for optimal optical properties in the implant device it is more important to have phase purity in either fully tetragonal or fully cubic phase to reduce optical scattering,[9] so it is not crucial to quantify the precise phase composition of the material, it will be crucial to identify whether or not the material is phase pure or consisting of mixed phases.

2.4: Conclusions and Prospective Applications of YSZ Nanoparticles

In this chapter, I have demonstrated a high degree of control over the synthesis of YSZ nanoparticles using aerosol spray pyrolysis. EDS indicates control over yttria dopant composition; XRD and Raman demonstrate control over the structure with fine control between tetragonal and cubic phase YSZ; XRD and TEM indicate some control over the particle size between 5 and 20 nm; and TEM indicates that I can produce loosely agglomerated mono-crystalline particles. This degree of control indicates the I can produce material that should be conducive to sintering high-quality bulk-nanostructured YSZ disks with good mechanical and optical properties for the proposed cranial implant application. With the nanoparticle synthesis protocol established, our group and our collaborators will seek to demonstrate the viability of this material in biological systems, and in modestly scaled-up production of high-quality YSZ disks. Below are brief descriptions of preliminary studies by our group and by our collaborators (D. Rutherford and Dr. H. Liu; Bioengineering Department, UCR) working to these goals.

C. Rudnicki (L. Mangolini group; Mechanical Engineering Department, UCR) has made some preliminary attempts at sintering 8-YSZ powder produced using the method described above using spark-plasma sintering. This technique is similar to CAPAD, in that high pressures and high temperatures are applied to a packed puck of powder in order to sinter the particles into a bulk-nanostructured disk. Fig. 7 shows the result from one of these first attempts in which the compacted powder sample was sintered at 1,200 ºC for five minutes with 100 MPa of pressure applied. Fig. 7a and 7b are bright-field microscopy images at 10x magnification of the sample surface after sintering (Fig. 7a) and after polishing the sintered sample (Fig. 7b). The smooth appearance of the

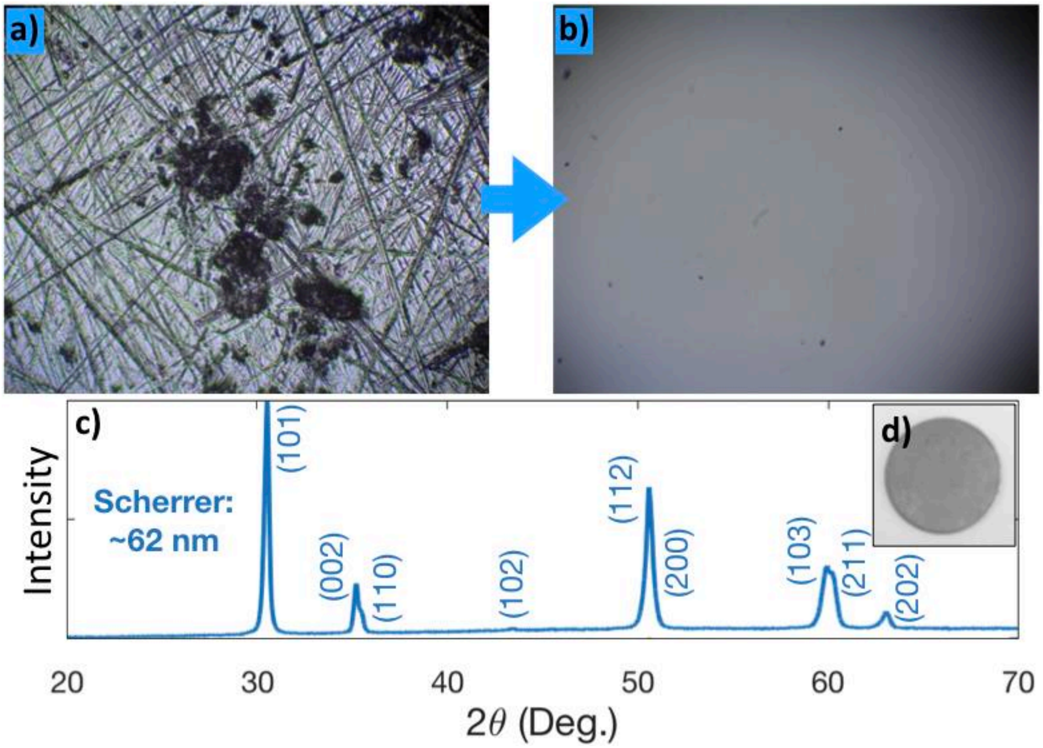

Figure 7: Preliminary data from spark-plasma sintered sample made from 8-YSZ powder produced using the methods described in this work. a) Morphology of the sample after sintering. b) Morphology of the sample after polishing (a). c) XRD pattern of sintered sample showing tetragonal structure and an average crystallite size of 62 nm. d) Image of the sintered sample showing opacity.

sample after polishing suggests the sample is fully dense; a sample with suboptimal density would appear pockmarked and full of voids, similar to the sample as it appears in Fig. 7a. XRD of the sample shows that the particles appear to be phase-pure tetragonal YSZ with an average crystallite size of approximately 62 nm according to the Scherrer first peak estimation (Fig. 7c).

Fig. 7d shows that the sample has negligible optical transparency. There are a few possible explanations for this. The most common factors that are detrimental to optical properties in bulk nanocrystalline YSZ are low density, phase inhomogeneities, defect densities, organic contamination, or birefringence in the crystal structure or crystal orientation.[9] Crystal structure birefringence occurs when a crystal structure has different dimensions along different axes in the unit cell, leading the crystal to have different refractive index values depending on the direction of light propagating through it. Birefringence is commonly observed in tetragonal YSZ, but for crystal grain domains that are sufficiently smaller than the wavelength of the interfering light, this property is negligible, meaning this is not a significant issue in our sample.[9]

The most likely factors contributing to the opacity of our sample are the density, phase purity, and organic contamination.[9] I take precautions to remove organic contamination from both the powder sample and the sintered sample by annealing in air at high temperatures, so I do not anticipate this to be a significant issue, though the sample must be intensively characterized to be certain of this. The sample appears to be highly dense both from visual characterization and from water displacement measurements, though again, further characterization is necessary. The most likely issue is phase impurity in the sample, this sample is likely a combination of cubic and tetragonal phase YSZ. The solid solution of these phases would create a high level of effective optical defects at the boundaries where these phases interact, which would greatly enhance optical scattering and reduce transparency. To solve these issues requires optimization of the sintering process, as the high temperature and pressure conditions applied to the material yield control over the development of the material's crystal structure during processing.

To understand if the material described here can be viable *in vivo* in biological systems, our collaborators have developed a biocompatibility assay to assess the cytotoxicity of the nanoparticles produced. Following extraction and cultivation of the cell culture, the cells are stained with fluorescent proteins, and mixed with varying concentrations of nanoparticles in solution. Cell growth/death is then monitored over the course of 48 hours, and comparison with an appropriate control will allow us to determine if the particles have a toxic effect on the cell culture.

2.5: References

(1) Alaniz, J. E.; Perez-Gutierrez, F. G.; Aguilar, G.; Garay, J. E. Optical Properties of Transparent Nanocrystalline Yttrium Stabilized Zirconia. *Optical Materials*, **2009**, *32*(1), 62-68.

(2) Kim, H.-K.; Kim, S.-H. Optical Properties of Pre-Colored Dental Monolithic Zirconia Ceramics. *Journal of Dentistry*, **2016**, *55*, 75-81.

(3) Langlois, J. A.; Rutland-Brown, W.; Thomas, K. E. Traumatic Brain Injury in the United States; Emergency Department Visits, Hospitalizations, and Deaths. **2006**.

(4) Wilson, N. M.; Gurney, M. E.; Dietrich, W. D.; Atkins, C. M. Therapeutic Benefits of Phosphodiesterase 4B Inhibition after Traumatic Brain Injury. *PloS One*, **2017**, *12*(5), e0178013.

(5) Cabraja, M.; Klein, M.; Lehmann, T.-N. Long-Term Results Following Titanium Cranioplasty of Large Skull Defects. *Neurosurgical Focus*, **2009**, *26*(6), E10.

(6) Winder, J.; Cooke, R.; Gray, J.; Fannin, T.; Fegan T. Medical Rapid Prototyping and 3D CT in the Manufacture of Custom Made Cranial Titanium Plates. *Journal of Medical Engineering & Technology*, **1999**, *23*(1), 26-28.

(7) Luo, J.; Morrison, D. A.; Hayes, A. J.; Bala, A.; Watts, G. Single-Piece Titanium Plate Cranioplasty Reconstruction of Complex Defects. *Journal of Craniofacial Surgery*, **2018**, *29*(4), 839.

(8) Kodera, Y.; Hardin, C. L.; Garay, J. E. Transmitting, Emitting and Controlling Light: Processing of Transparent Ceramics Using Current-Activated Pressure-Assisted Densification. *Scripta Materialia*, **2013**, *69*(2), 149-154.

(9) Klimke, J.; Trunec, M.; Krell, A. Transparent Tetragonal Yttria-Stabilized Zirconia Ceramics: Influence of Scattering Caused by Birefringence. *Journal of the American Ceramic Society*, **2011**, *94*(6), 1850-1858.

(10) Anselmi-Tamburini, U.; Woolman, J. N.; Munir, Z. A. Transparent Nanometric Cubic and Tetragonal Zirconia Obtained by High-Pressure Pulsed Electric Current Sintering. *Advanced Functional Materials*, **2007**, *17*(16), 3267-3273.

(11) Hannink, R. H. J.; Kelly, P. M.; Muddle, B. C. Transformation Toughening in Zirconia-Containing Ceramics. *Journal of the American Ceramic Society*, **2000**, *83*(3), 461-487.

(12) Messing, G. L.; Zhang, S.-C.; Jayanthi, G. V. Ceramic Powder Synthesis by Spray Pyrolysis. *Journal of the American Ceramic Society*, **1993**, *76*(11), 2707-2726.

(13) Studenikin, S. A.; Golego, N.; Cocivera, M. Fabrication of Green and Orange Photoluminescent, Undoped ZnO Films Using Spray Pyrolysis. *Journal of Applied Physics*, **1998**, *84*(4), 2287-2294.

(14) Mädler, L.; Kammler, H. K.; Mueller, R.; Pratsinis, S. E. Controlled Synthesis of Nanostructured Particles by Flame Spray Pyrolysis. *Journal of Aerosol Science*, **2002**, *33*(2), 369-389.

(15) Patil, P. S. Versatility of Chemical Spray Pyrolysis Technique. *Materials Chemistry and Physics*, **1999**, *59*(3), 185-198.

(16) Kontoyannis, C. G.; Orkoula, M. Quantitative Determination of the Cubic, Tetragonal and Monoclinic Phases in Partially Stabilized Zirconias by Raman Spectroscopy. *Journal of Materials Science*, **1994**, *29*(20), 5316-5320.

(17) Tabares, J. A. M.; Anglada, M. J. Quantitative Analysis of Monoclinic Phase in 3Y-TZP by Raman Spectroscopy. *Journal of the American Ceramic Society*, **2010**, *93*(6), 1790-1795.

Chapter 3: Review of CZTS and Photovoltaic Literature

3.1: A Background on Photovoltaics

The ability to harness the sun's energy incident on Earth's surface has long been touted as a large-scale electricity source of the future. The drawback thus far, though, has been cost-effectiveness relative to fossil-fuel consuming processes. As limitations and harmful effects on burning nonrenewable resources as fuel have become more and more well-documented in the past half-century, photovoltaic (PV) research has garnered significant interest in the international community, among other renewable technologies. The technology currently exists to harness solar energy and to do so efficiently, but it is not economically or politically tenable to implement large-scale solar power infrastructure. Hence, much work is currently focused on decreasing the cost of PV module fabrication, installation, and maintenance. On the cell fabrication side, a large focus is placed on optimizing alternative and inexpensive light-absorbing materials that can be produced via inexpensive and scalable processes.

French physicist Edward Becquerel is credited with the discovery of the PV effect in the mid-19th century, which is observed when a material absorbs a photon with enough energy to create a pair of excitons, or positively (holes) and negatively (electrons) oriented charge carriers. The crucial material-related component of this effect regards that threshold energy above which excitons will be generated, and below which absorbed light will be transferred to heat. In semi-conductors, this energy is referred to the band gap of the material, or the amount of energy required to boost a valence shell electron — spatially bound — into the conduction band, where it can propagate freely. It took nearly a century for Becquerel's PV effect to be applied as an effective PV cell due to the difficulty of collecting the excitons generated by photo-absorption.

Bell Labs made the major breakthrough in 1954, when Chapin, Fuller, and Pearson demonstrated the first practical solar cell, based on single-crystal silicon as the photo-absorber.[1] This cell demonstrated a photo-conversion efficiency of 6%. A similar iteration of this cell was fabricated and sold at $1,785 per Watt of power generated by Western Electric in 1955.

Chapin observed that a p-n semiconductor junction will create an electric field to push the exciton pair in opposite directions via Coulombic force.[1] By doping different elements into a semiconductor like silicon, in effect one is implanting either an excess of positive charge carriers in a semiconductor (making it a "p-type semiconductor") or an excess of negative charge carriers (making it an "n-type semiconductor"). Putting the p-type and n-type semiconductors in junction with each other, the excess and opposing charges in each side generate an intrinsic electric field. Chapin noted that this electric field could be used to guide positively and negatively charged excitons in opposite directions — positive charges would follow the direction of the electric field, and negative charges would follow the direction opposite to the electric field. Without the electric field, positively and negatively charged excitons will be attracted to each other and will undergo radiative exciton recombination. The simplified schematic of the p-n junction driven PV is seen in Fig. 1. Chapin's work on silicon-based p-n junction PVs has been steadily optimized since 1954, and today the latest iterations of this type of PV are nearing maximum theoretical efficiency.

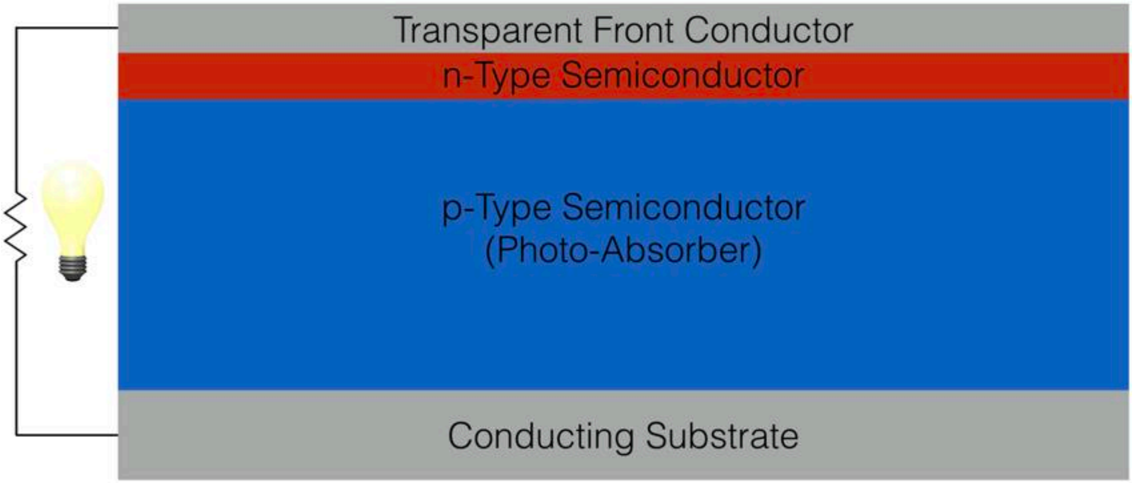

Figure 1: General schematic for a p-n junction PV similar to that made by Chapin in [1]. (Note: Chapin used a thick n-doped Si layer as the photo-absorber and a thin p-doped Si layer to complete the p-n junction; modern PVs use the layout above.)

Alternative material systems have also been studied and gradually optimized to account for the high material and processing costs associated with generating the single-crystal silicon layer in the cell schematic in Fig. 1. Yet the cost-per-Watt of power generated still makes solar energy impractical as part of a large-scale infrastructure.

Today, the effort to improve PV technology continues, with the notion of "grid parity" limiting the wide-spread use of PVs in the United States.[2] In essence, the consensus is that PVs will not be wide-spread until they are less expensive to fabricate, implement, and maintain such devices than to purchase mass-produced power generated from nonrenewable sources, like natural gas, coal, oil, or others.

Based on recent trends and public policy, the Department of Energy's annual energy outlook for the year 2018 [3] projects that domestic energy generated by renewable fuels will continue to expand to take the place of domestic nonrenewable-based fuels like petroleum and coal (Fig. 2a). Energy generation from renewable sources is projected to

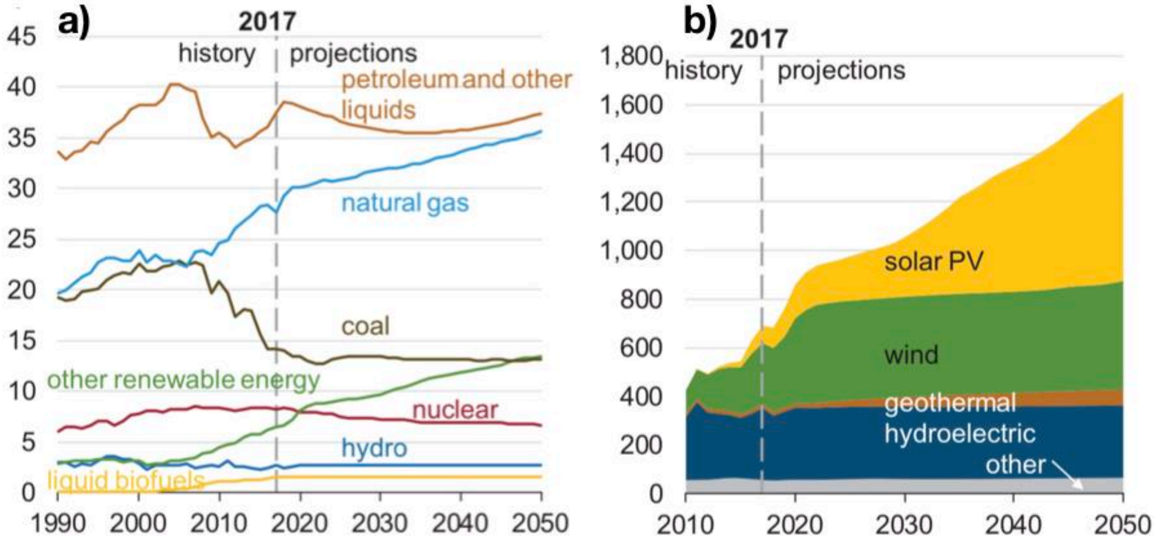

Figure 2: (From [3]) a) Shows past and projected percentages of energy consumption by fuel type from 1990-2050 in quadrillion BTU. b) Shows past and projected renewable electricity generation by fuel type from 2010-2050 in billion kilowatt hours.

grow at 1.5% annually, more than any other fuel source.[3] Further, domestic solar electricity generation is projected to grow more quickly than any other renewable source at 5% annually, and is expected to provide about 40% of all domestic electricity generated by renewable sources in 2050 (Fig. 2b).[3]

In the past few decades, there has been an ongoing search within the PV-research field for new materials and cell architectures that might circumvent the drawbacks to using silicon-based cells — namely that the most efficient single-crystal silicon-based PVs require relatively high production and high materials cost. Thin film PVs — cells based on thin film semiconductors as opposed to bulk, which is necessary with single-crystal silicon cells — have been well studied utilizing different photo-absorbing materials.

Copper-indium-gallium-selenide (CIGS) and cadmium telluride (CdTe) have both been extensively researched and have been improved to be efficient enough to sell publicly via startup companies like FirstSolar (CdTe) [4] or Solar Frontier (CIGS).[5] These materials, however, have significant drawbacks pertaining to mass market sustainability and environmental impact. Indium, in particular, is undesirable to use in a mass market product due to its scarcity and its subsequent high cost (Fig. 3), making this technology unsustainable for a large market.[6] Cadmium is a known human carcinogen, making its widespread commercial use undesirable due to possible negative health and environmental effects.

Relatively recently, in the past 20 years, copper-zinc-tin-sulfide — Cu_2ZnSnS_4 (CZTS) — has been investigated as a thin film photo-absorber for use in PV devices. This material is desirable due to the component elements' low-cost and Earth-abundance (Fig. 3). CZTS typically has a kesterite crystal structure which resembles the chalcopyrite structure of CIGS, though it can also be found as stannite (which only differs from

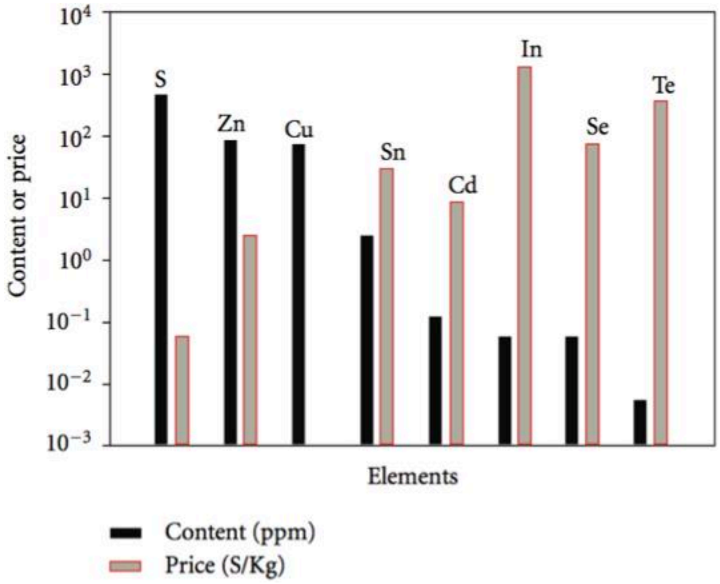

Figure 3: (From [6]) Shows content and price of elements commonly used in different thin film PV absorber layers.

kesterite in placement of copper and zinc atoms) or as wurtzite. Chen *et al*. calculate the kesterite structure to be the most thermodynamically stable of the three crystal structures.[7] Fig. 4 shows the orientations of the three CZTS crystal structures with the chalcopyrite CIGS crystal structure.

The band gap of CZTS is between 1-1.5 eV, and the material has an absorption coefficient on the order of 10^4 cm^{-1}, both desirable characteristics for use as a photo-absorber in a PV.[8] In simpler terms, it absorbs a significant amount of light corresponding to the solar spectrum, and the band gap energy corresponds to the photon energy

Figure 4: (From [8]) Shows chalcopyrite CIGS crystal structure (a) with different CZTS crystal structures (b, c, d).

provided by the solar spectrum meaning sun-light is capable of generating exciton pairs in this material. The primary advantage of using CZTS is that it offsets the drawbacks of silicon, CIGS, and CdTe technologies. Copper, zinc, tin, and sulfur are all relatively inexpensive, earth abundant, and environmentally friendly, and can be used in thin film polycrystalline photovoltaics.

CZTS is also a desirable material system because of its tunability. It is relatively straightforward both theoretically and experimentally to alloy or dope CZTS with different cations (like Fe, Ge, Ag, Ti, Cr, Mn, Sb etc.) or anions (like Se, Te). Through this process, the band gap and the band gap alignment can be tuned across a wide range of parameters. Using selenium in place of some sulfur is the most common technique, because it reduces the band gap to ~1.1 eV and provides better alignment with the corresponding n-type semiconductor junction facilitating charge transport.[7]

Presented here is our work investigating the viability of forming CZTS nanostructures and thin films by aerosol spray pyrolysis from different precursor sources. This work is intended to prove this to be an alternative method of synthesizing high-quality CZTS thin films for use in highly efficient PV cells, while also being easily implemented into commercial-scale production. There is herein much discussion of the application of CZTS as a photo-absorber layer in PVs, though our work is intended to investigate the control of CZTS material properties. In order to optimize the performance of CZTS-based PVs, we must first understand how to control phase and defect evolution in the material during processing, then the optimized PV structure can be constructed around the optimized absorber layer.

3.2: Notable Terms and Quantities

There are several terms and quantities that are used to describe the efficacy of PVs, the most notable of which are open circuit voltage (V_{OC}), short circuit current (J_{SC}), fill factor (FF), and photo-conversion efficiency (η). V_{OC} is defined as the potential difference generated by a PV across an effectively infinite load between the positive and negative charge collection terminals. J_{SC} is the electrical current flowing through the circuit when the load is effectively zero. There is an absolute extreme at which the PV will supply the most power, given by P_m or equivalently I_m*V_m. This allows the definition of FF as:

$$FF = \frac{I_m \times V_m}{I_{SC} \times V_{OC}} \qquad \text{(Eq. 1)}$$

and η as:

$$\eta = \frac{P_m}{P_L} \qquad \text{(Eq. 2)}$$

where P_L is the power of the light incident on the PV. P_L is generally simulated *in vitro*.[8]

For discussion in literature, it is globally accepted that PVs be characterized under the Standard Test Conditions: 25 ºC under Air Mass 1.5 spectrum illumination with an incident power density of 100 mW/cm^2.[8]

3.3: Current CZTS Benchmarks

In 1961, Shockley and Queisser presented a theoretical model detailing a limit to p-n junction PV cell performance that is still used for reference in literature today.[9] The model takes into account the total power supplied to a PV cell by the sun, taken to be an ideal black body at 6,000 ºC with the cell taken to be an ideal black body at 300 ºC. The limiting factors on photo-conversion efficiency are the band gap of the photo-absorber material and the exciton recombination frequency. For a perfectly optimized PV cell, the radiative recombination rate of excitons is governed by thermodynamic probability, and the number of generated excitons is governed by the absorber material's band gap. For a perfectly optimized CZTS-based PV cell with a band gap of 1.5 eV, the maximum theoretical efficiency is ~29%, while the maximum possible efficiency is ~31% for a material with a band gap of 1.1 eV.[9]

The current champion CZTS cell was published by Fukano *et al.*[10] The record efficiency is 8.5% ± 0.2% for a cell of 0.2382 cm^2. The V_{OC} is listed as 708 mV and the J_{SC} is listed as 16.83 mA/cm^2, while the FF is 70.9%.[10,11] To give perspective, the current champion CIGS cell has an efficiency of 21.7% ± 0.7%.[11] The V_{OC} is comparable, as the CIGS cell has V_{OC} of 796.3 mV, but the J_{SC} of the CIGS cell is vastly superior at 36.59 mA/cm^2 and the FF is improved to 79.3%.[11,12]

There has been extensive work done optimizing CZTS PVs by introducing selenium replacement defects in place of sulfur atoms in the kesterite lattice, with the new material called CZTSSe ($Cu_2ZnSn(S_xSe_{1-x})_4$). With this material system, a cell has been produced by Wang *et al.* with an efficiency of 12.6% ± 0.3%, with improved J_{SC} of 35.21 mA/cm^2 but diminished V_{OC} of 513.4 mV [13, 15].[13] Further, by alloying in silver to the kesterite CZTSSe lattice in place of copper (making AgCZTSSe), there are indications that the efficiency could be improved to >16%, though this has not been demonstrated experimentally.[14] While this is an encouraging improvement in photo-conversion efficiency, the material system will be disregarded in this work due to the inclusion of the rare and expensive element selenium (see Fig. 3).

In order for CZTS to be commercialized viably, it is generally accepted that the *in vitro* photo-conversion efficiency needs to be boosted to ~20%.

3.4: Ways to Improve CZTS-Based PV Efficiency

Due to the similarities between the CIGS and the CZTS material systems, it is logical to attempt to improve CZTS-based PVs in similar manners as have already proven effective in the improvement of CIGS-based PVs to beyond 20% efficient.

In 2013, a meeting of experts in the field was convened to identify critical steps toward improving CZTS as a thin film PV material.[15] The V_{OC} deficit (given by the difference between the band gap voltage — E_g/q — and the V_{OC}) in well-performing CIGS-based PVs is ~500 mV, while in the best CZTSSe devices the deficit is higher than 650 mV. From section 2.2, the benchmark CZTS device has a V_{OC} of 708 mV, which still yields a V_{OC} deficit of greater than 750 mV.[10]

Quoting from Polizzotti *et al.*:[15]

> *"Three key areas were identified to address this problem, as listed here in rough order of priority: (1) defect characterization and passivation, (2) phase stability and processing control, and (3) interface optimization."*

Further from Polizzotti *et al.*, defects in the CZTS layer cause the semiconducting properties of the material — primarily the band gap — to be nonuniform through the bulk material, leading to additional impedance affecting the generated excitons.[15] The high

V_{OC} loss is attributed to charge recombination centers, focused at bulk defect sites as well as grain boundaries and interfaces. The formation and control of these defects is not well understood at this point. With further understanding will come the ability to promote beneficial defects and to diminish detrimental ones in the synthesis of the CZTS absorber layer. The pn-junction also must be optimized in order to reduce interfacial exciton recombination.

Current work on improving the CZTS absorber layer focuses generally on improving the material stoichiometry [16-21] and crystallinity [22-26] within existing synthesis processes. Further efforts are focused on improving the pn-junction consisting of the CZTS and a thin n-type layer.[27-29] In short, it has been concluded that the ideal stoichiometry is slightly copper-poor and zinc-rich, that the presence of alkali metal defects in CZTS greatly aid crystal growth during annealing, and that ZnS is likely the ideal n-type material to pair with CZTS. Further work must be done to support these conclusions more solidly, though this is generally consensus in the field.

3.5: Material Synthesis Techniques

There are many different methods that have been used to generate CZTS or CZTSSe. The previously-mentioned CZTSSe benchmark was set in 2013 for a cell based on a CZTSSe layer grown using a hydrazine pure-solution approach.[13] The benchmark CZTS cell was made by sputtering ZnS/Sn/Cu/ZnS layers then annealing in a sulfur-rich atmosphere.[10] Further methods that have been used to synthesize CZTS layers for PVs are evaporation,[30-41] sputtering,[42-54] electrodeposition,[55-62] sol-gel based deposition,[63-71] pulsed laser deposition,[72-77] screen printing,[78,79] chemical bath deposition,[80-84] nanoparticle based sintering,[85-98] and aerosol spray pyrolysis.[99-107]

Of these synthesis methods, evaporation, sputtering, and electrodeposition have generally yielded the highest efficiency devices. Other methods are primarily intended as more cost-effective or scalable alternatives. Aerosol spray pyrolysis will be discussed further in section 3.6. Nanoparticle synthesis and sintering will be discussed further in sections 3.7 and 3.8.

Evaporation:

Evaporation is a commonly used process to synthesize metallic or semiconducting thin films. The target material, in liquid or more typically solid phase, is evaporated by a concentrated electron beam, directed by Coulombic force, and directed onto a substrate (Fig. 5).[108] Typically, evaporation of the target will be incited by an electron beam, but it can also be achieved thermally. This process can be done with an individual target, or multiple targets can be used simultaneously. For example, a cuprous sulfide thin film can

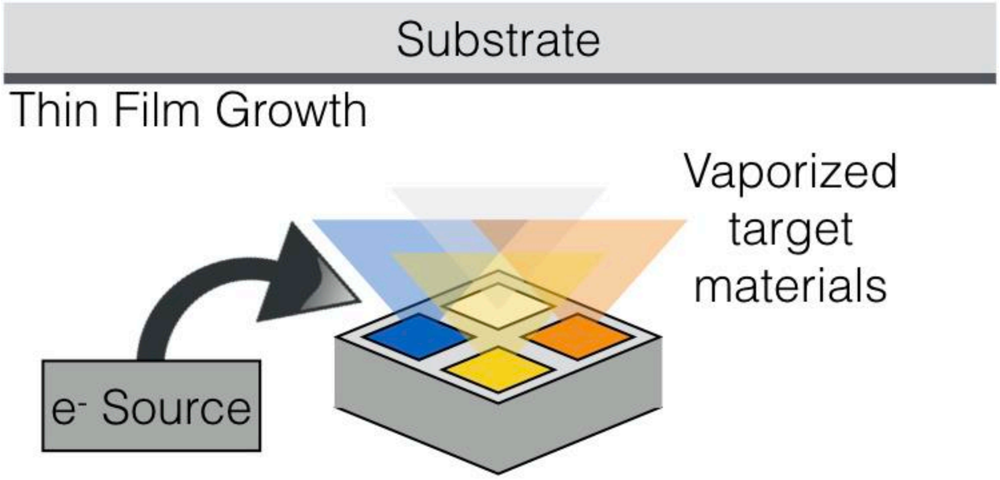

Figure 5: General schematic for a multi-target electron beam evaporator.

be formed by co-evaporating copper and sulfur targets.

There are two common methods by which evaporation is used to synthesize CZTS. Katagiri *et al.* pioneered the method by evaporating separate copper, zinc, and tin layers onto a heated molybdenum-coated soda lime glass substrate, then thermally annealing in an $N_2 + H_2S$ environment.[30,31] The material was characterized to be stannite CZTS. The stoichiometry of the material was governed by the relative thickness of the three metallic layers.

Other groups have added sulfur in the evaporation process, either via the replacement of the zinc target with a zinc sulfide target,[32-35,40] or the addition of a sulfur target to the three elemental targets.[36] Some of the most efficient CZTS-based PVs to have been reported have all been fabricated with a co-evaporated CZTS layer with an added thermal annealing process.

Sputtering:

Sputtering is another commonly known process. It is similar to e- beam evaporation, but the target material is eroded away by a gaseous ion plasma, typically made from an inert carrier gas like argon, instead of an electron beam. Neutral particles of the target material ejected from the target then nucleate and form a thin film on the substrate surface (Fig. 6).[109] Similar to evaporation, this process can use multiple targets to form alloy thin films.

Sputtered synthesis of polycrystalline stannite CZTS was first reported by Ito and Nakazawa in 1988.[42] They reported an improved quality film with decreasing resistivity as substrate temperature during film growth was increased. The conclusion drawn was

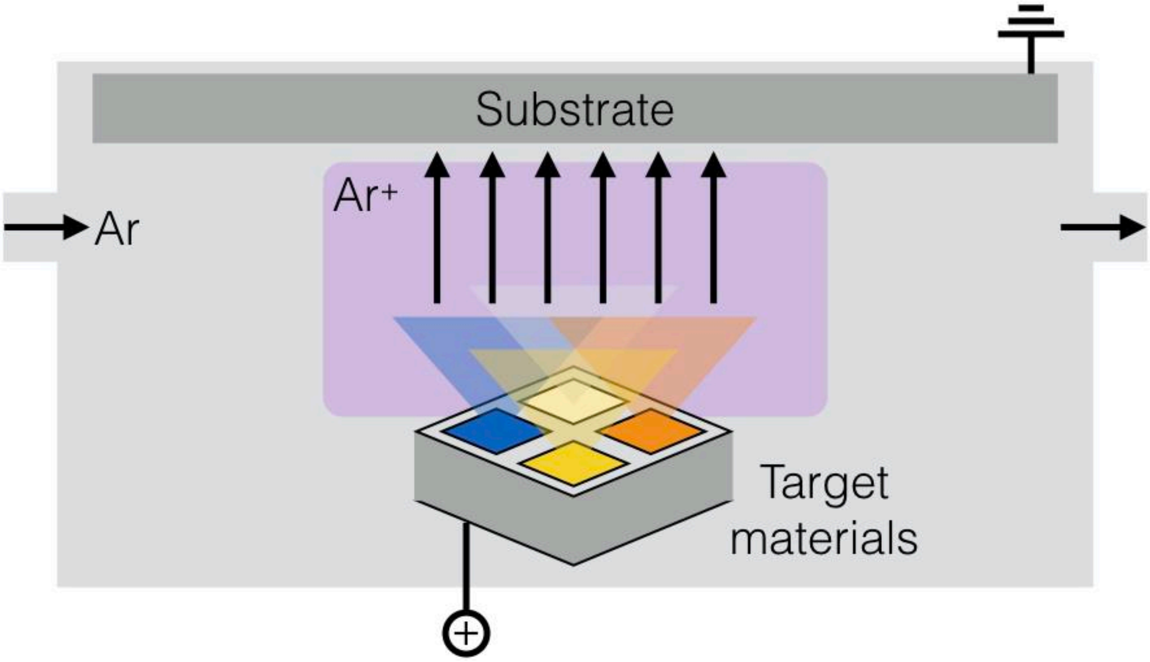

Figure 6: General schematic for a multi-target sputterer.

that CZTS is a suitable absorber layer for a PV due to its high absorption coefficient and its direct band gap. Again similar to evaporation, there has been work reported as having synthesized CZTS via thermal annealing of a sputtered stack of copper, zinc, and tin metals,[44,45,49,53] as well as work reporting the sputtering of binary sulfide targets — most commonly in the form of tin sulfide and zinc sulfide with elemental copper.[46-48,51,52,54]

Sputtering deposition creates films of a similar quality to evaporation, so it is not surprising that sputtering-deposited CZTS-based PVs have similarly impressive efficiencies to those synthesized via evaporation, including the current benchmark in [10].

Electrodeposition:

Electrodeposition uses precursor materials dissolved in an electrolyte to complete a circuit across two electrodes, with the current flowing between the electrodes through the electrolyte causing the dissociation of the precursors and deposition onto the working electrode (Fig. 7).[110] Electrodeposition is more dependent on precursor materials than processing conditions, as opposed to the previously discussed vapor deposition processes. The process is presented as more inexpensive and scalable than vacuum-based vapor deposition processes.

To make CZTS, there are a variety of precursors that can be used. Scragg *et al.* demonstrated the synthesis of a copper-tin-zinc metal stack via electrodeposition, followed by a sulfur-vapor annealing step to make CZTS. The work used three separate deposition steps, the each using a singular copper, tin, or zinc chloride as the precursor dissolved in the electrolyte.[56] There has been further work via the same precursor chemistry in.[55,58,60] There has also been some study of single-step electrodeposition of

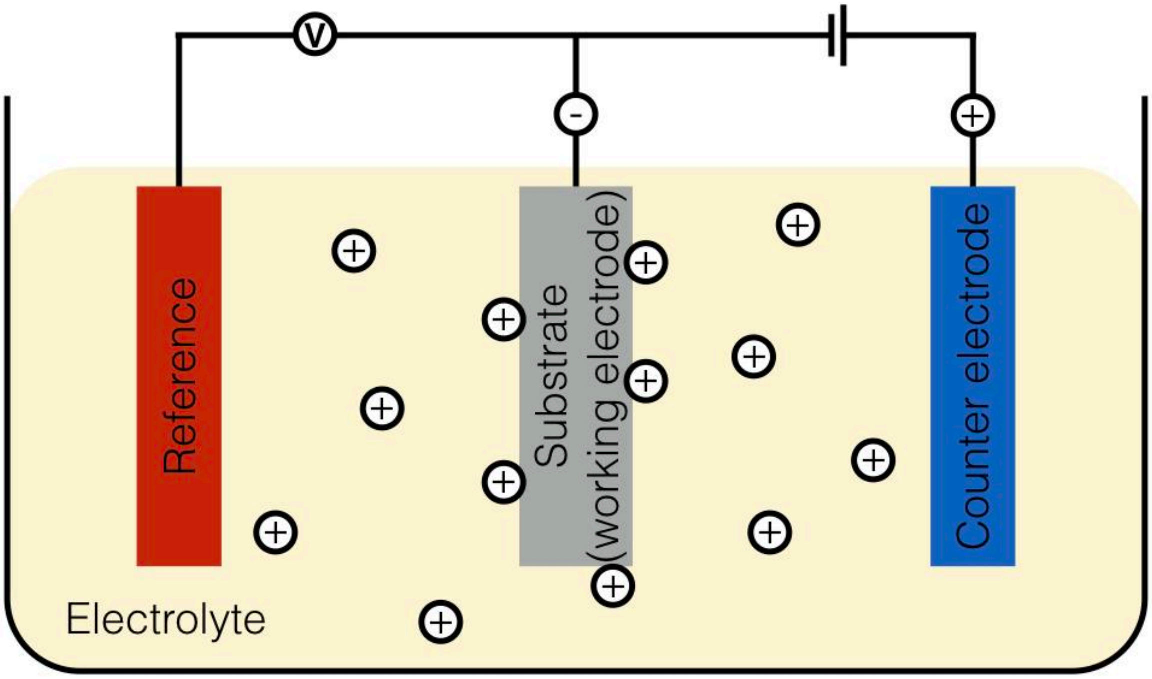

Figure 7: General schematic for an electrodeposition setup.

CZTS by combining copper, zinc, and tin sulfates with sodium thiosulfate in the electrolytic solution in,[62] as well as further single-step depositions in.[56,57,59,61]

Ahmed *et al.* reported a 7.3% efficient CZTS-based PV,[55] the highest value yet reported for this sort of process, based on a thermally annealed electrodeposited three-metal stack of copper, zinc, and tin.

Sol-Gel Deposition:

The sol-gel deposition is fairly straightforward in concept. Precursor metal salts are dissolved in a mixture of solvent and binder, then coated onto a substrate. Thermal treatment of the coating allows for evaporation of the solvent and decomposition of the precursors. A further annealing step allows for the full conversion to a CZTS thin film.[65] This process is advantageous due to its cost-effectiveness and ability to be run at atmospheric pressure.

The biggest source of variety for CZTS synthesis from the sol-gel deposition method is the use of different precursors and solvents. The highest efficiency cell based on a CZTS layer fabricated in this fashion is outlined in [65].[65] Su *et al.* used a non-aqueous thiourea-metal-oxygen molecule as the precursor solute, which underwent thermal decomposition at a relatively low temperature to leave a more favorable material behind. Their best cell achieved an efficiency of 5.1%. More commonly used as precursor solutes are copper, zinc, and tin acetates or chlorides with or without a sulfur source added as precursor via thiourea [63,64,66-68,71] ([68] used tin sulfide as the tin source).

Pulsed Laser Deposition:

Pulsed laser deposition (PLD) is a vacuum process similar to evaporation and sputtering. Energy is supplied to a target, typically in the form of a pellet, via a high-energy laser pulse. Material is ablated from the target in the form of ionic plasma, which then settles on a substrate within the chamber (Fig. 8).[111] Targets can be elementary or alloy, allowing for deposition of either simple or complex thin films. These films still require a further annealing step after deposition.

The best device fabricated using this method has an efficiency of 3.14%.[73] The PLD deposition was achieved by ablating a target formed by mixing copper, tin, and zinc binary sulfides in adequate ratios into a solid CZTS pellet. Further work studying the PLD deposition of CZTS from a CZTS pellet has been shown in.[75,76] Moriya pioneered this method of CZTS deposition by depositing a mixture of copper, zinc, and tin, then annealing in a sulfur atmosphere.[72,74] Further work has been done using zinc sulfide and

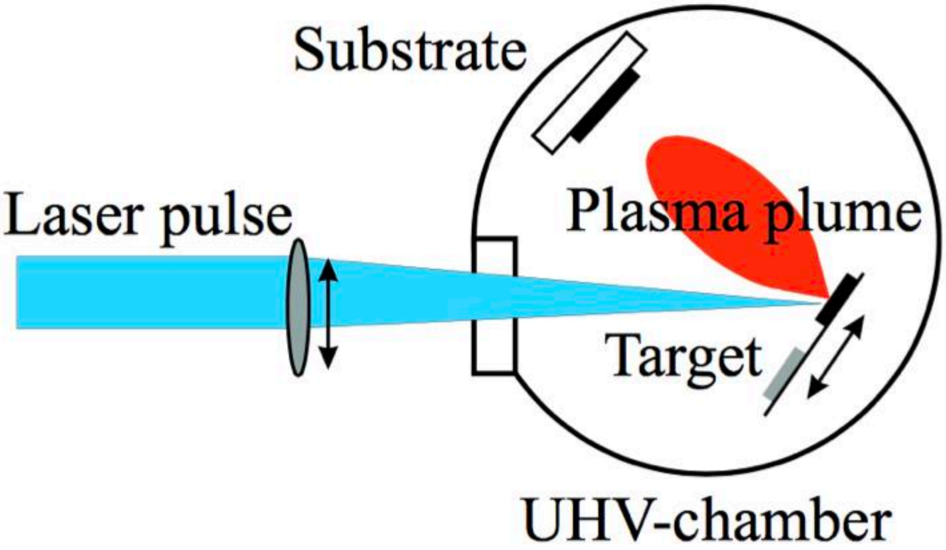

Figure 8: (From [102]) General schematic for a PLD setup.

copper-tin-sulfide multicomponent targets.[77]

Screen Printing:

Screen printing deposition is very similar to sol-gel deposition. It is a solution-phase process by which CZTS particles are dispersed into a solvent at high concentration to make a thick paste. The solution is then coated by dragging the paste across a screen placed atop the substrate. The coating is then thermally treated to evaporate solvent and remove organic ligands.[78]

Screen printing is well known in the PV field. It has been used in fabricating crystalline silicon PVs, which proved to be a fiscally advantageous innovation.[8] The best cell efficiency discussed in [78] was 0.49%, but the advantages — being cost- effective, scalable, well-known to industry, and relatively simplistic — of using such a process as screen printing have proven effective in PV fabrication in the past, and could prove to be so for the CZTS material system as well in the future.

Chemical Bath Deposition:

Chemical bath deposition (CBD) is a similar process to electrodeposition. It is another non-vacuum, conceptually simple method of thin film deposition. The process depends simply on the either chemical and/or thermal dissolution and deposition of precursors based on the solution bath chemistry and the surface of the substrate (Fig. 9).[112] CBD has been used to synthesize CZTS thin films in various ways. Wangperawong *et al.* deposited copper, zinc, tin, and sulfur layers and annealed the samples to form CZTS.[80] Similar results have also been achieved by depositing layers of copper, zinc, and/or tin binary sulfides.[82-84] This method has not been shown to be viable relative to

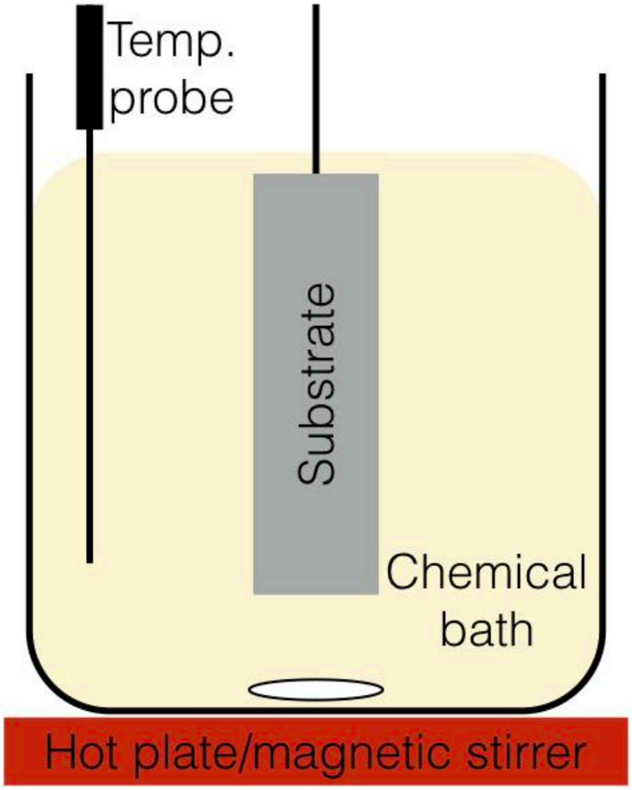

Figure 9: General schematic for a CBD setup.

other low-cost non-vacuum based methods, with the highest efficiency reported for a CBD-deposited CZTS-based PV as 0.16%.[80]

3.6: Spray Pyrolysis of CZTS Thin Films

Aerosol spray pyrolysis is a non-vacuum solution/gas phase process. In theory, it is similar to the previously discussed solution- based processes in section 3.5. Spray pyrolysis relies on the thermal decomposition of precursors in order to form a desired material. It differs, though, in the notion that the precursor solution is aerosolized via a nebulizer into micro-scale droplets before deposition to decrease the deposition speed, which theoretically allows more complete thermal equilibration to form the desired material (Fig. 10).[113]

There have been several reports of using spray pyrolysis to synthesize CZTS thin films. Generally, a precursor solution containing copper, zinc, and tin chlorides or acetates plus thiourea is used, with an operating substrate temperature between 400-450 ºC.[99-107] The common conclusion is that the resulting film is not phase-pure, with primarily copper sulfide impurities, and further the crystallinity of the sprayed films post-annealing is poor for PV applications. A further disadvantage of this work is the use of metal chlorides or acetates as precursors. The chlorine or oxygen present in the precursors leads to a high concentration of undesirable impurities in the sprayed film.

Aerosol spray pyrolysis is regarded as a readily scalable method for CZTS synthesis, as it is a process well known to be successful in synthesizing nanoparticles. For example, the method is used to form titania nanoparticles,[114] which are commonly used in pigments and cosmetics, as well as other more technological applications. In our work, we have studied the growth of CZTS thin films by spray pyrolysis, though we use copper, zinc, and tin diethyldithiocarbamate ($C_5H_{10}NS_2$) precursors.[115] The advantage of using

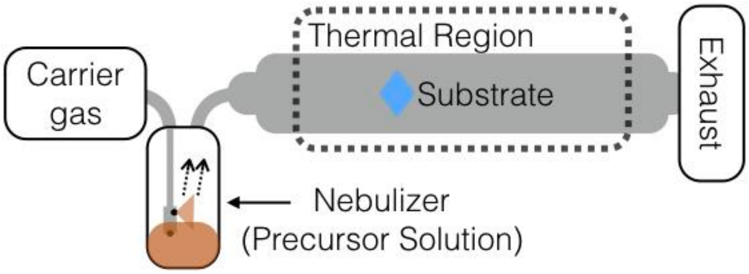

Figure 10: General schematic for a thin film aerosol spray pyrolysis setup.

these precursors is the lack of chlorine or oxygen in the ligand, which lead to impurities in the film.

3.7: CZTS Nanoparticle Synthesis

A method of creating CZTS that has been steadily growing in interest in recent years is nanoparticle sintering. It is thought to be among the most cost-effective and scalable methods outlined in this chapter and marked recent improvements in reported efficiencies for nanoparticle CZTS-based PVs suggest there is still room for improvement in material processing. CZTS nanoparticle-based PVs have been reported to have 3.6% efficiency under conventional construction,[93] and up to 5.02% efficiency with a novel three-dimensional architecture,[91] which puts it close to the range of PVs fabricated with vacuum-processed CZTS.

There are different methods of CZTS nanoparticle synthesis that have been employed, which yield nanoparticles with different material properties. The most common method is solution-phase thermolysis.[85-88,90-98] In this method, precursor solutes are dissolved with the help of an acidic solvent. Typically precursor solutes are basic copper, tin, and zinc chlorides or acetates plus thiourea as the sulfur source, as are used in other solution-phase processes outlined above.[85,86,90-95,97,98] Other work has used the single-source metal and sulfur precursors copper, tin, and zinc diethyldithiocarbamates ($C_5H_{10}SN_2$).[87,88,96] The advantage to the single-source metal and sulfur precursors lies in the reduction of undesirable impurity atoms in the reactor, which are present with the use of chlorides or acetates. The solution is then combined with a hot amine solvent and thermally treated under an inert atmosphere to decompose the solutes and form CZTS nanoparticles. The resultant particles are invariably capped by organic ligands leftover from the amine solvent.

The nanoparticles synthesized in the method above are highly controllable in composition and size, both ideal for adjusting the synthesis for optimal PV performance. Once the nanoparticles are isolated, they can be dispersed into a colloidal ink, then coated on a substrate. The porous nanocrystal film must then be sintered to form large crystal grains, on the order of the thickness of the film, for the best PV characteristics.[8]

The work described here in Chapters 4-5, outlines a novel method of controllably forming ligand-free CZTS nanoparticles via aerosol spray pyrolysis. The method is very similar to that outlined in Section 3.6 (and Fig. 10), but the substrate is removed from the thermal region and a particle collection apparatus is added beyond the thermal region to collect the synthesized nanoparticles.

3.8: CZTS Sintering/Annealing

Most of the methods of forming CZTS absorber layers for PVs listed in Sections 3.5-7 require an extra annealing/sintering step in a sulfur environment. Generally, the reason is to allow thermal equilibrium of phases and crystallinity for the film to possess the optimal PV characteristics. As discussed in Section 3.4, the two most important steps to improving CZTS as a PV absorber material is passivating and decreasing undesirable defects and improving phase stability.[15]

When a metal stack or metal-alloy is deposited on a substrate, the sulfur annealing process is required to diffuse sulfur into the metal layer(s) and form crystalline CZTS. The annealing time is understandably lengthy in this case, on the scale of 8-10 hours,[8] in order to allow the sulfur to fully diffuse through the film and to reach chemical steady state. With sulfur already included in the pre-annealed film, the annealing step requires much less time, now on the order of 1 hour or less.[8] In this case, the annealing step is geared towards increasing crystal grain size, phase purity, and cation ordering. With a nanoparticle CZTS film, the annealing step is also short and aimed at increasing crystal grain size, as the nanoparticles are already assumed to be phase pure.

The conditions of the annealing process must be optimized with the CZTS film. It has been observed that under different annealing conditions, primarily with annealing temperature and sulfur pressure varied, different material phases tend to out-diffuse from the CZTS film, primarily the binary copper sulfide and tin sulfide phases.[116] The same has been observed in annealing tin-rich and copper-rich samples in our work. Typically, the stoichiometry of the film must be compensated slightly to account for the loss of some tin and copper during annealing.[8]

There are two methods of sulfur-annealing used in literature. The first requires an evacuated quartz ampoule or graphite vessel with solid sulfur placed inside with the sample ([87], for example). Upon thermal treatment, the sulfur is vaporized to provide an easily variable sulfur pressure during the anneal. The other method uses a thermal flow reactor, with the sample placed inside a thermal region feeling a flow of 1-5% H_2S + 95-

99% inert gas (in [30], for example). Both methods have been demonstrated as effective in annealing and sintering CZTS films for use in PV cells.

3.9: CZTS Thin Film and Nanoparticle Characterization

As complex as fabricating the quaternary CZTS is, characterizing the presence of phase-pure CZTS is equally challenging. X-ray diffraction (XRD), is the most common and straightforward method of characterizing crystalline phases in bulk or nanostructured material, but XRD alone is not enough to adequately characterize CZTS. The diffraction peaks associated with kesterite CZTS are also common to other binary or ternary sulfide phases that can segregate from CZTS. In particular, zinc sulfide and copper-tin-sulfide give identical or effectively identical diffraction spectra, making it impossible to tell which phases might be present. Raman spectroscopy (Raman) in combination with XRD provides sufficient data to characterize each of these binary or ternary sulfide phases as separate from the quaternary kesterite CZTS phase.[117]

Further material characterization can be performed via X-ray photoelectron spectroscopy (XPS) and energy dispersive x ray spectroscopy (EDS). These techniques make it possible to identify relative atomic proportions within a sample, as well as the presence and abundance of impurity elements relative to the CZTS material.[38]

Optical characterization techniques also allow the identification of the semiconducting properties of a CZTS thin film or nanoparticles. Conducting UV/Vis/NIR spectrophotometry allows the measurement of the material's absorbance across a broad spectrum. Typically, PV absorbers such as CZTS are optimized to have broad absorbance across the UV and visible spectrum, correlating to the spectrum of light given off by our sun. From this data, a Tauc plot can be created, by plotting the square of the product of the material's absorbance and the photon energy ($h\nu$).[8] Extrapolation of the Tauc plot allows for a reasonable estimation of the materials optical band gap.

3.10: Phase Evolution and Segregation in CZTS During Processing

At the 600 ºC annealing temperature used in this and prior works from our group, kesterite CZTS should be unstable if even slightly-off stoichiometric according to quasi-ternary-phase diagrams.[118,119] Additionally, the presence of any secondary phases — noted as prevalent by Alvarez *et al.* [120] — will influence the composition of the regions of kesterite-CZTS.[121.122] Valle Rios *et al.*, however, note experimentally that kesterite CZTS is stable at room temperature at off-stoichiometric values due to the formation of intrinsic point defects.[123] Specifically for the Cu-poor, Zn-rich condition mentioned above as optimal for PV performance, the key defects are V_{Cu} and Zn_{Cu} antisites, which are beneficial to charge transport in the bulk material system.[124] Comprehensive studies by Lund *et al.* [125] and Du *et al.* [118] further indicate the importance of tin content as well. An excess of tin will result in a high degree of disorder in the kesterite lattice [122,126] while also contributing to a quenching effect of the PL signal.[118] Just *et al.* report empirically for a copper-poor, zinc-rich, tin-poor CZTS-based PV a minority carrier diffusion length of 270 nm and a total collection length of ~500 nm, both of which indicate that charge collection should not hinder performance of CZTS-based PVs.[127]

Többens *et al*. report on the ordering of copper and zinc cations in CZTSe at different temperatures using an anomalous XRD technique.[128] By analyzing a shift in lattice parameters, they were able to derive a shift in copper and zinc lattice sites and correlated the shift to a transition to a disordered CZTSe phase above 203 ± 6 ºC. Rudisch *et al*. confirm this order-disorder transition in CZTS using Raman spectroscopy in correlation with simulations based on Vineyard's theory of order.[129] Both of these studies rely on *ex situ* characterization after quenching or varying cooling rate on annealing CZTS/CZTSe material.

At higher temperatures still, off-stoichiometric CZTS will undergo phase segregation beyond cation disorder. In correlation with the knowledge that films should undergo phase transitions from disordered and segregated phases to primarily bulk-CZTS when cooling from high temperature. Sayed *et al*. report the recrystallization temperature to be 383 ± 6 ºC according to *in situ* XRD monitoring.[130] Wang *et al*. report a similar (though imprecise) recrystallization temperature on cooling using an *in situ* Raman experiment.[131] Further, Wang *et al*. are able to monitor phase segregation and evolution during high temperature annealing, noting that high annealing temperatures (>500 ºC) are required to fully crystallize kesterite CZTS and inhibit the formation of copper sulfide. Their annealing procedure is not optimal as understood in much of the literature in the field, though. To anneal, the films are placed inside a heating stage with constant inert gas flow and a constant heating/cooling rate of 30 ºC/min. is applied. With no external sulfur pressure, the film composition will be unstable and volatile phases will not be retained. Further, the fast cooling rate has been shown extensively in literature to promote segregated phase retention.[119] Additionally, the group used a solution-based thin film synthesis method (SILAR), and gave no consideration to grain growth mechanics.

Both phase evolution and grain growth mechanics can be understood in the CZTS system by *in situ* monitoring of the annealing process. Due to it being such a complex material system with inherent antisite and vacancy defects, computational approaches have been largely inconclusive, making *in situ* experiments more valuable to understanding the physics underpinning the material behavior. Raman spectroscopy allows for more intensive monitoring of phase evolution in the material system, as it allows identification of phases indiscernible in diffraction spectra.[117]

3.11: References

(1) Chapin, D. M.; Fuller, C. S. A New Silicon P-N Junction Photocell for Converting Solar Radiation into Electrical Power. *Journal of Applied Physics*, **1954**, *25*(5), 676-677.

(2) Breyer, C.; Gerlach, A. Global Overview on Grid-Parity. *Progress in Photovoltaics: Research and Applications*, **2013**, *21*(1), 121-136.

(3) Annual Energy Outlook 2018 with Projections to 2050. *U.S. Energy Information Administration*, **2018**.

(4) “First Solar Sets World Record for CdTe Solar PV Efficiency.” First Solar, Inc. News provided by *Acquire Media*, **2011**. <http://investor.firstsolar.com/releasedetail.cfm?ReleaseID=593994>.

(5) “Company Overview of Solar Frontier K.K.” *Business Week*, **2015**. <http://www.bloomberg.com/research/stocks/private/snapshot.asp?privcapId=52311569>.

(6) Wang, H. Progress in Thin Film Solar Cells Based on CZTS. *International Journal of Photoenergy*, **2011**, *2011*, e801292.

(7) Chen, S.; Gong, X. G.; Walsh, A.; Wei, S.-H. Crystal and Electronic Band Structure of Cu2ZnSnX4 (X=S and Se) Photovoltaic Absorbers: First-Principles Insights. *Applied Physics Letters*, **2009**, *94*(4), 041903.

(8) Jiang, M.; Xingzhong, Y. Cu2ZnSnS4 Thin Film Solar Cells: Present Status and Future Prospects. In *Solar Cells - Research and Application Perspectives* (ed. A. Morales-Acevedo). **2013**.

(9) Shockley, W.; Queisser, H. J. Detailed Balance Limit of Efficiency of P-N Junction Solar Cells. *Journal of Applied Physics*, **1961**, *32*(3), 510-519.

(10) Fukano, T.; Tajima, S.; Ito, T. Enhancement of Conversion Efficiency of Cu2ZnSnS4 Thin Film Solar Cells by Improvement of Sulfurization Conditions. *Applied Physics Express*, **2013**, *6*(6), 062301.

(11) Green, M. A.; Emery, K.; Hishikawa, Y.; Warta, W.; Dunlop, E. D. Solar Cell Efficiency Tables (Version 45). *Progress in Photovoltaics: Research and Applications*, **2015**, *23*(1), 1-9.

(12) Wischmann, W.; Menner, R.; Lotter, E.; Würz, R.; Witte, W.; Paetel, S.; Hariskos, D.; Jackson, P.; Powalla, M.

(13) Wang, W.; Winkler, M. T.; Gunawan, O.; Gokmen, T.; Todorov, T. K.; Zhu, Y.; Mitzi, D. B. Device Characteristics of CZTSSe Thin-Film Solar Cells with 12.6% Efficiency. *Advanced Energy Materials*, **2014**, *4*(7), 1301465.

(14) Hages, C. J.; Koeper, M. J.; Agrawal, R. Optoelectronic and Material Properties of Nanocrystal-Based CZTSe Absorbers with Ag-Alloying. *Solar Energy Materials and Solar Cells*, **2016**, *145*(3), 342-348.

(15) Polizzotti, A.; Repins, I. L.; Noufi, R.; Wei, S.-H.; Mitzi, D. B. The State and Future Prospects of Kesterite Photovoltaics. *Energy & Environmental Science*, **2013**, *6*(11), 3171-3182.

(16) Mousel, M.; Schwarz, T.; Djemour, R.; Weiss, T. P.; Sendler, J.; Malaquias, J. C.; Redinger, A.; Cojocaru-Mirédin, O.; Choi, P.-P.; Siebentritt, S. Cu-Rich Precursors Improve Kesterite Solar Cells. *Advanced Energy Materials*, **2014**, *4*(2), 1300543.

(17) Gershon, T.; Gokmen, T.; Gunawan, O.; Haight, R.; Guha, S.; Shin, B. Understanding the Relationship between Cu2ZnSn(S,Se)4 Material Properties and Device Performance. *MRS Communications*, **2014**, *4*(4), 159-170.

(18) Sarker, P.; Al-Jassim, M. M.; Huda, M. N. Theoretical Limits on the Stability of Single-Phase Kesterite-Cu2ZnSnS4. *Journal of Applied Physics*, **2015**, *117*(3), 035702.

(19) Redinger, A.; Berg, D. M.; Dale, P. J.; Siebentritt, S. The Consequences of Kesterite Equilibria for Efficient Solar Cells. *Journal of the American Chemical Society*, **2011**, *133*(10), 3320-3323.

(20) Han, D.; Sun, Y. Y.; Bang, J.; Zhang, Y. Y.; Sun, H.-B.; Li, X.-B.; Zhang, S. B. Deep Electron Traps and Origin of ‘P’-Type Conductivity in the Earth-Abundant Solar-Cell Material Cu2ZnSnS4. *Physical Review B*, **2013**, *87*(15), 155206.

(21) Tanaka, T.; Yoshida, A.; Saiki, D.; Saito, K.; Guo, Q.; Nishio, M.; Yamaguchi, T. Influence of Composition Ratio on Properties of Cu2ZnSnS4 Thin Films Fabricated by Co-Evaporation. *Thin Solid Films, The 10th International Symposium on Sputtering and Plasma Processes (ISSP2009)*, **2010**, *518*(21), S29-33.

(22) Johnson, M.; Baryshev, S. V.; Thimsen, E.; Manno, M.; Zhang, X.; Veryovkin, I. V.; Leighton, C.; Aydil, E. S. Alkali-Metal-Enhanced Grain Growth in Cu2ZnSnS4 Thin Films. *Energy & Environmental Science*, **2014**, *7*(6), 1931-1938.

(23) Dasgupta, U.; Saha, S. K.; Pal, A. J. Plasmonic Effect in Pn-Junction Solar Cells Based on Layers of Semiconductor Nanocrystals: Where to Introduce Metal Nanoparticles? *Solar Energy Materials and Solar Cells*, **2015**, *136*, 106-112.

(24) Kim, H. T.; Kim, C.-D.; Kim, C.; Kim, M. J.; Park, C. Effect of Sodium Chloride (NaCl) as Crystallization Catalyst on Cu2ZnSnS4 (CZTS) Films Deposited by Wet-Solution Coating Method. *Molecular Crystals and Liquid Crystals*, **2014**, *602*(1), 144-150.

(25) Guijarro, N.; Prévot, M. S.; Sivula, K. Enhancing the Charge Separation in Nanocrystalline Cu2ZnSnS4 Photocathodes for Photoelectrochemical Application: The Role of Surface Modifications. *The Journal of Physical Chemistry Letters*, **2014**, *5*(21), 3902-3908.

(26) Baryshev, S. V.; Thimsen E. Enthalpy of Formation for Cu-Zn-Sn-S (CZTS) Calculated from Surface Binding Energies Experimentally Measured by Ion Sputtering. *Chemistry of Materials*, **2015**, *27*(7), 2294-2298.

(27) Shin, B.; Zhu, Y.; Bojarczuk, N. A.; Chey, S. J.; Guha, S. Control of an Interfacial MoSe2 Layer in Cu2ZnSnSe4 Thin Film Solar Cells: 8.9% Power Conversion Efficiency with a TiN Diffusion Barrier. *Applied Physics Letters*, **2012**, *101*(5), 053903.

(28) Haque, F.; Khan, N. A.; Rahman, K. A.; Islam, M. A.; Alam, M. M.; Sopian, K.; Amin, N. Prospects of Zinc Sulphide as an Alternative Buffer Layer for CZTS Solar Cells from Numerical Analysis. In *2014 International Conference on Electrical and Computer Engineering (ICECE)*, **2014**, 504-507.

(29) Yu, K. M.; Mayer, M. A.; Speaks, D. T.; He, H.; Zhao, R.; Hsu, L.; Mao, S. S.; Haller, E. E.; Walukiewicz, W. Ideal Transparent Conductors for Full Spectrum Photovoltaics. *Journal of Applied Physics*, **2012**, *111*(12), 123505.

(30) Katagiri, H.; Sasaguchi, N.; Hando, S.; Ohashi, J.; Hoshino, S.; Yokota, T. Preparation and Evaluation of Cu2ZnSnS4 Thin Films by Sulfurization of E-B Evaporated Precursors. *Solar Energy Materials and Solar Cells*, **1997**, *49*(1), 407-414.

(31) Araki, H.; Mikaduki, A.; Kubo, Y.; Sato, T.; Jimbo, K.; Maw, W. S.; Katagiri, H.; Yamazaki, M.; Oishi, K.; Takeuchi, A. Preparation of Cu2ZnSnS4 Thin Films by Sulfurization of Stacked Metallic Layers. *Thin Solid Films, Proceedings of the 2nd International Symposium on the Manipulation of Advanced Smart Materials*, **2008**, *517*(4), 1457-1460.

(32) Katagiri, H.; Ishigaki, N.; Ishida, T.; Saito, K. Characterization of Cu2ZnSnS4 Thin Films Prepared by Vapor Phase Sulfurization. *Japanese Journal of Applied Physics*, **2001**, *40*(2R), 500.

(33) Kobayashi, T.; Jimbo, K.; Tsuchida, K.; Shinoda, S.; Oyanagi, T.; Katagiri, H. Investigation of Cu2ZnSnS4-Based Thin Film Solar Cells Using Abundant Materials. *Japanese Journal of Applied Physics*, **2005**, *44*(1S), 783.

(34) Schubert, B.-A.; Marsen, B.; Cinque, S.; Unold, T.; Klenk, R.; Schorr, S.; Schock, H.-W. Cu2ZnSnS4 Thin Film Solar Cells by Fast Coevaporation. *Progress in Photovoltaics: Research and Applications*, **2011**, *19*(1), 93-96.

(35) Weber, A.; Krauth, H.; Perlt, S.; Schubert, B.; Kötschau, I.; Schorr, S.; Schock, H. W. Multi-Stage Evaporation of Cu2ZnSnS4 Thin Films. *Thin Solid Films, Thin Film Chalcogenide Photovoltaic Materials (EMRS, Symposium L)*, **2009**, *517*(7), 2524-26.

(36) Wang, K.; Gunawan, O.; Todorov, T.; Shin, B.; Chey, S. J.; Bojarczuk, N. A.; Mitzi, D.; Guha, S. Thermally Evaporated Cu2ZnSnS4 Solar Cells. *Applied Physics Letters*, **2010**, *97*, 143508.

(37) Shin, B.; Zhu, Y.; Gershon, T.; Bojarczuk, N. A.; Guha, S. Epitaxial Growth of Kesterite Cu2ZnSnS4 on a Si(001) Substrate by Thermal Co-Evaporation. *Thin Solid Films*, **2014**, *556*, 9-12.

(38) Hurtado, M.; Cruz, S. D.; Becerra, R. A.; Calderon, C.; Bartolo-Perez, P.; Gordillo, G. XPS Analysis and Structural Characterization of CZTS Thin Films Prepared Using Solution and Vacuum Based Deposition Techniques. In *Photovoltaic Specialist Conference (PVSC), 2014 IEEE 40th*, **2014**, 0368-0372.

(39) Li, Y.; Chen, J.; Ma, J. Properties of Cu2ZnSnS4 (CZTS) Thin Films Prepared by Plasma Assisted Co-Evaporation. *Journal of Materials Science: Materials in Electronics*, **2015**, 1-6.

(40) Zhang, J.; Long, B.; Cheng, S.; Zhang, W. Effects of Sulfurization Temperature on Properties of CZTS Films by Vacuum Evaporation and Sulfurization Method. *International Journal of Photoenergy*, **2013**, e986076.

(41) Shin, B.; Gunawan, O.; Zhu, Y.; Bojarczuk, N. A.; Chey, S. J.; Guha, S. Thin Film Solar Cell with 8.4% Power Conversion Efficiency Using an Earth-Abundant Cu2ZnSnS4 Absorber. *Progress in Photovoltaics: Research and Applications*, **2013**, *21*(1), 72-76.

(42) Ito, K.; Nakazawa, T.; Electrical and Optical Properties of Stannite-Type Quaternary Semiconductor Thin Films. *Japanese Journal of Applied Physics*, **1988**, *27*(11R), 2094.

(43) Yoo, H.; Kim, J. Comparative Study of Cu2ZnSnS4 Film Growth. *Solar Energy Materials and Solar Cells*, **2011**, *95*(1), 239-244.

(44) Zhang, J.; Shao, L. Cu2ZnSnS4 Thin Films Prepared by Sulfurizing Different Multilayer Metal Precursors. *Science in China Series E: Technological Sciences*, **2009**, *52*(1), 269-272.

(45) Jimbo, K.; Kimura, R.; Kamimura, T.; Yamada, S.; Maw, W. S.; Araki, H.; Oishi, K.; Katagiri, H. Cu2ZnSnS4-Type Thin Film Solar Cells Using Abundant Materials. *Thin Solid Films, Proceedings of Symposium O on Thin Film Chalcogenide Photovoltaic Materials, EMRS 2006 Conference*, **2007**, *515*(15), 5997-5999.

(46) Katagiri, H.; Jimbo, K.; Yamada, S.; Kamimura, T.; Maw, W. S.; Fukano, T.; Ito, T.; Motohiro, T. Enhanced Conversion Efficiencies of Cu2ZnSnS4-Based Thin Film Solar Cells by Using Preferential Etching Technique. *Applied Physics Express*, **2008**, *1*(4), 041201.

(47) Liu, F.; Li, Y.; Zhang, K.; Wang, B.; Yan, C.; Lai, Y.; Zhang, Z.; Li, J.; Liu, Y. In Situ Growth of Cu2ZnSnS4 Thin Films by Reactive Magnetron Co-Sputtering. *Solar Energy Materials and Solar Cells*, **2010**, *94*(12), 2431-2434.

(48) Dhakal, T. P.; Peng, C.-Y.; Tobias, R. R.; Dasharathy, R.; Westgate, C. R. Characterization of a CZTS Thin Film Solar Cell Grown by Sputtering Method. *Solar Energy*, **2014**, *100*, 23-30.

(49) Katagiri, H.; Jimbo, K.; Washio, T. Development of Earth-Abundant CZTS Thin Film Solar Cells with Sulfurization Technique. In *Symposium E/H - Advances in the Characterization, Performance and Defect Engineering of Earth Abundant and Thin-Film Materials for Solar Energy Conversion*, **2014**, *1670.*

(50) Muhunthan, N.; Singh, O. P.; Singh, S.; Singh, V. N. Growth of CZTS Thin Films by Cosputtering of Metal Targets and Sulfurization in H2S. *International Journal of Photoenergy*, **2013**, *2013*, e752012.

(51) Inamdar, A. I.; Lee, S.; Jeon, K.-Y.; Lee, C. H.; Pawar, S. M.; Kalubarme, R. S.; Park, C. J.; Im, H.; Jung W.; Kim, H. Optimized Fabrication of Sputter Deposited Cu2ZnSnS4 (CZTS) Thin Films. *Solar Energy*, **2013**, *91*, 196-203.

(52) Wang, J.; Li, S.; Cai, J.; Shen, B.; Ren, Y.; Qin, G. Cu2ZnSnS4 Thin Films: Facile and Cost-Effective Preparation by RF-Magnetron Sputtering and Texture Control. *Journal of Alloys and Compounds*, **2013**, *552*, 418-422.

(53) Zhou, S.; Tan, R.; Jiang, X.; Shen, X.; Xu, W.; Song, W. Growth of CZTS Thin Films by Sulfurization of Sputtered Single-layered Cu-Zn-Sn Metallic Precursors from an Alloy Target. *Journal of Materials Science: Materials in Electronics*, **2013**, *24*(12), 4958-4963.

(54) Amal, M. I.; Kim, K. H. Crystallization of Kesterite Cu2ZnSnS4 Prepared by the Sulfurization of Sputtered Cu-Zn-Sn Precursors. *Thin Solid Films*, **2013**, *534*, 144-148.

(55) Ahmed, S.; Reuter, K. B.; Gunawan, O.; Guo, L.; Romankiw, L. T.; Deligianni, H. A High Efficiency Electrodeposited Cu2ZnSnS4 Solar Cell. *Advanced Energy Materials*, **2012**, *2*(2), 253-259.

(56) Scragg, J. J.; Dale, P. J.; Peter, L. M.; Zoppi, G.; Forbes, I. New Routes to Sustainable Photovoltaics: Evaluation of Cu2ZnSnS4 as an Alternative Absorber Material. *Physics Status Solidi (b)*, **2008**, *245*(9), 1772-1778.

(57) Pawar, S. M.; Pawar, B. S.; Moholkar, A. V.; Choi, D. S.; Yun, J. H.; Moon, J. H.; Kolekar, S. S.; Kim, J. H. Single Step Electrosynthesis of Cu2ZnSnS4 (CZTS) Thin Films for Solar Cell Application. *Electrochimica Acta*, **2010**, *55*(12), 4057-4061.

(58) Araki, H.; Kubo, Y.; Mikaduki, A.; Jimbo, K.; Maw, W. S.; Katagiri, H.; Yamazaki, M.; Oishi, K.; Takeuchi, A. Preparation of Cu2ZnSnS4 Thin Films by Sulfurizing Electroplated Precursors. *Solar Energy Materials and Solar Cells, 17th International Photovoltaic Science and Engineering Conference*, **2009**, *93*(6-7), 996-999.

(59) Gurav, K. V.; Shin, S. W.; Patil, U. M.; Suryawanshi, M. P.; Pawar, S. M.; Gang, M. G.; Vanalakar, S. A.; Yun, J. H.; Kim, J. H. Improvement in the Properties of CZTSSe Thin Films by Selenizing Single-Step Electrodeposited CZTS Thin Films. *Journal of Alloys and Compounds*, **2015**, *631*, 178-182.

(60) Chen, H.; Ye, Q.; He, X.; Ding, J.; Zhang, Y.; Han, J.; Liu, J.; Liao, C.; Mei, J.; Lau, W. Electrodeposited CZTS Solar Cells from Reline Electrolyte. *Green Chemistry*, **2014**, *16*(8), 3841-3845.

(61) Lee, S. G.; Kim, J.; Woo, H. S.; Jo, Y.; Inamdar, A. I.; Pawar, S. M.; Kim, H. S.; Jung, W.; Im, H. S. Structural, Morphological, Compositional, and Optical Properties of Single Step Electrodeposited Cu2ZnSnS4 (CZTS) Thin Films for Solar Cell Application. *Current Applied Physics*, **2014**, *14*(3), 254-258.

(62) Jeon, M.; Shimizu, T.; Shingubara, S. Cu2ZnSnS4 Thin Films and Nanowires Prepared by Different Single-Step Electrodeposition Method in Quaternary Electrolyte. *Materials Letters*, **2011**, *65*(15-16), 2364-2367.

(63) Tanaka, K.; Oonuki, M.; Moritake, N.; Uchiki, H. Thin Film Solar Cells Prepared by Non-Vacuum Processing. *Solar Energy Materials and Solar Cells*, **2009**, *93*(5), 583-587.

(64) Tanaka, K.; Fukui, Y.; Moritake, N.; Uchiki, H. Chemical Composition Dependence of Morphological and Optical Properties of Cu2ZnSnS4 Thin Films Deposited by Sol-Gel Sulfurization and Cu2ZnSnS4 Thin Film Solar Cell Efficiency. *Solar Energy Materials and Solar Cells*, **2011**, *95*(3), 838-842.

(65) Su, Z.; Sun, K.; Han, Z.; Cui, H.; Liu, F.; Lai, Y.; Li, J.; Hao, X.; Liu, Y.; Green, M. A. Fabrication of Cu2ZnSnS4 Solar Cells with 5.1% Efficiency via Thermal Decomposition and Reaction Using a Non-Toxic Sol-Gel Route. *Journal of Materials Chemistry A*, **2013**, *2*(2), 500-509.

(66) Park, H.; Hwang, Y. H.; Bae, B.-S. Sol-Gel Processed Cu2ZnSnS4 Thin Films for a Photovoltaic Absorber Layer without Sulfurization. *Journal of Sol-Gel Science and Technology*, **2012**, *65*(1), 23-27.

(67) Kahraman, S.; Çetinkaya, S.; Çetinkara, H. A.; Güder, H. S. A Comparative Study of Cu2ZnSnS4 Thin Films Growth by Successive Ionic Layer Adsorption-Reaction and Sol-Gel Methods. *Thin Solid Films*, **2014**, *550*, 36-39.

(68) Zhao, W.; Wang, G.; Tian, Q.; Yang, Y.; Huang, L.; Pan, D. Fabrication of Cu2ZnSn(S,Se)4 Solar Cells via an Ethanol-Based Sol-Gel Route Using SnS2 as Sn Source. *ACS Applied Materials & Interfaces*, **2014**, *6*(15), 12650-12655.

(69) Chaudhuri, T. K.; Tiwari, D. Earth-Abundant Non-Toxic Cu2ZnSnS4 Thin Films by Direct Liquid Coating from Metal-Thiourea Precursor Solution. *Solar Energy Materials and Solar Cells*, **2012**, *101*, 46-50.

(70) Mitzi, D. B.; Gunawan, O.; Todorov, T. K.; Wang, K.; Guha, S. The Path towards a High-Performance Solution-Processed Kesterite Solar Cell. Special Issue: *Thin Film and Nanostructured Solar Cells*, **2011**, *95*(6), 1421-1436.

(71) Agawane, G. L.; Kamble, A. S.; Vanalakar, S. A.; Shin, S. W.; Gang, M. G.; Yun, J. H.; Gwak, J.; Moholkar, A. V.; Kim, J. H. Fabrication of 3.01% Power Conversion Efficient High-Quality CZTS Thin Film Solar Cells by a Green and Simple Sol-Gel Technique. *Materials Letters*, **2015**, *158*, 58-61.

(72) Moriya, K.; Tanaka, K.; Uchiki, H. Cu2ZnSnS4 Thin Films Annealed in H2S Atmosphere for Solar Cell Absorber Prepared by Pulsed Laser Deposition. *Japanese Journal of Applied Physics*, **2008**, *47*(1S), 602.

(73) Moholkar, A. V.; Shinde, S. S.; Babar, A. R.; Sim, K.-U.; Kwon, Y.-B.; Rajpure, K. Y.; Patil, P. S.; Bhosale, C. H.; Kim, J. H. Development of CZTS Thin Film Solar Cells by Pulsed Laser Deposition: Influence of Pulse Repetition Rate. *Solar Energy*, **2011**, *85*(7), 1354-1363.

(74) Moriya, K.; Tanaka, K.; Uchiki, H. Fabrication of Cu2ZnSnS4 Thin-Film Solar Cell Prepared by Pulsed Laser Deposition. *Japanese Journal of Applied Physics*, **2007**, *46*(9R), 5780.

(75) Crovetto, A.; Cazzaniga, A.; Ettlinger, R. B.; Schou, J.; Hansen, O. Optical Properties and Surface Characterization of Pulsed Laser-Deposited Cu2ZnSnS4 by Spectroscopic Ellipsometry. *Thin Solid Films, EMRS 2014 Spring Meeting, Symposium A, Thin-Film Chalcogenide Photovoltaic Materials*, **2015**, *582*, 203-207.

(76) Sulaiman, C.; Suhada, N.; Nee, C. H.; Yap, S. L.; Lee, Y. S.; Tou, T. Y.; Yap, S. S. The Growth of Nanostructured Cu2ZnSnS4 Films by Pulsed Laser Deposition. *Applied Surface Science*, **2015**, *354*(A), 42-47.

(77) Ettlinger, R. B.; Cazzaniga, A.; Canulescu, S.; Pryds, N.; Schou, J. Pulsed Laser Deposition from ZnS and Cu2SnS3 Multicomponent Targets. *EMRS 2014 Spring Meeting, Symposium J: Laser Interaction with Advanced Materials: Fundamentals and Applications*, **2015**, *336*, 385-390.

(78) Zhou, Z.; Wang, Y.; Xu, D.; Zhang, Y. Fabrication of Cu2ZnSnS4 Screen Printed Layers for Solar Cells. *Solar Energy Materials and Solar Cells*, **2010**, *94*(12), 2042-2045.

(79) Dai, P.; Zhang, Y.; Xue, Y.; Jiang, X.; Wang, X.; Zhan, J.; Bando, Y. Nanoparticle-Based Screen Printing of Copper Zinc Tin Sulfide Thin Film as Photocathode for Quantum Dot Sensitized Solar Cell. *Materials Letters*, **2015**, *158*, 198-201.

(80) Wangperawong, A.; King, J. S.; Herron, S. M.; Tran, B. P.; Pangan-Okimoto, K.; Bent, S. F. Aqueous Bath Process for Deposition of Cu2ZnSnS4 Photovoltaic Absorbers. *Thin Solid Films*, **2011**, *519*(8), 2488-2492.

(81) Mali, S. S.; Shinde, P. S.; Betty, C. A.; Bhosale, P. N.; Oh, Y. W.; Patil, P. S. Synthesis and Characterization of Cu2ZnSnS4 Thin Films by SILAR Method. *Journal of Physics and Chemistry of Solids*, **2012**, *73*(6), 735-740.

(82) Gao, C.; Shen, H.; Jiang, F.; Guan, H. Preparation of Cu2ZnSnS4 Film by Sulfurizing Solution Deposited Precursors. *Applied Surface Science*, **2012**, *261*, 189-192.

(83) Suarez, H.; Correa, J. M.; Cruz, S. D.; Otalora, C. A.; Hurtado, M.; Gordillo, G. Synthesis and Study of Properties of CZTS Thin Films Grown Using a Novel Solution-Based Chemical Route. In *Photovoltaic Specialists Conference (PVSC), 2013 IEEE 39th*, **2013**, 2585-2589.

(84) Li, J.; Wang, Y.; Jiang, G.; Liu, W.; Zhu, C. Cu2MSnS4 (M: Zn, Cd, Mn) Thin Films Fabricated with Stacked Layers by CBD-Annealing Route. *Materials Letters*, **2015**, *157*, 27-29.

(85) Kameyama, T.; Osaki, T.; Okazaki, K.-I.; Shibayama, T.; Kudo, A.; Kuwabata, S.; Torimoto, T. Preparation and Photoelectrochemical Properties of Densely Immobilized Cu2ZnSnS4 Nanoparticle Films. *Journal of Materials Chemisry*, **2010**, *20*(25), 5319.

(86) Guo, Q.; Hillhouse, H. W.; Agrawal, R. Synthesis of Cu2ZnSnS4 Nanocrystal Ink and Its Use for Solar Cells. *Journal of the American Chemical Society*, **2009**, *131*(33), 11672-11673.

(87) Chernomordik, B. D.; Béland, A. E.; Trejo, N. D.; Gunawan, A. A.; Deng, D. D.; Mkhoyan, K. A.; Aydil, E. S. Rapid Facile Synthesis of Cu2ZnSnS4 Nanocrystals. *Journal of Materials Chemistry A*, **2014**, *2*(27), 10389-10395.

(88) Khare, A.; Willis, A. W.; Ammerman, L. M.; Norris, D. J.; Aydil, E. S. Size Control and Quantum Confinement in Cu2ZnSnS4 Nanocrystals. *Chemical Communications*, **2011**, *47*(42), 11721-11723.

(89) Park, J.; Song, M.; Jung, W. M.; Lee, W. Y.; Kim, H.; Kim, Y.; Hwang, C.; Shim, I.-W. Syntheses of Cu2SnS3 and Cu2ZnSnS4 Nanoparticles with Tunable Zn/Sn Ratios under Multibubble Sonoluminescence Conditions. *Dalton Transactions*, **2013**, *42*(29), 10545-10550.

(90) Steinhagen, C.; Panthani, M. G.; Akhavan, V.; Goodfellow, B.; Koo, B.; Korgel, B. A. Synthesis of Cu2ZnSnS4 Nanocrystals for Use in Low-Cost Photovoltaics. *Journal of the American Chemical Society*, **2009**, *131*(35), 12554-12555.

(91) Park, S.-N.; Sung, S.-J.; Sim, J.-H.; Yang, K.-J.; Hwang, D.-K.; Kim, J.H.; Kim, G. Y.; Jo, W.; Kim, D.-H.; Kang, J.-K. Nanostructured P-Type CZTS Thin Films Prepared by a Facile Solution Process for 3D P-N Junction Solar Cells. *Nanoscale*, **2015**, *7*(25), 11182-11189.

(92) Zhou, H.; Hsu, W.-C.; Duan, H.-S.; Bob, B.; Yang, W.; Song, T.-B.; Hsu, C.-J.; Yang, Y. CZTS Nanocrystals: A Promising Approach for Next Generation Thin Film Photovoltaics. *Energy & Environmental Science*, **2013**, *6*(10), 2822-2838.

(93) Kim, Y.; Woo, K.; Kim, I.; Cho, Y. S.; Jeong, S.; Moon, J. Highly Concentrated Synthesis of Copper-Zinc-Tin-Sulfide Nanocrystals with Easily Decomposable Capping Molecules for Printed Photovoltaic Applications. *Nanoscale*, **2013**, *5*(21), 10183-10188.

(94) Collord, A. D.; Hillhouse, H. W. Composition Control and Formation Pathway of CZTS and CZTGS Nanocrystal Inks for Kesterite Solar Cells. *Chemistry of Materials*, **2015**, *27*(5), 1855-1862.

(95) Peng, X.; Guo, W.; Zhang, S.; Xiang, Y. Solvothermal Synthesis of Cu2ZnSnS4 Nanocrystals by Using Metal Oxides. In *2014 International Symposium on Next-Generation Electronics (ISNE)*, **2014**, 1-2.

(96) Williams, B. A.; Mahajan, A.; Smeaton, M. A.; Holgate, C. S.; Aydil, E. S.; Francis, L. F. Formation of Copper Zinc Tin Sulfide Thin Films from Colloidal Nanocrystal Dispersions via Aerosol-Jet Printing and Compaction. *ACS Applied Materials & Interfaces*, **2015**, *7*(21), 11526-11535.

(97) Dai, P.; Zhang, Y.; Xue, Y.; Jiang, X.; Wang, X.; Zhan, J.; Bando, Y. Nanoparticle-Based Screen Printing of Copper Zinc Tin Sulfide Thin Film as Photocathode for Quantum Dot Sensitized Solar Cell. *Materials Letters*, **2015**, *158*, 198-201.

(98) Akhavan, V. A.; Goodfellow, B. W.; Panthani, M. G.; Steinhagen, C.; Harvey, T. B.; Jackson Stolle, C.; Korgel, B. A. Colloidal CIGS and CZTS Nanocrystals: A Precursor Route to Printed Photovoltaics. *Solution Processing Technology for Inorganic Films, Nanostructures and Functional Materials, Symposium JJ, 6th International Conference on Materials for Advanced Technologies*, **2011**, *189*, 2-12.

(99) Yoo, H.; Kim, J.H.; Comparative Study of Cu2ZnSnS4 Film Growth. *Solar Energy Materials and Solar Cells*, **2011**, *95*(1), 239-244.

(100) Kamoun, N.; Bouzouita, H.; Rezig, B. Fabrication and Characterization of Cu2ZnSnS4 Thin Films Deposited by Spray Pyrolysis Technique. *Thin Solid Films, Proceedings of Symposium O on Thin Film Chalcogenide Photovoltaic Materials, EMRS 2006 Conference*, **2007**, *515*(15), 5949-5952.

(101) Valdés, M.; Santoro, G.; Vázquez. Spray Deposition of Cu2ZnSnS4 Thin Films. *Journal of Alloys and Compounds*, **2014**, *585*, 776-782.

(102) Majeed Khan, M. A.; Kumar, S.; Alhoshan, M.; Al Dwayyan, A. S. Spray Pyrolysed Cu2ZnSnS4 Absorbing Layer: A Potential Candidate for Photovoltaic Applications. *Optics & Laser Technology*, **2013**, *49*, 196-201.

(103) Espindola-Rodriguez, M.; Placidi, M.; Vigil-Galán, O.; Izquierdo-Roca, V.; Fontané, X.; Fairbrother, A.; Sylla, D.; Saucedo, E.; Pérez-Rodríguez, A. Compositional Optimization of Photovoltaic Grade Cu2ZnSnS4 Films Grown by Pneumatic Spray Pyrolysis. *Thin Solid Films*, **2013**, *535*, 67-72.

(104) Gurieva, G.; Guc, M.; Bruk, L. I.; Izquierdo-Roca, V.; Pérez Rodríguez, A.; Schorr, S.; Arushanov, E. Cu2ZnSnS4 Thin Films Grown by Spray Pyrolysis: Characterization by Raman Spectroscopy and X-Ray Diffraction. *Physica Status Solidi (c)*, **2013**, *10*(7-8), 1082-1085.

(105) Aono, M.; Yoshitake, K.; Miyazaki, H. XPS Depth Profile Study of CZTS Thin Films Prepared by Spray Pyrolysis. *Physica Status Solidi (c)*, **2013**, *10*(7-8), 1058-1061.

(106) Rajeshmon, V. G.; Sudha Kartha, C.; Vijayakumar, K. P.; Sanjeeviraja, C.; Abe, T.; Kashiwaba, Y. Role of Precursor Solution in Controlling the Opto-Electronic Properties of Spray Pyrolysed Cu2ZnSnS4 Thin Films. *Solar Energy*, **2011**, *85*(2), 249-255.

(107) Shinde, N. M.; Deokate, R. J.; Lokhande, C. D. Properties of Spray Deposited Cu2ZnSnS4 (CZTS) Thin Films. *Journal of Analytical and Applied Pyrolysis*, **2013**, *100*, 12-16.

(108) Harsha, K. S. Principles of Vapor Deposition of Thin Films. *Elsevier*, 2005.

(109) "What Is Sputtering?" *AJA International*, **2015**. <http:// www.ajaint.com/what-is-sputtering.html>.

(110) Schwarzacher, W. "Electrodeposition: A Technology for the Future." *The Electrochemical Society, Interface*, **2006**, 32-35.

(111) Krebs, H.-U.; Weisheit, M.; Faupel, J.; Süske, E.; Scharf, T.; Fuhse, C.; Störmer M.; Sturm, K.; Seibt, M.; Kijewski, H.; Nelke, D.; Panchenko, E.; Buback, M.; Kramer, B. Pulsed Laser Deposition (PLD) — A Versatile Thin Film Technique. In *Advances in Solid State Physics* (ed. B. Kramer), **2003**, *43*, 505-518.

(112) Hodes, G. Semiconductor and Ceramic Nanoparticle Films Deposited by Chemical Bath Deposition. *Physical Chemistry Chemical Physics*, **2007**, *9*(18), 2181-2196.

(113) Sorensen, C. M.; Li, Q.; Xu, H. K.; Tang, Z. X.; Klabunde, K. J.; Hadjipanayis, G. C. Aerosol Spray Pyrolysis Synthesis Techniques. In *Nanophase Materials* (ed. G. C. Hadjipanayis and R. W. Siegel), **1994**, 109-116.

(114) Wang, W.-N.; Wuled Lenggoro, I.; Terashi, Y.; Kim, T. O.; Okuyama, K.; One-Step Synthesis of Titanium Oxide Nanoparticles by Spray Pyrolysis of Organic Precursors. *Materials Science and Engineering: B*, **2005**, *123*(3), 194-202.

(115) Exarhos, S.; Bozhilov, K. N.; Mangolini, L. Spray Pyrolysis of CZTS Nanoplatelets. *Chemical Communications*, **2014**, *50*(77), 11366-11369.

(116) Emrani, A.; Vasekar, P.; Westgate, C. R. Effects of Sulfurization Temperature on CZTS Thin Film Solar Cell Performances. *Solar Energy*, **2013**, *98*(C), 335-40.

(117) Cheng, A.-J.; Manno, M.; Khare, A.; Leighton, C.; Campbell, S. A.; Aydil, E. S. Imaging and Phase Identification of Cu2ZnSnS4 Thin Films Using Confocal Raman Spectroscopy. *Journal of Vacuum Science and Technology A*, **2011**, *29*(5), 051203.

(118) Du, H.; Yan, F.; Young, M.; To, B.; Jiang, C.; Dippo, P.; Kuciauskas, D.; Chi, Z.; Lund, E. A.; Hancock, C.; Hlaing Oo, W. M.; Scarpulla, M. A.; Teeter, G. Investigation of Combinatorial Coevaporated Thin Film Cu2ZnSnS4. I. Temperature Effect, Crystalline Phases, Morphology, and Photoluminescence. *Journal of Applied Physics*, **2014**, *115*(17), 173502.

(119) Schorr, S. Structural Aspects of Adamantine Like Multinary Chalcogenides. *Thin Solid Films, Proceedings of Sympodium O on Thin Film Chalcogenide Photovoltaic Materials, EMRS 2006 Conference*, **2006**, *515*(15), 5985-5991.

(120) Alvarez Barragan, A.; Malekpour, H.; Exarhos, S.; Balandin, A. A.; Mangolini, L. Grain-to-Grain Compositional Variations and Phase Segregation in Copper-Zinc-Tin-Sulfide Films. *ACS Applied Materials & Interfaces*, **2016**, *8*(35), 22971-22976.

(121) Just, J.; Sutter-Fella, C. M.; Lützenkirchen-Hecht, D.; Frahm, R.; Schorr, S.; Unold, T. Secondary Phases and Their Influence on the Composition of the Kesterite Phase in CZTS and CZTSe Thin Films. *Physical Chemistry Chemical Physics*, **2016**, *18*, 15988-15994.

(122) Exarhos, S.; Palmes, E.; Xu, R.; Mangolini, L. Oxide-Induced Grain Growth in CZTS Nanoparticle Coatings. *RSC Advances*, **2017**, *7*(41), 25575-25581.

(123) Valle Rios, L. E.; Neldner, K.; Gurieva, G.; Schorr, S. Existence of Off-Stoichiometric Single Phase Kesterite. *Journal of Alloys and Compounds*, **2015**, *657*, 408-413.

(124) Liu, X.; Feng, Y.; Cui, H.; Liu, F.; Hao, X.; Conibeer, G.; Mitzi, D.; Green, M. The Current Status and Future Prospects of Kesterite Solar Cells: A Brief Review. *Progress in Photovoltaics: Research and Applications*, **2016**, *24*, 879-898.

(125) Lund, E. A.; Du, H.; Hlain Oo, W. M.; Teeter, G.; Scarpulla, M. A. Investigation of Combinatorial Coevaporated Thin Film Cu2ZnSnS4. II: Beneficial Cation Arrangement in Cu-Rich Growth. *Journal of Applied Physics*, **2014**, *115*(17), 173503.

(126) Just, J.; Nichterwitz, M.; Lützenkirchen-Hecht, D.; Frahm, R.; Unold, T. Compositional Dependence of Charge Carrier Transport in Kesterite Cu2ZnSnS4 Solar Cells. *Journal of Applied Physics*, **2016**, *120*(22), 225703.

(127) Többens, D. M.; Gurieva, G.; Levcenko, S.; Unold, T.; Schorr, S. Temperature Dependency of Cu/Zn Ordering in CZTSe Kesterites Determined by Anomalous Diffraction. *Physica Status Solidi (b)*, **2016**, *253*(10), 1890-1897.

(128) Rudisch, K.; Ren, Y.; Platzer-Björkman, C.; Scragg, J. Order-Disorder Transition in B-Type Cu2ZnSnS4 and Limitations of Ordering Through Thermal Treatments. *Applied Physics Letters*, **2016**, *108*(23), 231902.

(129) Sayed, M. H.; Brandl, M.; Chory, C.; Hammer-Riedel, I.; Parisi, J.; Gütay, L.; Hock, R. In-Situ XRD Investigation of Re-Crystallization and Selenization of CZTS Nanoparticles. *Journal of Alloys and Compounds*, **2016**, *686*, 24-29.

(130) Wang, Z.; Elouatik, S.; Demopoulos, G. Understanding the Phase Formation Kinetics of Nano-Crystalline Kesterite Deposited on Mesoscopic Scaffold via In-Situ Multi-Wavelength Raman-Monitored Annealing. *Physical Chemistry Chemical Physics*, **2016**, *18*, 29435-29446.

Chapter 4: CZTS Synthesis

4.1: Precursor Solution Chemistry

CZTS nanoparticles and thin films have been produced using aerosol spray pyrolysis with two different precursor chemistries. The general necessity is to generate a miscible solution consisting of a combination of copper, zinc, and tin salts. The first precursor solution consisted of metal-diethyldithiocarbamates (dedc, $(C_2H_5)_2NCS_2$) salts. These precursor molecules are advantageous because the metal and sulfur source is contained within the same molecule, improving the thermodynamic probability that the desired metal sulfide bond would be formed upon precursor decomposition. The $Cu(dedc)_2$, $Zn(dedc)_2$, and $Sn(dedc)_4$ precursors were all synthesized in-house according to the process described in Section 4.2. The solvent for this configuration is toluene.

The solutes for the second type of precursor solution are much simpler chemically, though they require separate metal and sulfur sources. This precursor solution consisted of dissolved metal-chloride salts plus a large excess of thiourea as sulfur source. Na_2S was also added to the solution in order to attract chlorine radicals into forming NaCl to reduce the chlorine contamination to the produced CZTS nanoparticles. An excess of thiourea (~8x) was used to saturate the sulfur content of the particles so that sulfur would not be the limiting reactant in the production process. The solvent for this configuration is deionized (DI) water, and for full solubility, the thiourea must be added last.

The amounts of the precursors must be calibrated with the apparatus in order to achieve the desired CZTS stoichiometry, as the system is not 100% efficient in converting the precursors into CZTS, and the precursors decompose at different temperatures. The higher the decomposition temperature relative to the other precursors, the higher concentration of the solute is required.

A typical synthesis run using the dedc-precursors will use precursor concentrations of 14 mg/mL (2.9×10^{-2} mol/L) $Cu(dedc)_2$, 2.5 mg/mL (0.4×10^{-2} mol/L) $Sn(dedc)_4$, and 1.6 mg/mL (0.5×10^{-2} mol/L) $Zn(dedc)_2$. The precursors are dissolved in 60 mL of toluene and sonicated for >20 minutes. The $Cu(dedc)_2$ is not highly soluble in pure toluene, so a 4x excess is used to compensate for the poor solubility and the solution is kept under constant stirring during aerosolization. For the chloride-precursors, a run will use precursor concentrations of 4.0 mg/mL (2.3×10^{-2} mol/L) $CuCl_2 * 2H_2O$, 5.3 mg/mL (1.5×10^{-2} mol/L) $SnCl_4 * 5H_2O$, and 2.1 mg/mL (1.5×10^{-2} mol/L) $ZnCl_2$, 38.3 mg/mL (50×10^{-2} mol/L) CH_4N_2S, and 3.3 mg/mL (4.2×10^{-2} mol/L) Na_2S. The precursors are dissolved in 60 mL of DI water in strictly the order they are listed here and sonicated for >20 minutes.

The composition of the CZTS product can be controlled by varying the relative precursor ratios. By increasing the amount of $Cu(dedc)_2$ relative to $Zn(dedc)_2$ and $Sn(dedc)_4$, the resulting powder stoichiometry increases in copper relative to zinc plus tin (this will be shown in Section 4.4). Doping of CZTS using the synthesis method described below can also be achieved by including various additives to the precursor solution.

4.2: Precursor Synthesis

In the case of the dedc-precursors, they are synthesized in-house according to the recipe outlined by Khare *et al.*[1] In essence, sodium diethyldithiocarbamate is mixed drop-wise with zinc, tin, and copper chlorides respectively to induce an ion-replacement reaction to form sodium chloride and metal-diethyldithiocarbamate products, which are then cleaned and purified to isolate the desired material.

To form $Zn(dedc)_2$ (white), 9.0 g of Na(dedc) is dissolved in 150 mL of ethanol. Concurrently, 3.38 g of $ZnCl_2$ is dissolved in 50 mL of ethanol. The Na(dedc) solution is added drop-wise to the zinc chloride solution under constant stirring via a burette. Upon completion of the titration, the product is stirred for a further ten minutes, followed by ten minutes of sonication, to ensure the reaction has progressed to completion. The product is then washed in ethanol and DI water, separated via centrifuge, and washed again until the product has been washed five times. The product is then dissolved in chloroform and dried under argon flow. The synthesized $Zn(dedc)_2$ is fully decomposed above 334 ºC (Fig. 1).

To form $Sn(dedc)_4$ (orange), 12.85 g of Na(dedc) is dissolved in 200 mL of ethanol. Concurrently, 3.0 mL of $SnCl_4$ is dissolved in 50 mL of ethanol. The Na(dedc) solution is added drop-wise to the tin chloride solution under constant stirring via a burette. Upon completion of the titration, the product is stirred for a further ten minutes, followed by ten minutes of sonication, to ensure the reaction has progressed to completion. The product is then washed in ethanol and DI water, separated via centrifuge, and washed again until the product has been washed five times. The product is then

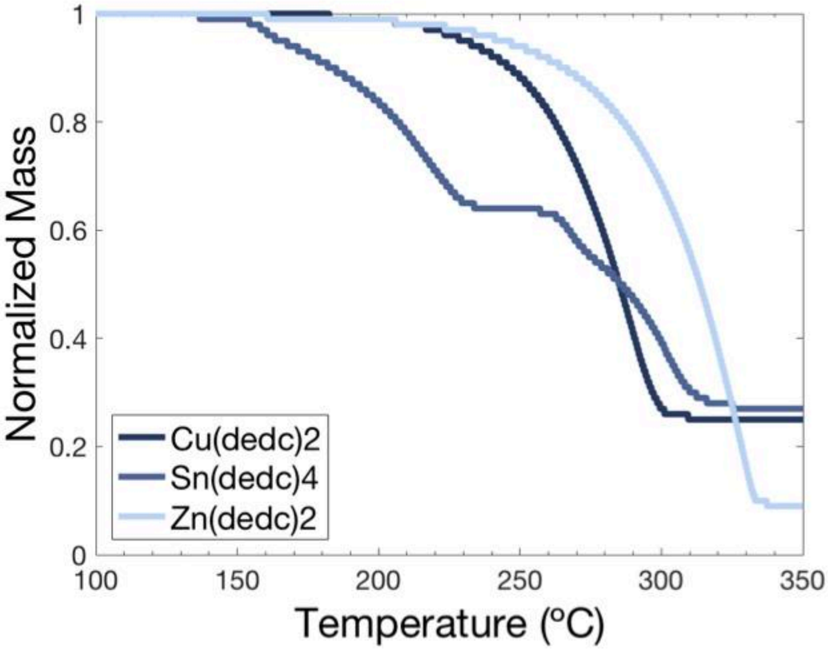

Figure 1: Shows thermogravimetric analysis and decomposition of $Zn(dedc)_2$ (light blue), $Sn(dedc)_4$ (mid-blue), and $Cu(dedc)_2$ (dark blue) with temperature.

dissolved in chloroform and dried under argon flow. The synthesized $Sn(dedc)_4$ is fully decomposed above 318 ºC (Fig. 1).

To form $Cu(dedc)_2$ (dark green/black), 9.0 g of Na(dedc) is dissolved in 150 mL of ethanol. Concurrently, 4.23 g of $CuCl_2$ is dissolved in 50 mL of ethanol. The Na(dedc) solution is added drop-wise to the copper chloride solution under constant stirring via a burette. Upon completion of the titration, the product is stirred for a further ten minutes, followed by ten minutes of sonication, to ensure the reaction has progressed to completion. The product is then washed in ethanol and DI water, separated via centrifuge, and washed again until the product has been washed five times. The product is then dissolved in chloroform and dried under argon flow. The synthesized $Cu(dedc)_2$ is fully decomposed above 302 ºC (Fig. 1).

4.3: CZTS Thin Film Synthesis

To synthesize CZTS thin films, the spray pyrolysis apparatus is assembled as shown in Fig. 2 and the dedc precursor solution described above is used. The location of the substrate within the furnace allows for crystal nucleation and growth in one step, theoretically removing the need for an annealing step in a sulfur-rich atmosphere.

The precursor solution is aerosolized by the pressure differential caused by the flow of the carrier gas through the nebulizer head. In this apparatus, a one-jet nebulizer head is used, so the carrier gas (Ar) flow rate is limited to ~0.5 SCFH (~200 SCCM). The aerosol is then pulled through an aperture (diameter of 1/8") and directed onto a substrate, fastened onto a stainless steel mount. The excess non-decomposed precursor, carrier gas, and decomposed dedc complexes are then pulled through the furnace by a rotary vane vacuum pump and filtered by a liquid nitrogen trap, before proceeding to an exhaust tube.

The system is kept at an ambient pressure of ~225 torr during runs, measured on

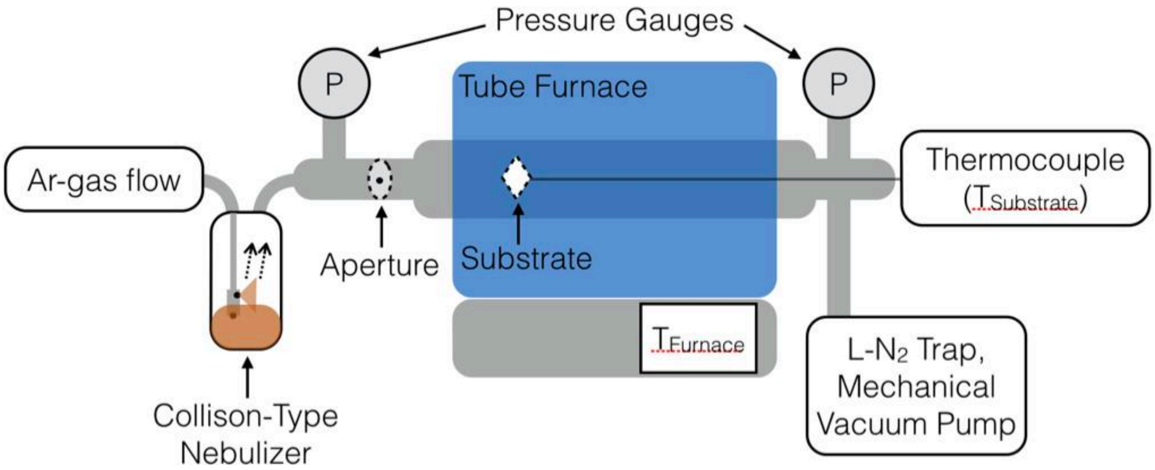

Figure 2: Schematic of aerosol spray pyrolysis system used to synthesize CZTS thin films.

both sides of the furnace. Molybdenum-coated soda lime glass is the substrate of choice, as it makes an effective base for a PV cell. Further, the sodium in the glass is diffusively active and has been shown to enhance CZTS grain growth when present in high dopant concentrations.[2] The furnace is set within a range of 350-500 ºC. Temperatures lower than this run the risk of not fully decomposing the precursors, while temperatures higher than this run the risk of damaging the molybdenum coating on the substrate. The location of the substrate within the furnace is variable. The system is typically run with the substrate a distance of ~45 cm away from the nebulizer port. The substrate temperature is measured approximately by a thermocouple that is threaded through to touch the back side of the substrate mount. The substrate temperature is measured to be consistently 20 ºC below the ambient temperature of the furnace, which is attributed to the cooling effect of the aerosol and carrier gas colliding with the substrate. The system is allowed to run until the nebulizer jar is empty, or as long as the user desires, depending on the desired thickness of the film. At the completion of a run, the carrier gas is stopped, the nebulizer is shut off from the furnace tube by a quarter-turn valve, and the furnace tube is pumped constantly until the furnace drops to a temperature below 300 ºC. The system is then opened, the substrate is removed, and the resulting film is characterized.

We have demonstrated that spray pyrolysis is not an effective method to synthesize CZTS thin films, and disseminated our results in.[3] Effectively, at low temperatures (~350-400 ºC), there is minimal film deposition, likely due to the incomplete deposition of the precursors. At higher temperatures, the deposited material nucleates non-uniformly, particularly above ~440 ºC, at which point quasi-two-dimensional platelet structures nucleate above the substrate (Fig. 3). This result has been observed using multiple different spray pyrolysis and precursor configurations since our initial discovery.[4-6]

The dominant variable associated with the structure and morphology of these films is temperature. Within a small temperature range (~350-500 ºC), there is an immense morphological development, ranging from a film of negligible thickness grown at 350 ºC, to a very complex morphological structure that is made up of quasi-two-dimensional platelet structures in a disordered arrangement that increases the effective film thickness to 5-10 µm seen in films grown above 440 ºC.

The same apparatus and procedure have also been used to synthesize binary

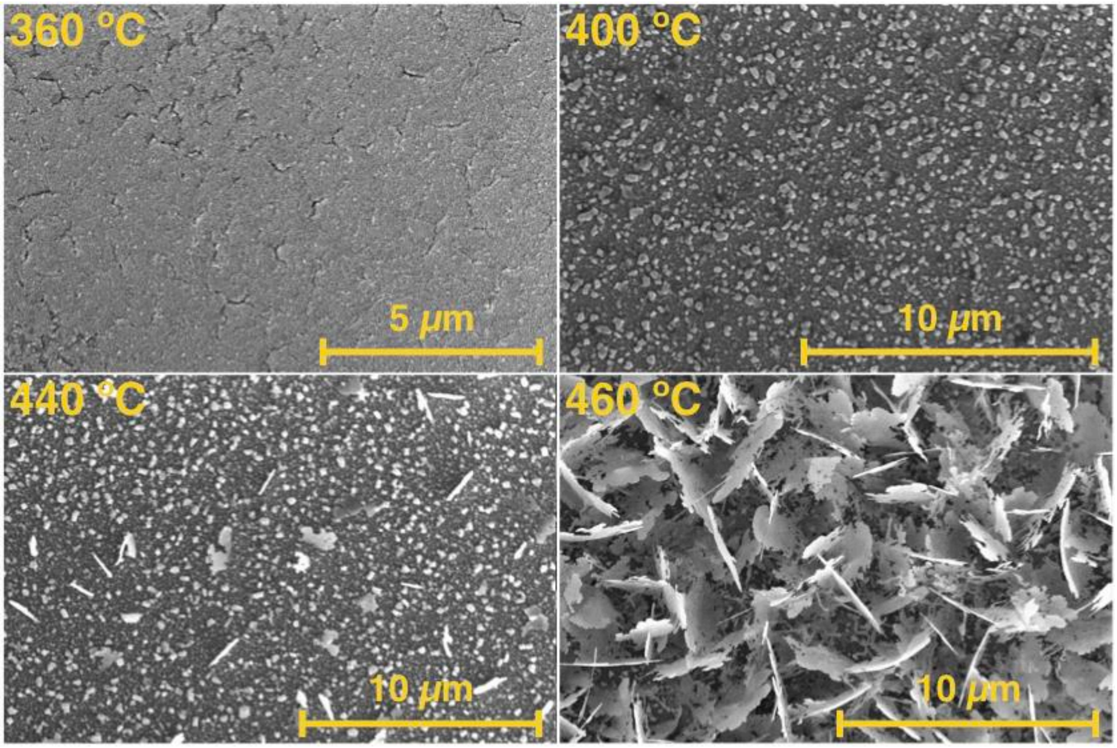

Figure 3: SEM micrographs of samples grown on molybdenum-coated soda lime glass at various temperatures.

copper sulfide, tin sulfide, and zinc sulfide films. From these films, we attribute the platelet formation and nucleation to the presence of a copper sulfide phase. For tin sulfide and zinc sulfide films, nanostructured isotropic growth is observed. It is only in copper sulfide films where anisotropic growth is observed (Fig. 4).

Films synthesized at various temperatures within this growth range have been characterized extensively. XRD scans of a sample with a prevalence of the platelet structures indicates the presence of kesterite-phase CZTS, while absorption spectroscopy measurements allow the estimation of the material's band gap via a Tauc plot, found to be ~1.5 eV (Fig. 5), consistent with literature for CZTS.[1] While the characteristic kesterite CZTS peaks in XRD align well with those in Fig. 5a, this by itself is not conclusive proof of phase-pure CZTS.[8] The diffraction pattern for kesterite CZTS matches well with peaks for other binary and ternary sulfides, like ZnS and Cu_2SnS_3, making differentiation between the phases difficult. In combination with Raman spectroscopy, though, it is easier to be conclusive about the phase of the material.[8]

Raman spectroscopy of samples grown across the 350-500 ºC temperature range

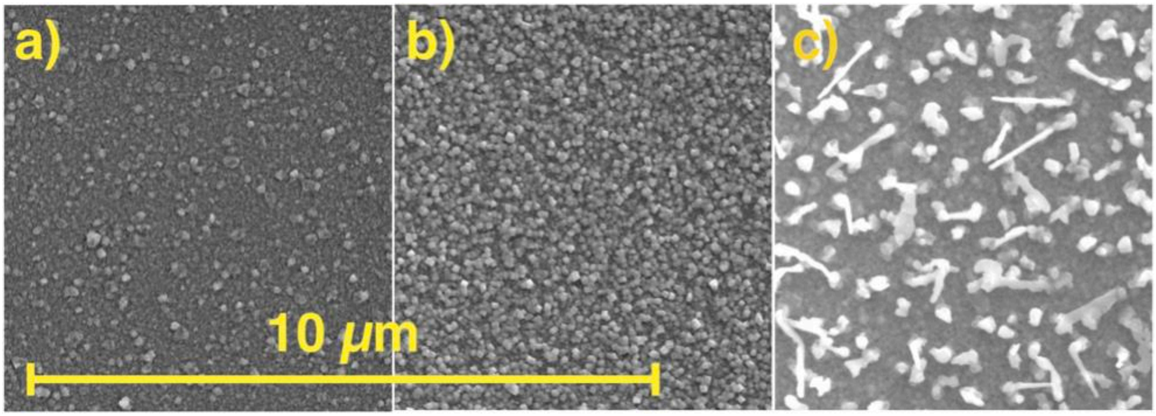

Figure 4: SEM micrographs of a) zinc sulfide, b) tin sulfide, and c) copper sulfide samples grown on molybdenum-coated soda lime glass each at 450 ºC.

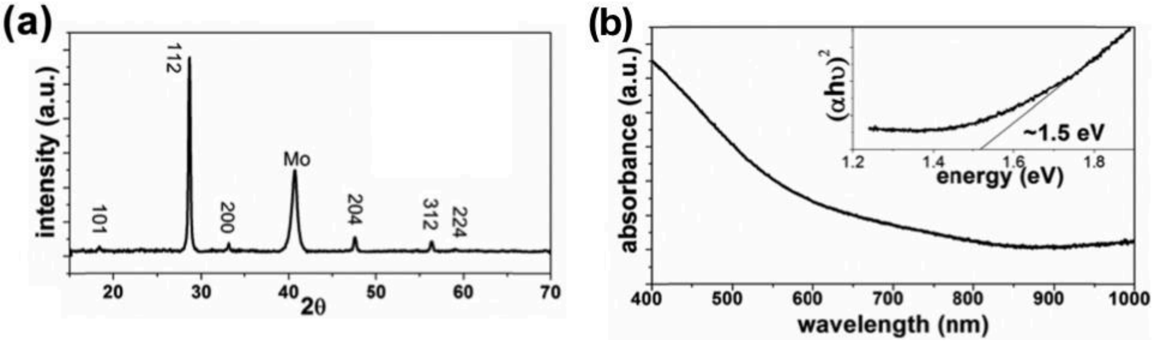

Figure 5: a) XRD of the sample grown at 460 ºC (see fig. 4.1.1). b) UV-vis absorbance for the sample grown at 460 ºC. The Tauc plot generated using the spectrum is shown in the inset.

shows in interesting development as temperature is increased. At the lower temperatures (360, 400 ºC, the spectra show the presence of crystalline CZTS, but also molybdenum sulfide (MoS_2), suggesting that some of the precursors have decomposed, but the most thermodynamically favorable reaction is with the molybdenum substrate instead of with the other metal cations present. At the higher temperatures (440, 460 ºC), the MoS_2 peak disappears, and the CZTS peaks at 288, 338, and 380 cm^{-1} are sharper and more well-defined (Fig. 6).

Elemental analysis of large areas on these films provides further support to the hypothesis that at lower temperatures, the failure of film growth is due to the lack of precursor decomposition. Noting that the highest precursor decomposition temperature is 334 ºC for $Zn(dedc)_2$ (Fig. 1), at the lower processing temperatures, there is an excess of copper — the precursor with the lowest decomposition temperature at 302 ºC (Fig. 1). At higher temperatures, the [Cu]/([Zn]+[Sn]) ratio levels out to ~1, which is ideal for stoichiometric CZTS (Table 1). The elemental analysis was performed on areas of ~100 μm^2, meaning that any phase instability on individual platelets leading to local compositional inhomogeneity is inconsequential.

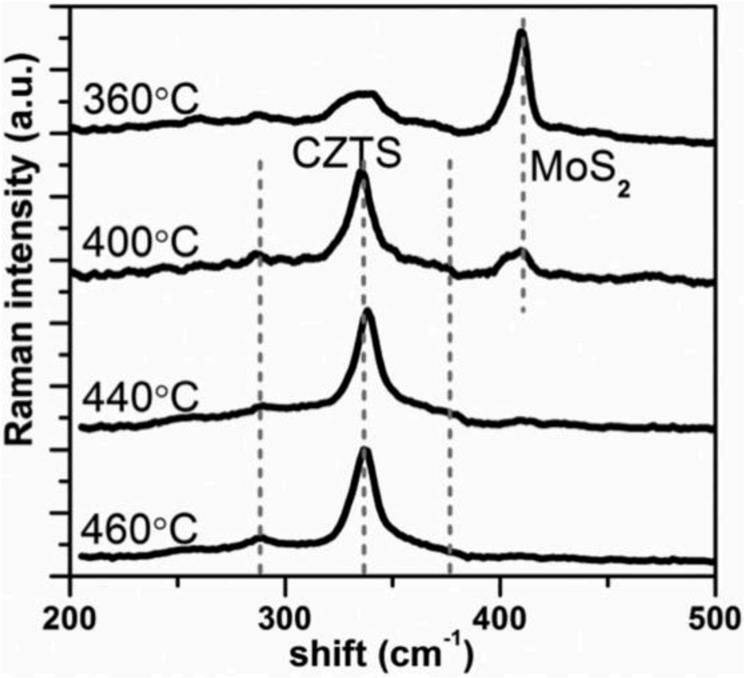

Figure 6: Thin film Raman spectra as a function of temperature.

Table 1: Summary of the results from the elemental analysis performed by EDS on samples grown at different temperatures. The values correspond to atomic percentages and to their ratios.

T (°C)	At. % Cu	At. % Zn	At. % Sn	At. % S	$\frac{[Cu]}{[Zn]+[Sn]}$	$\frac{[Zn]}{[Sn]}$
360	38.1(±1.6)	15.5(±0.6)	6.8(±0.5)	39.5(±2.0)	1.70	2.2
400	34.8(±0.8)	21.9(±0.5)	8.7(±0.3)	35.4(±1.6)	1.13	2.5
440	25.7(±0.8)	25.0(±0.7)	9.5(±0.5)	39.7(±1.9)	0.75	2.6
460	29.8(±1.0)	21.0(±0.6)	10.5(±0.4)	38.7(±1.6)	0.94	2.0

Elemental analysis has also been performed on individual platelets in TEM (Fig. 7). The platelets are clearly crystalline, though the selected area electron diffraction pattern suggests that multiple phases are present within a single platelet. Elemental mapping suggests that the bulk of the platelets could be kesterite CZTS, while the phase

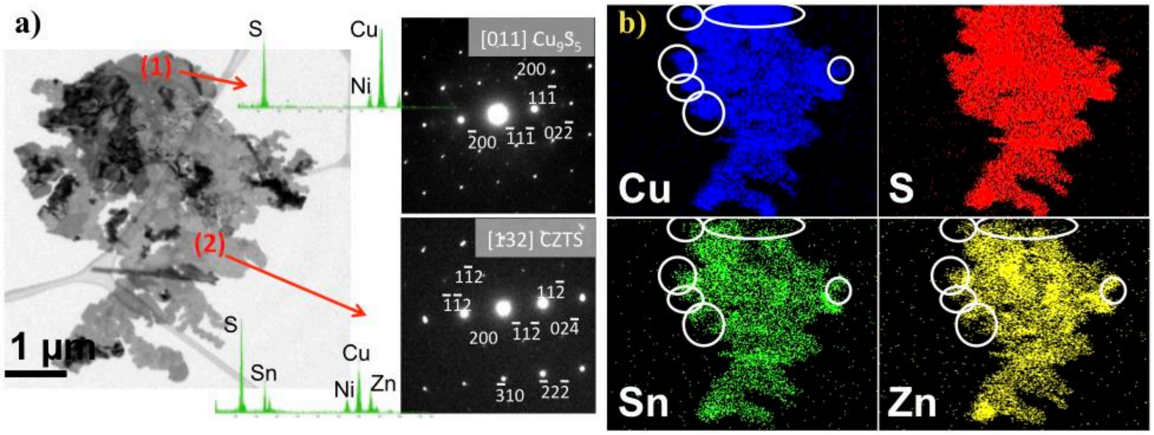

Figure 7: (a) TEM of a nanoplatelet grown at 460 ºC. EDS scans and selected area diffraction pattern for two spots are also shown. (b) Elemental mapping for the platelet in (a) showing the variation in the local composition.

impurity is focused on the edges, where an excess of copper relative to zinc and tin is seen.

It is hypothesized that the copper sulfide initially nucleates as a binary sulfide because the corresponding precursor has the lowest decomposition temperature. Once the copper sulfide has nucleated, it is thermodynamically stable, and will not change phase, though it appears to catalyze the formation of anisotropic platelet growth and the formation of kesterite CZTS.

While interesting, these findings suggest that aerosol spray pyrolysis is an ineffective method for synthesizing CZTS thin films for PV applications. In order to make an effective PV, it is necessary for the interface between each layer to have exceptional contact, so that little charge is lost between the different materials. Since the inherent problem with the application of the CZTS material system to PVs lies in charge loss and bulk defects within the material, an alternative method of CZTS synthesis — nanoparticle formation and sintering — has been explored.

4.4: CZTS Nanoparticle Synthesis

Using aerosol spray pyrolysis to synthesize CZTS nanoparticles appears to be more advantageous than using the process to synthesize CZTS films, mainly due to its economic and scalable application to the technology's marketability. The process can be separated into a few distinct steps to go from precursor material through to uniform, crystalline CZTS thin films. Discussed here are results found when attempting to synthesize and control the composition of CZTS nanoparticles.

To synthesize CZTS nanoparticles, the spray pyrolysis apparatus is assembled as shown in Fig. 8. The powder can be collected either on a stainless steel mesh filter or in solvent-filled bubblers. The mesh filter is easier to use and collects more powder, but the bubblers quench the powder and eliminate contamination from interaction with hot stainless steel parts. Using either collection technique, the system is operated at atmospheric pressure under an inert argon atmosphere.

The precursor solution is aerosolized by the pressure differential caused by the

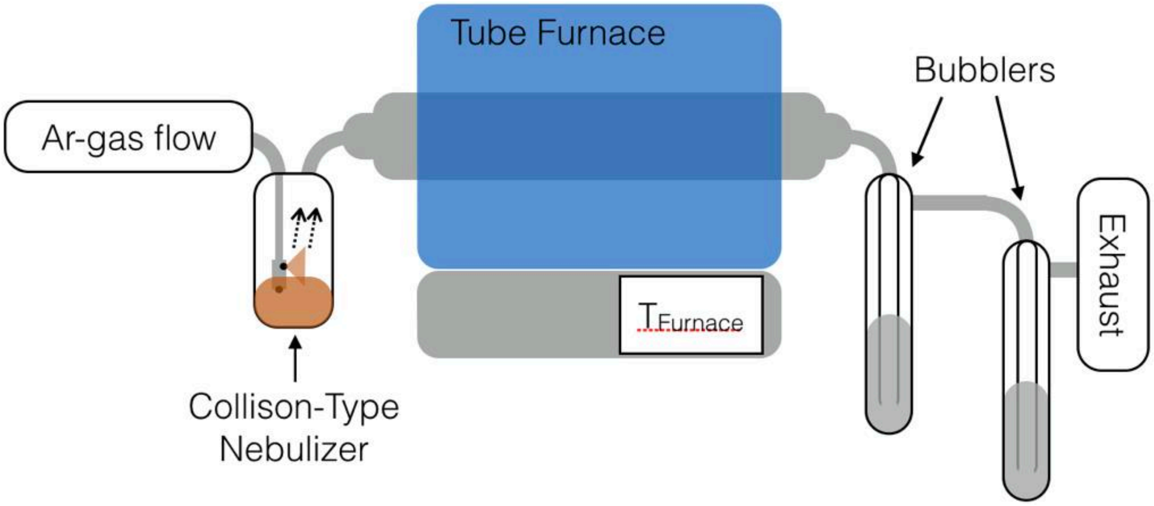

Figure 8: Schematic of spray pyrolysis system used to synthesize CZTS nanoparticles.

flow of the carrier gas through the nebulizer head. In this apparatus, a six-jet nebulizer head is used, the carrier gas (Ar) flow rate is set to ~15 SCFH (~5,700 SCCM) for each run, which gives the aerosol droplets a residence time on the order of 100 ms within the furnace. The aerosol is pushed into the tube furnace via the carrier gas, where the thermal conditions are such that precursors decompose and form CZTS particles. The particles, along with the excess non-decomposed precursor, carrier gas, and decomposed precursor molecules are then collected by either technique mentioned above.

The solid material collected is washed five times and centrifuged with toluene and methanol (in the case of the dedc precursor recipe from Section 4.2) or with DI water and ethanol (in the case of the chloride precursor recipe from Section 4.2) to dissolve any remaining precursor or precursor residue that may have formed. The remaining particles are then dispersed in methanol and dried under argon flow. The material can then be characterized accordingly.

The optimal temperature at which to synthesize CZTS nanoparticles using this system is 800 ºC. At lower temperatures, the mass of particles recovered diminishes significantly, while at higher temperatures, the particles are found to be embedded in an amorphous carbon matrix.

We have shown the ability to consistently create crystalline kesterite-CZTS nanoparticles with a narrow size distribution centered around ~23 nm in diameter using the dedc-precursor configuration (Fig. 9). Further characterization of these particles via XRD and Raman confirms the presence of kesterite-phase CZTS (Fig. 10).

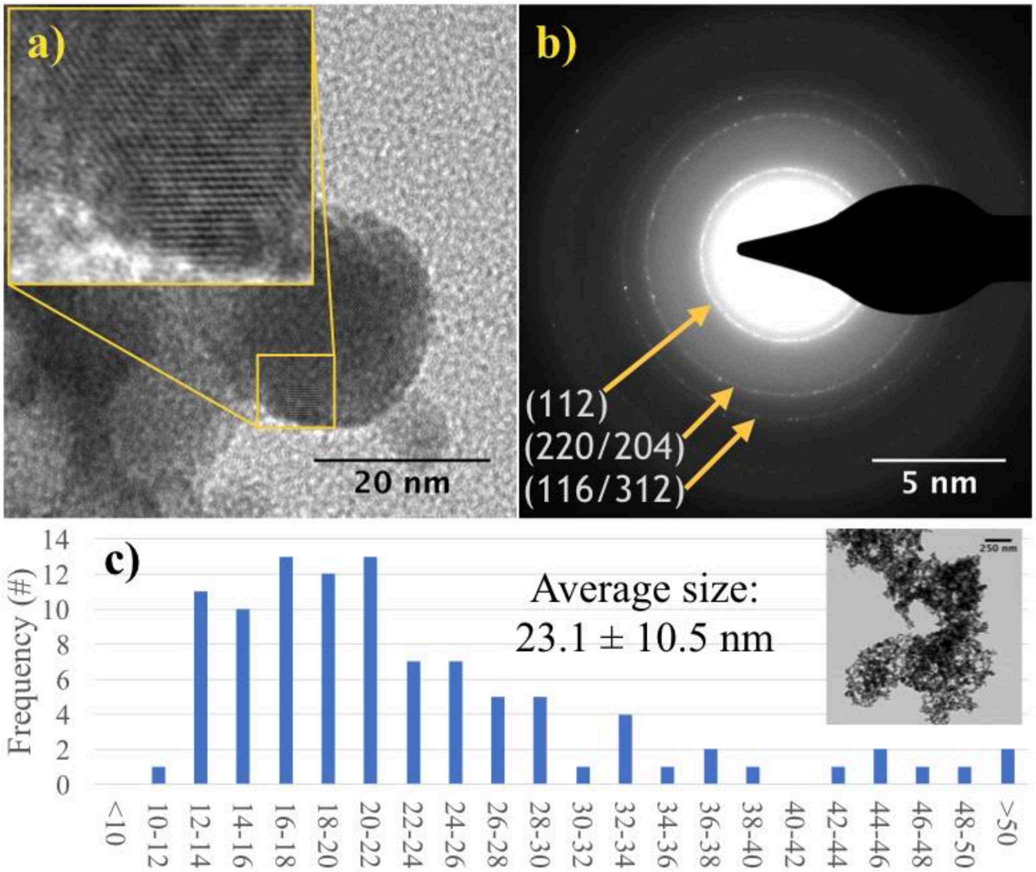

Figure 9: (a) TEM of a nanoparticle grown at 800 ºC. Inset provided to better observe uniform crystal fringes. (b) Diffraction pattern of particle shown in (a), three primary fringes align well with major kesterite-CZTS peaks. (c) Shows histogram of nanoparticle sizes constructed from the inset image. The average particle size is 23.1 ± 10.5 nm.

With the ability to synthesize nanocrystalline CZTS confirmed, the controllability of the system needed to be assessed. To do this, the system was run with one parameter varied at a time. Running at different furnace temperatures and using altered precursor ratios in the precursor solution (i.e. the amount of Cu(dedc)$_2$ relative to Zn(dedc)$_2$ and Sn(dedc)$_4$) are the most significant variables in tuning the composition, size, and morphology of the particles. By running the system at temperatures between 400 ºC and

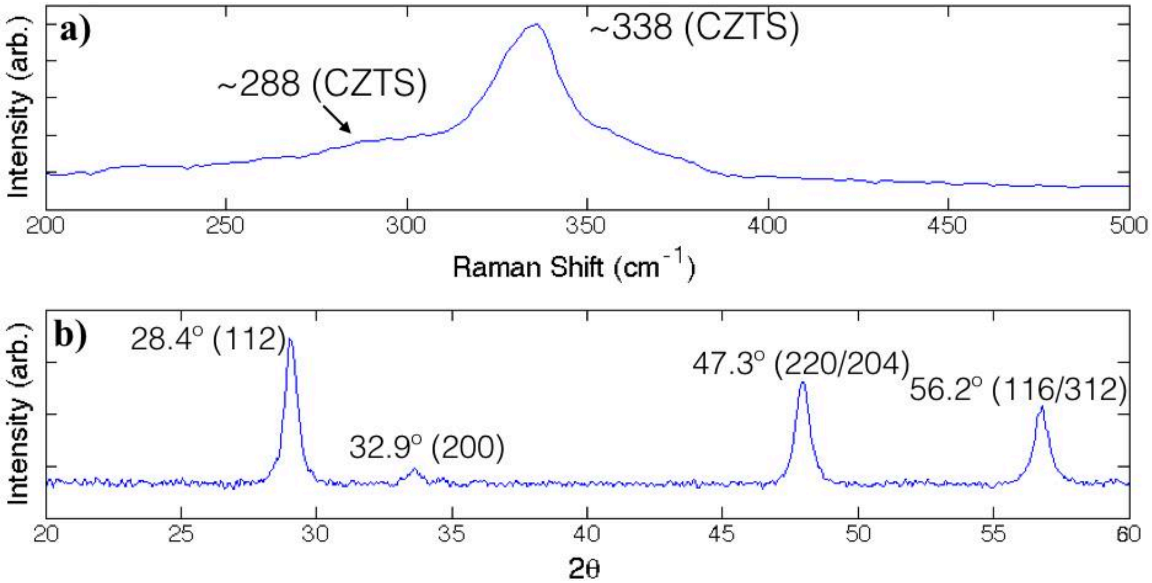

Figure 10: (a) Shows a Raman spectrum of nanoparticles grown at 800 ºC and (b) XRD pattern of the same nanoparticles.

1,000 ºC, the optimal operating temperature was determined to be 800 ºC. All further samples discussed in this section were produced at this temperature.

Below this optimal temperature, there is a marked decline in the amount of powder produced and collected, implying that the precursor doesn't fully decompose at lower temperatures. While the furnace is set above the decomposition temperature for all three precursors even at 400 ºC, the residence time of the aerosol droplets within the furnace is too short (~0.12 s) to allow an adequate amount of thermal energy to be radiated into the droplets to cause decomposition of the precursors, hence the higher temperature is necessary. The crystalline powder collected at lower temperatures is still evidently kesterite-CZTS as confirmed by Raman spectroscopy (Fig. 11).

Above the optimal 800 ºC temperature, the powder is still formed as crystalline CZTS, but TEM indicates that the powder is embedded in an amorphous matrix (Fig. 12). Cursory analysis via Fourier Transform Infrared Spectroscopy indicates that the

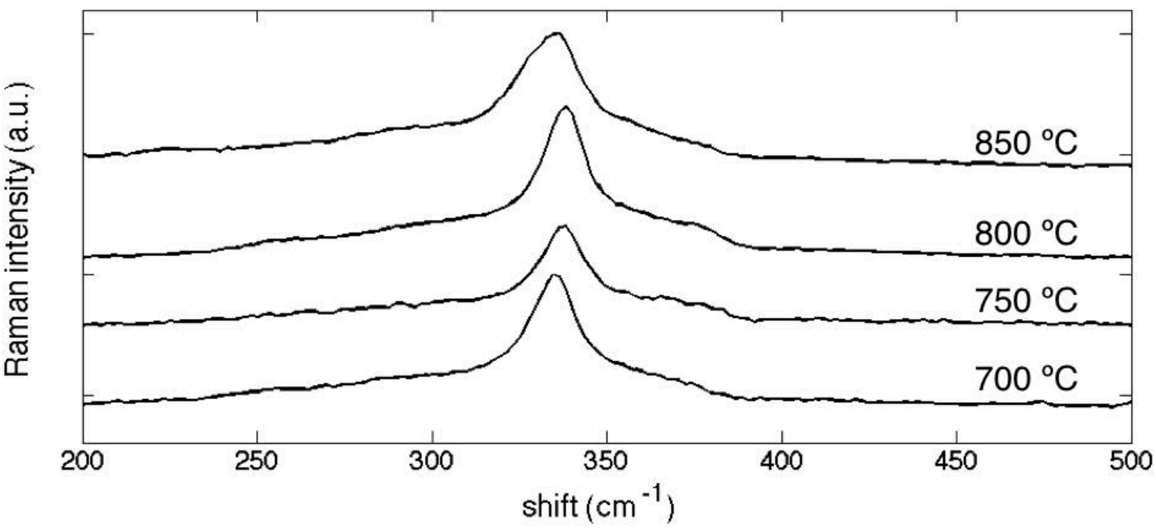

Figure 12: Shows Raman spectra of CZTS nanopowders grown at various temperatures.

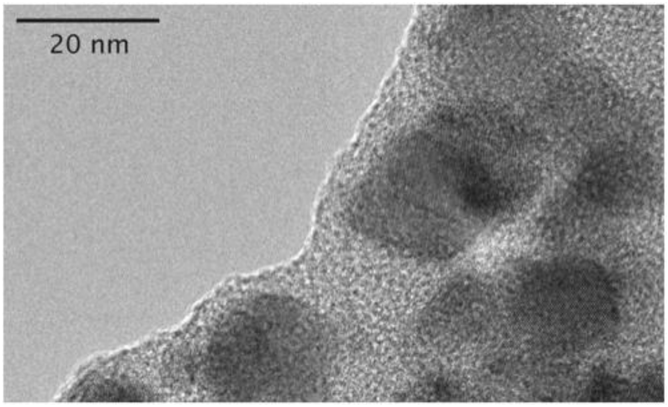

Figure 11: TEM micrograph of sample grown at 900 ºC showing crystalline CZTS powder embedded in amorphous matrix.

amorphous material is likely organic in composition, making it an undesirable contaminant for the proposed application of this material system (Fig. 13).

Then, by running the spray pyrolysis system with variable relative precursor ratios, the controllability of the material composition has been examined. The nanoparticle stoichiometry has been shown to be highly controllable, though it is clear that the system is incapable of converting all of the precursor into CZTS effectively, as

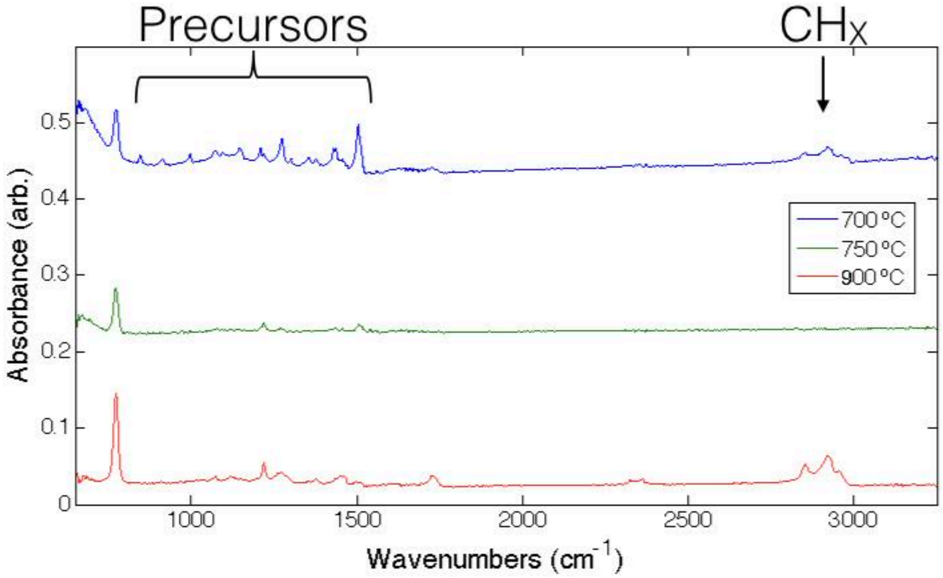

Figure 13: FTIR spectra of CZTS nanopowder samples produced at 700, 750, and 900 ºC. The 700 ºC sample shows a significant presence of unreacted dedc precursor complexes, and the 900 ºC sample shows a strong presence of CH_x bonds correlated with the amorphous matrix seen in Fig. 11. The 750 ºC sample shows neither of these features.

observed in Table 2 — a summary of EDS analysis performed on powder formed with varied precursor concentrations.

Perfect precursor conversion would yield the ideal relative copper : zinc : tin ratio with a relative $Cu(dedc)_2$: $Zn(dedc)_2$: $Sn(dedc)_4$ mass ratio of approximately 2:2:1 (used

Table 2: Summary of the results from the EDS performed on samples grown from different precursor ratios.

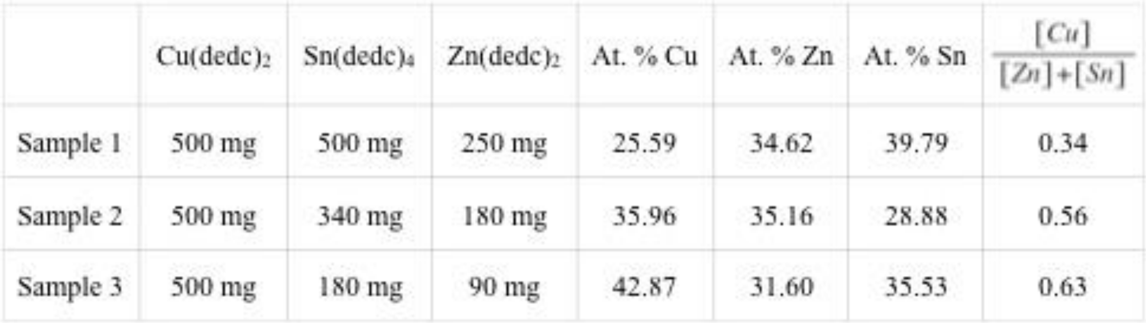

	$Cu(dedc)_2$	$Sn(dedc)_4$	$Zn(dedc)_2$	At. % Cu	At. % Zn	At. % Sn	$\frac{[Cu]}{[Zn]+[Sn]}$
Sample 1	500 mg	500 mg	250 mg	25.59	34.62	39.79	0.34
Sample 2	500 mg	340 mg	180 mg	35.96	35.16	28.88	0.56
Sample 3	500 mg	180 mg	90 mg	42.87	31.60	35.53	0.63

in Sample 1 of Table 2). However, ideal CZTS stoichiometry was approached as both tin and zinc precursors were decreased relative to copper precursor, implying the copper precursor is more difficult to convert than the others. This is likely due to the fact that Cu(dedc)$_2$ has been observed to be imperfectly soluble in toluene at the concentrations we are using, so there is a depletion of this precursor in the aerosol droplets unless its relative concentration is increased.

This data provides evidence that the aerosol spray pyrolysis system described here is capable of controllably producing phase-pure kesterite-CZTS.

4.5: CZTS Nanoparticle Sintering

To create thin films from CZTS nanoparticles, it is necessary to coat the particles uniformly on a substrate. In this work, CZTS nanoparticle dispersions in methanol are sprayed onto substrate using a Master$^{®}$ airbrush.

The dry CZTS nanoparticles are well-dispersed in methanol by ultrasonicating for >15 minutes. The solution is then added to the airbrush reservoir and is turned into an aerosol and sprayed onto a substrate. Compressed argon is used to generate the aerosol. To achieve a uniform coating, it is necessary to run the carrier gas at a low flow rate; here ~1 SCFH (~380 SCCM) is used. The spray is directed onto a masked substrate in a uniform pattern until the desired thickness is achieved. An exemplary coating is shown in Fig. 14, both at the macro- and the micro-scale.

Coatings have been deposited on both soda lime glass and quartz substrates. The substrate is masked over a rectangular area using masking tape, which also served to hold

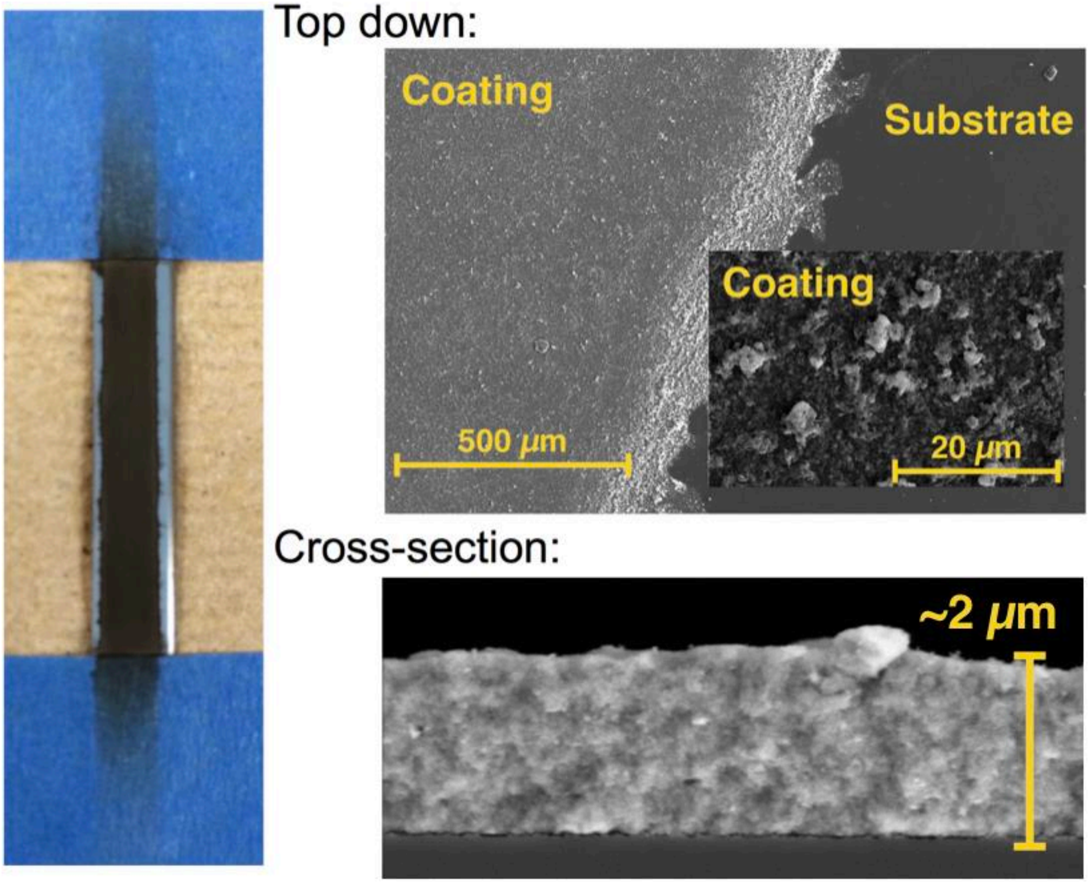

Figure 14: Macroscopic, SEM top down, and SEM cross section images of a coating of CZTS nanoparticles created using the process outlined in Section 4.4.

the substrate immobile and level. The substrate is also made twice as large as the desired film area and is pre-scored. This is to allow easy splitting of the substrate and coating to give a control sample, as well as one that will be annealed.

Once the CZTS nanoparticles have been coated onto a substrate, the sample must be baked in a sulfur-rich atmosphere to promote crystal grain formation and growth, as discussed in Section 3.8. To do this, the samples are sealed in an evacuated ampoule with some solid sulfur and placed inside a tube furnace for an hour.

The samples are placed in a 1/4” diameter quartz tube with one end that has been sealed shut. Approximately 1 mg of sulfur is added to the tube, which when heated to 600 ºC will yield roughly 50 torr of sulfur pressure within the sealed and evacuated ampoule (the boiling point of sulfur is 445 ºC).[9]

The quartz tube is then joined to an airtight apparatus via a Swagelok Ultra-Tour fitting to be pumped down to ~10^{-5} torr by a Leybold turbo-molecular pump (Fig. 15a). The ampoule is then closed off from the system by a quarter-turn valve. The ampoule plus valve assembly is then removed from the apparatus and the ampoule is sealed off using an oxygen-acetylene torch so that the ampoule is 8" long (Fig. 15b).

The sealed ampoule is then inserted into a tube furnace ramped to 600 ºC at a rate of 5 ºC/min. and then baked for 60 minutes. At the end of the time, the furnace is allowed to cool slowly (~5 ºC/min.). This slow cooling rate is necessary to preserve order and crystal phase integrity in the material, as discussed in Section 3.10.

Once the furnace has cooled below the "order/disorder transition temperature" at ~206 ºC, the ampoule is extracted from the furnace and quenched. Once cooled, the ampoule is cracked open and the sample is removed and characterized.

Attempts at making uniform, large-grain CZTS films based on the powder as-

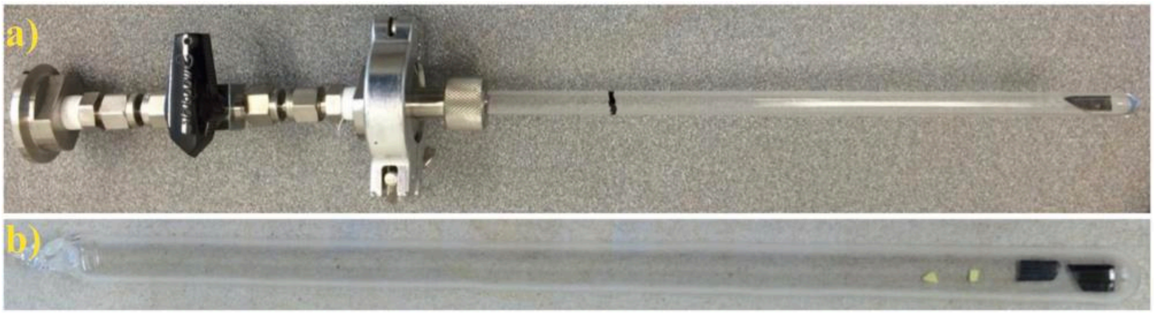

Figure 15: a) Shows an ampoule loaded with sample and elemental sulfur after pumping down to 10^{-5} torr. b) Shows an ampoule that has been sealed off to be eight inches long from image a.

produced from the aerosol spray pyrolysis system with no post-treatment other than solvent rinsing and centrifuging have proven unsuccessful. A typical result is shown in Fig. 16. There is some grain growth in the bulk of the film, the uniform-looking grains in the background have an average size of 230 ± 50 nm. Further, the background layer is porous and thin. From a cross-section SEM image, the thickness of this layer is approximated at less than 1 µm, while the initial coating before annealing had a thickness of approximately 3.5 µm. The annealed film is also non-uniform. There are sparse occurrences of very large grains segregated above the bulk of the film. Volume conservation suggests that the massive reduction in the thickness of the bulk of the film can be explained by material loss to these large grains that extend as high as 5 µm above the surface of the bulk film. A similar result is noted by Chernomordik *et al.* in the sintering of ligand-capped pure sulfide CZTS nanoparticle films.[10]

4.6: Oxide-Induced Grain Growth

In order to investigate the role of surface chemistry on the sintering kinetics of

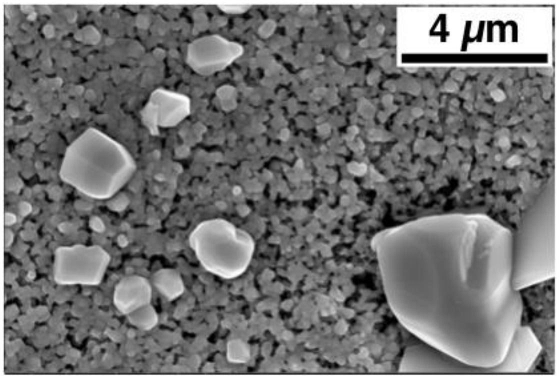

Figure 16: Top-down SEM micrograph of sulfur-annealed CZTS nanoparticles with no post-synthesis treatment.

CZTS nanoparticles, we have tested a very simple air-annealing process. This was originally motivated by the idea that such a process would remove any residual trace amount of carbon contamination, due to either solvent residue or unreacted precursor not removed by the cleaning procedure. The annealing temperature range is between 200 and 300 ºC. Fig. 17 shows the effect of the air annealing process on particle morphology for two different temperatures (225 ºC and 300 ºC) relative to the as-produced particles.

At 225 ºC (Fig. 17b), there is a clear modification to the particle surface, and at 300 ºC (Fig. 17c), the formation of a thin amorphous layer is thicker (~1.5 nm) and clearly distinguishable. It should be stressed that the bulk of the material retains the apparent phase-pure CZTS character, as confirmed by XRD and Raman spectroscopy (Fig. 18).

XPS characterization confirms that the amorphous layer on the surface of the particles is an oxide primarily comprised of tin and zinc cations (Fig. 19). From Fig. 19, it is also interesting to note that the surface of air-annealed particles tends to be more rich in

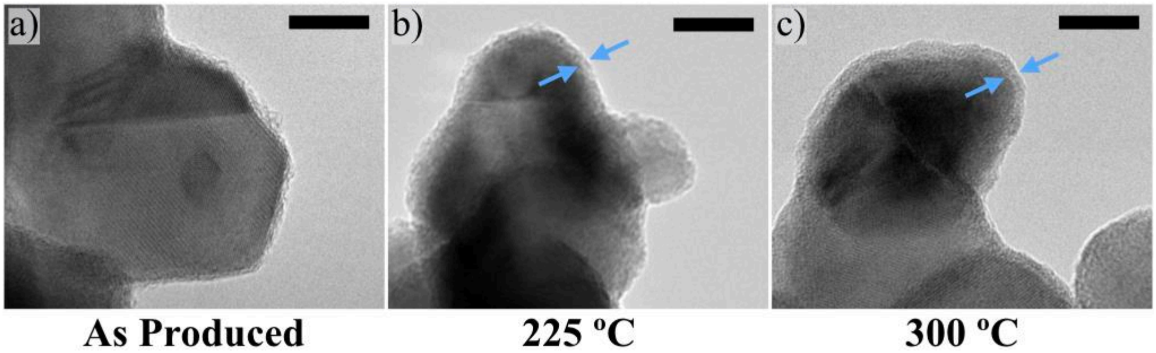

Figure 17: TEM micrographs of CZTS nanoparticles as-produced from the spray pyrolysis reactor (a), after annealing in air at 225 ºC (b), and after annealing in air at 300 ºC (c). Arrows indicate presence of amorphous oxide layer after air annealing. Scale bar is 10 nm.

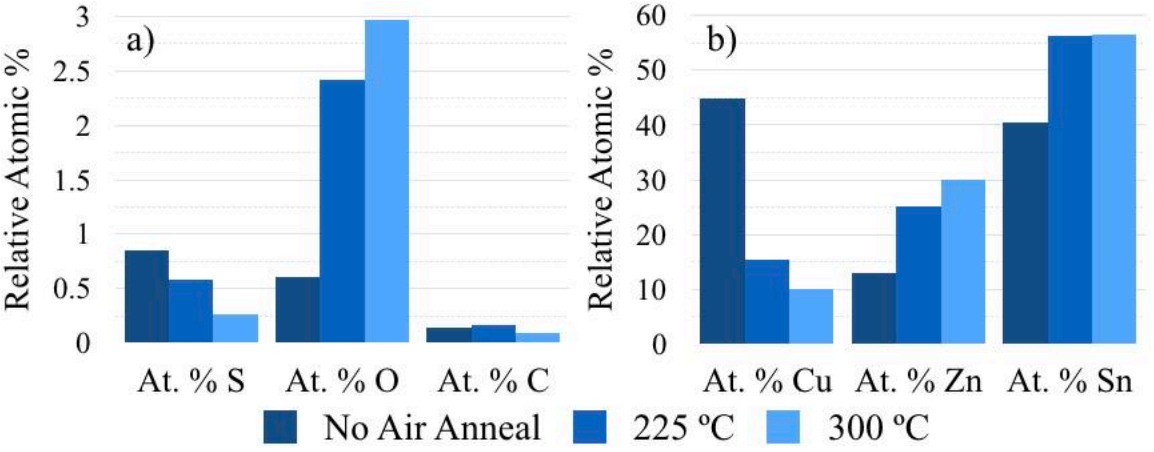

Figure 19: Shows relative atomic composition of different elements as calculate from XPS spectra of samples before air annealing, then after air annealing at 225 and 300 ºC. a) Compares relative sulfur, oxygen, and carbon content at the particle surface. b) Compares Cu, Zn, and Sn content at the particle surface.

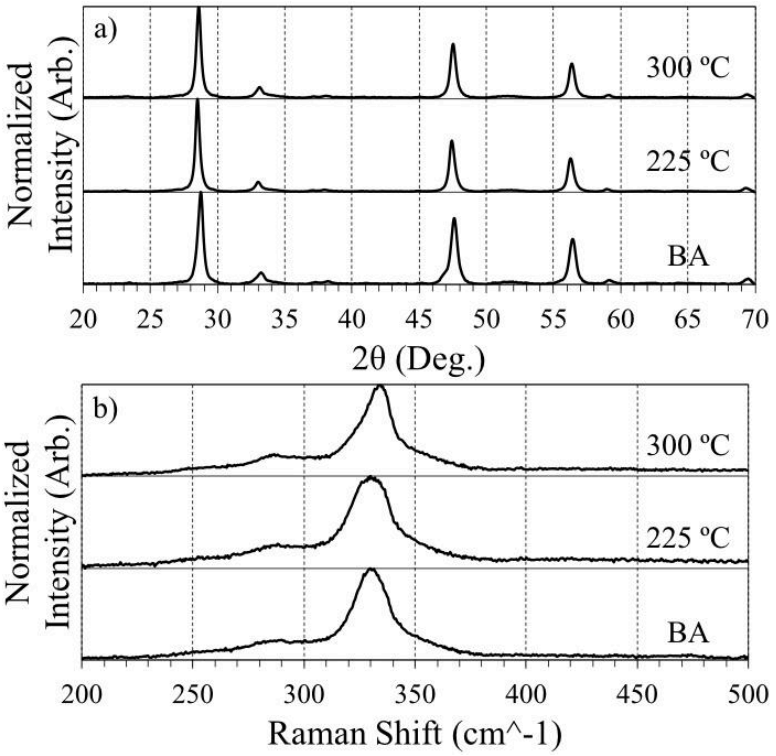

Figure 19: Shows XRD (a) and Raman (b) characterization of nanoparticle samples as-produced (BA), then after annealing at 225 ºC and 300 ºC.

tin and zinc, and consequently more copper-poor, compared to the surface of particles that have not been air-annealed. SEM/EDS measurements indicate that the loss of copper is restricted to the particle surface; the composition of the bulk powder remains the same within uncertainty of the measurement.

Other groups have observed similar behavior in the CZTS layer after annealing CZTS-based PV devices in air.[11-14] Using Auger Nanoprobe Spectroscopy, Sardashti *et al*. characterized the formation of these copper-depleted, SnO_x-enriched surfaces in the absorber layer after air-annealing a CZTSSe-based PV.[11] The absence of copper at the particle surfaces may be attributed to the formation of $CuSO_4$, which is volatile at temperatures much lower than the air annealing temperature.[15] Copper sulfate has a relatively low heat of formation,[16] and the corresponding zinc and tin sulfates are much less likely to form — the respective heats of formation are roughly 5 and 10 times greater in magnitude than that for copper sulfate.[16,17]

These air-annealed CZTS particle samples are then coated, pressed, and annealed according to the exact same procedure used for the non-air-annealed particles as described in Section 4.5. The as-produced powder-derived samples appear to be morphologically similar to that seen in Fig. 16 — large CZTS grains are formed sparsely and on the surface of a uniform-but-porous smaller grain layer. The resulting films derived from the air-annealed powder are starkly contrasting, however.

The film, as determined from SEM, consists of uniform, large-grain CZTS (Fig. 20e-g). The average grain size for the sample derived from powder annealed in air at 225 ºC is 1.8 ± 0.5 µm. The powder annealed at 225 ºC consistently gives the most uniform

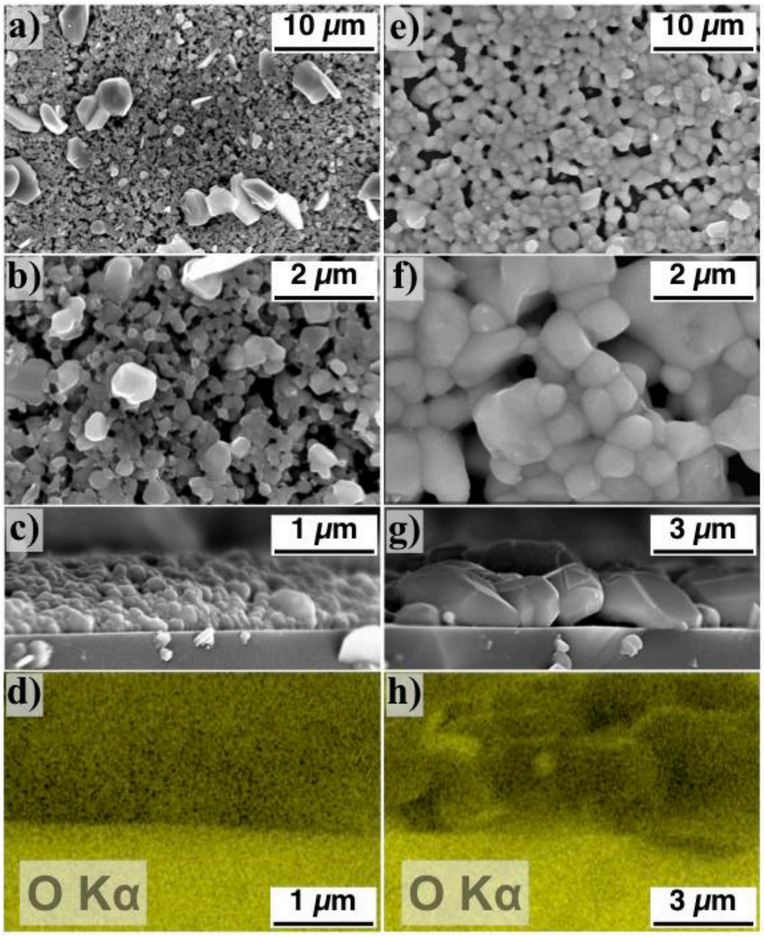

Figure 20: Top-down and cross-section SEM images of films derived from as-produced CZTS nanoparticles (a-c) and nanoparticles annealed in air at 225 ºC (e-g). (d) and (f) are EDS maps of oxygen content in images (c) and (g) respectively.

and least porous film, though similarly uniform grain growth is observed for all films derived from powder annealed in air between 200 and 300 ºC. The air-annealed sample exhibits uniform large grain morphology on a large scale (Fig. 20e) relative to the non-air annealed counterpart (Fig. 20a).

A further notable result is observed in Fig. 20g — the large grains of CZTS span the thickness of the film (~2 μm) with no carbon-rich fine-grain layer between the film and the substrate. Typically in related work, CZTS nanoparticles are synthesized via a hot-injection method, and consequently are covered at the surface with organic ligands. These ligands result in the aforementioned carbon-rich fine-grain layer sandwiched between the bulk of the film and the substrate.[10,18-22] Huang *et al.* have demonstrated a method to eliminate this fine-grain layer by using ligand-free CZTS nanoparticles synthesized by hot-injection in a formamide solvent system and maximizing the packing density of the nanoparticle coating before annealing.[23] The samples shown in Fig. 20 imply that a similar result can be achieved by an alternative mean — by starting with ligand-free CZTS nanoparticles and performing a 30-minute anneal in atmosphere at moderate temperature.

Intuitively thinking, the introduction of oxygen into the material may adversely affect charge transport in the film by introducing poorly conducting phases into the structure. In Fig. 20h, the oxygen in the system appears to aggregate at the surfaces of the grains and not in the bulk. Further characterization is necessary to investigate the role of such oxide segregations on the electronic properties of the films. Such a study goes beyond the scope of our work. Nevertheless, the conclusion from a recent study by Sardashti *et al.* is that the presence of tin-oxide phases and copper depletion at the surface of the grains in a CZTS thin film act as a passivating layer, inhibiting charge recombination at grain boundaries.[11] Air-annealing CZTS/CZTSSe-based PVs after production is now commonly applied to enhance device efficiency by this passivation mechanism.[12]

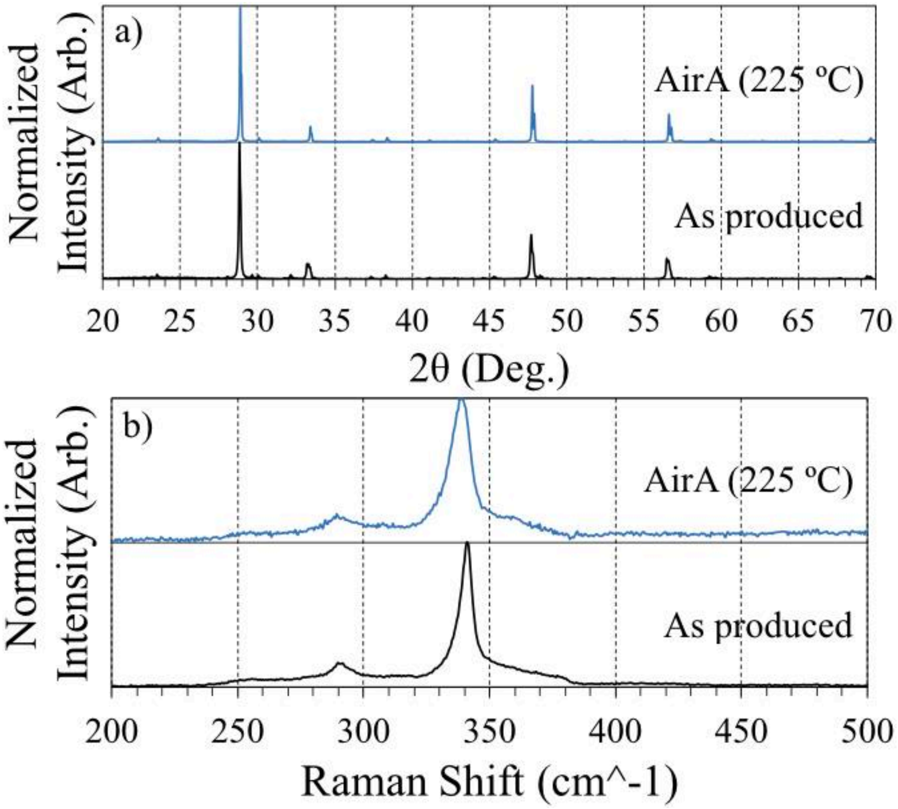

Figure 21: XRD patterns (a) and Raman spectra (b) comparing air-annealed powder-derived CZTS thin films to as-produced powder-derived films. Each spectrum is normalized to itself.

Structurally, both of the annealed films in Fig. 20 appear to be phase-pure CZTS (Fig. 21). Comparisons in diffraction and Raman spectra between the air-annealed powder-derived sample and the as-produced powder-derived sample show minimal bulk-phase variability. In Fig. 21a, the diffraction peaks between the two samples align, with the 112 peak strongest at 28.4 ºC aligning well with CZTS standards.[8] The difference is that the air-annealed sample exhibits sharper peaks, to be expected after observing the morphology in SEM. Scherrer peak analysis of the respective 112 peaks in Fig. 21a yields an approximate average crystallite size of 130 nm for the “AirA (225 ºC)” sample and 77 nm for the “As Produced” sample. In Raman (Fig. 21b), the spectra are effectively identical, with both samples exhibiting CZTS peaks at ~336 and 286 cm^{-1}.[8] It is crucial to apply both Raman and XRD to determine the phase of a CZTS film. Diffraction alone is insufficient due to the near perfect overlap of kesterite CZTS with its potential segregate-phases ZnS and Cu_2SnS_3.[8] We have observed signatures of these segregating phases independent of the primary CZTS resonance at 336 cm^{-1} in different samples not shown here.

It must also be noted that the apparent bulk-phase purity is not necessarily indicative of an entirely phase-pure sample. A recent study by Alvarez *et al.* used Raman microprobe spectroscopy to identify structural and compositional inhomogeneity that exists from grain-to-grain in a CZTS film that appears structurally phase pure and compositionally near-stoichiometric using the conventional characterization strategy.[24] The samples examined in this study were synthesized by sulfurizing a stack of sputtered Cu, Zn, and Sn metal-layers using the same technique detailed in Section 4.5, but for an eight-hour duration rather than the one-hour used here for nanoparticle sintering.

In the present study, after quantifying the composition of different spots in the two films obtained without and with the nanoparticle air-annealing step (Fig. 22a and 22b respectively), it is apparent that the same localized compositional variability found by Alvarez *et al.* exists in the films analyzed in this study.[24] The table beneath Fig. 22a clearly shows a variability in the metal content between the small grains and the segregated large grains. The large grains each have a relatively higher tin and copper content, as evidenced by the decrease in the Zn/Sn ratio from spots 1 and 2 to spots 3, 4, and 5. The copper content is highly variable, with a large increase between the spots 1, 2,

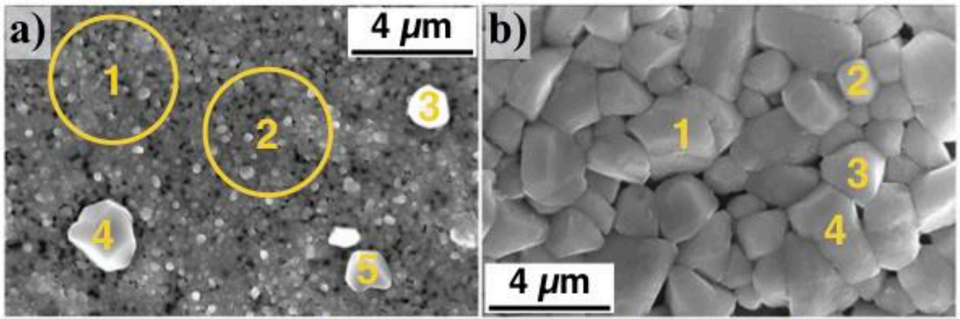

(Fig. a)	Zn/Sn	Cu/(Zn+Sn)	(Fig. b)	Zn/Sn	Cu/(Zn+Sn)
Spot 1	0.92	1.41	Spot 1	0.72	1.51
Spot 2	0.93	1.37	Spot 2	0.76	1.16
Spot 3	0.84	1.80	Spot 3	0.68	1.74
Spot 4	0.86	1.62	Spot 4	0.67	1.43
Spot 5	0.85	1.67	Whole Field	0.72	1.39

Figure 22: Top-down SEM images of as-produced CZTS powder-derived film (a) and air-annealed CZTS powder-derived film (b) with different spots showing locations of EDS elemental quantification (in atomic %). Each number corresponds to the underlying grain and the respective spot in the table below, where Cu, Zn, and Sn are quantified with respect to each other. In the table under (b), "Whole Field" refers to elemental quantification of the entire image.

and 3, 4, and 5. In the air-annealed nanoparticle-derived film (Fig. 22b), there is still variability from grain-to-grain as well. The small grain in spot 2 appears to be more tin- and copper-poor than the others surveyed, matching the trend between the large and small grains in Fig. 22a. However, the sample in Fig. 22b shows a consistently higher tin content relative to zinc.

In addition to these observations, we have compared the average (measured at low magnification to include a large number of grains) amount of tin in several sulfurized CZTS thin films (Fig. 23). We have found consistently higher tin content in films produced using the air-annealed powder.

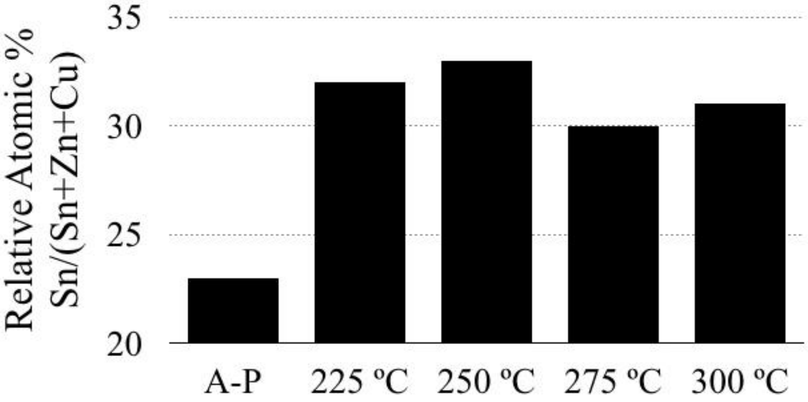

Figure 23: Comparison of tin content relative to all metals in annealed CZTS thin films. The bars represent as-produced (A-P), and the different temperature air-annealed CZTS nanoparticle-derived films.

To summarize, the elemental analysis data shown in Figs. 22 and 23 give some insight into the grain growth mechanics for the CZTS material system and suggest that tin plays a crucial role in the kinetics of grain growth in CZTS thin films. This information, after comparing the morphologies and compositions between large and small grains (Fig. 22) and after comparing the composition of films realized from particles with and without an oxide shell, supports the conclusion that the amorphous oxide layer formed during the air-annealing process (Fig. 17) acts as a diffusion barrier that helps in retaining volatile phases during the high-temperature sulfurization step.

4.7: Na_2S-Induced Phase Activity

Current efforts to improve the efficiency of CZTS-based devices are mirroring the development of the CIGS system, which is structurally similar to CZTS. sodium doping has been shown to enhance device performance and thin film properties in both the CIGS and CZTS systems.[2,25-29] By comparing the growth of CZTS crystal grains on substrates with and without sodium, enhanced grain growth was concluded to be an effect of sodium and other alkali diffusion from the substrate into the film material.[2] These devices, in turn, also exhibited better performance than the devices without alkali in-diffusion due to enhanced minority carrier mobility.

Organic ligands have also been proposed as being beneficial in promoting grain growth in CZTS/CZTSSe nanoparticle systems. Martin *et al*. compared the effect that two different nanoparticle-capping-ligands, derived from oleylamine (OLA) and dodecylamine respectively in a hot-injection process, had on the crystallinity of the annealed CZTSSe film.[18] The conclusion was that the longer ligands from the OLA yielded vastly superior crystallinity and uniformity after annealing. Huang *et al*. have produced a similar study in pure CZTS, comparing the crystallinity of films derived from OLA-synthesized CZTS nanoparticles and formamide-synthesized CZTS nanoparticles.[23] However, with carbon introduced to the system, these same groups report highly crystalline thin films in the case of the higher-carbon content ligands, but with a carbon-rich fine-grain layer sandwiched between the substrate and the CZTS or CZTSSe film.

There is little precedent for the synthesis of surface-ligand-free CZTS particles that can be sintered successfully into uniform large-grain thin films. Huang *et al*. have reported a ligand-free application of the hot-injection synthesis method by substituting a formamide solvent system as the reaction media.[23] Huang *et al*. report further the successful sintering of these ligand-free films into a highly crystalline and highly uniform thin film by mechanically compacting with a "reasonably soft metal and silicone",[23] maximizing the packing density of the nanoparticle coatings. Alternatively, in our previous work we have shown that a thin amorphous oxide layer grown on the surface of surface-ligand-free CZTS particles facilitates the formation of uniform large-grain CZTS films.[30] Our recent focus has concerned identifying a facile method by which to facilitate grain growth in these coatings, and we take inspiration from the work from Tiong *et al.*, in which the authors demonstrated controllable grain growth in surface-ligand-free CZTS nanoparticle coatings by dipping the coatings in a sodium halide solution prior to annealing.[31]

In this section, I present a novel method of controlling sodium incorporation into CZTS thin films by a facile sodium disulfide (Na_2S) dipping technique. After production, CZTS nanoparticles are coated onto an inert quartz glass substrate. The coating is then submerged in a Na_2S:MeOH solution for five minutes and then dried overnight at 60 ºC to evaporate the solvent and leave a Na_2S residue coating the film. During annealing, the film exhibits grain growth that is indicative of sodium incorporation. Further, by varying the concentration of the dipping solution, different film morphologies, structural homogeneity, and cation ordering are obtained after annealing, indicating that varied amounts of sodium are incorporated.

For the sodium disulfide-dipping process, varied amounts of Na_2S are dissolved in methanol. In this manuscript, solution concentrations of 0, 0.01, 0.05, 0.1, and 0.5 M were used. The drop-cast nanoparticle coatings are then submerged in the solution for 5 minutes, then placed in a convection oven held at 60 ºC to dry overnight. The dipped coatings are then sealed inside quartz glass ampoules with some elemental sulfur and annealed according to the procedure outlined in Section 4.5.

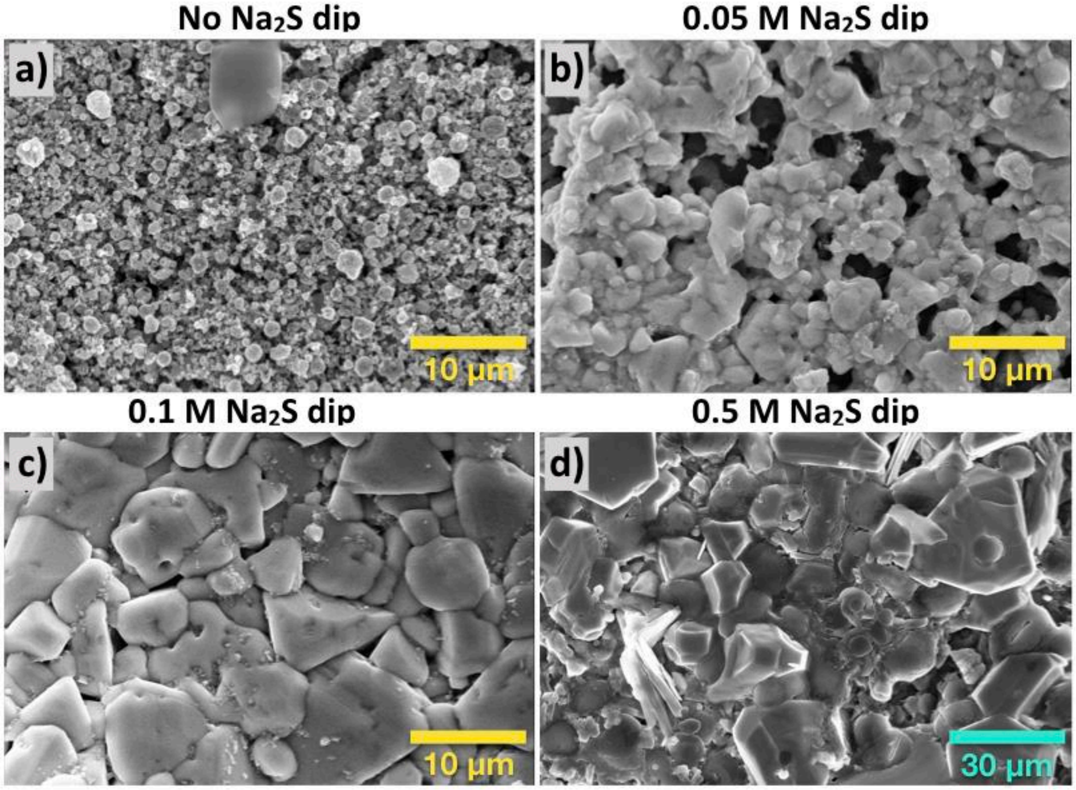

Figure 24: SEM images from samples annealed after dipping in Na_2S solutions of 0 (a), 0.05 (b), 0.1 (c), and 0.5 M (d). Scale bars in a-c are 10 μm, in d it is 30 μm.

With the four different Na_2S dipping concentrations — 0.0 M, 0.05 M, 0.1 M, and 0.5 M — we demonstrate a wide range of quality in the annealed CZTS films. In Fig. 24, each SEM image corresponds with a different dipping concentration. With no Na_2S (Fig. 24a), we see very little change in the morphology of the film from pre- to post-annealing. The grains remain small and the film is quite porous. With 0.05 M Na_2S (Fig. 24b), the film is still quite porous, but there is some crystal grain growth. The grain growth appears somewhat uneven, with some larger grains and some smaller grains, and there are some areas where material accumulates while in other areas there are large voids. With 0.1 M Na_2S (Fig. 24c), the film has what we consider to be near-optimal morphology (similar to the morphology exhibited in Figs. 20f and 22b). The crystal grains are uniformly large in size, and there are few pores or voids in the film. There are small particulates on the surface, which may be attributable to segregated phases like copper sulfide or tin sulfide or to residue from the Na_2S dopant. With 0.5 M Na_2S (Fig. 24d), the crystal grains have grown excessively (note the different scale bar from the other images). Further, the shape and texture of the grains suggests significant structural inhomogeneity within this film.

Raman spectroscopy demonstrates the structural changes in each of these samples (Fig. 25). These spectra were collected at low magnification (10x) to ensure the resulting spectra represents a large area survey of the film, although we know in smaller areas there will be significant phase inhomogeneity.[24,30] Fig. 25a shows spectra collected using a 532 nm Raman probe laser, and Fig. 25b shows spectra from the same samples collected using a 785 nm Raman probe laser. In each of the first three dipping conditions (0, 0.05, and 0.1 M Na_2S), CZTS appears to be the dominant phase present after annealing. With increasing Na_2S-dip concentration, though, the CZTS phase develops

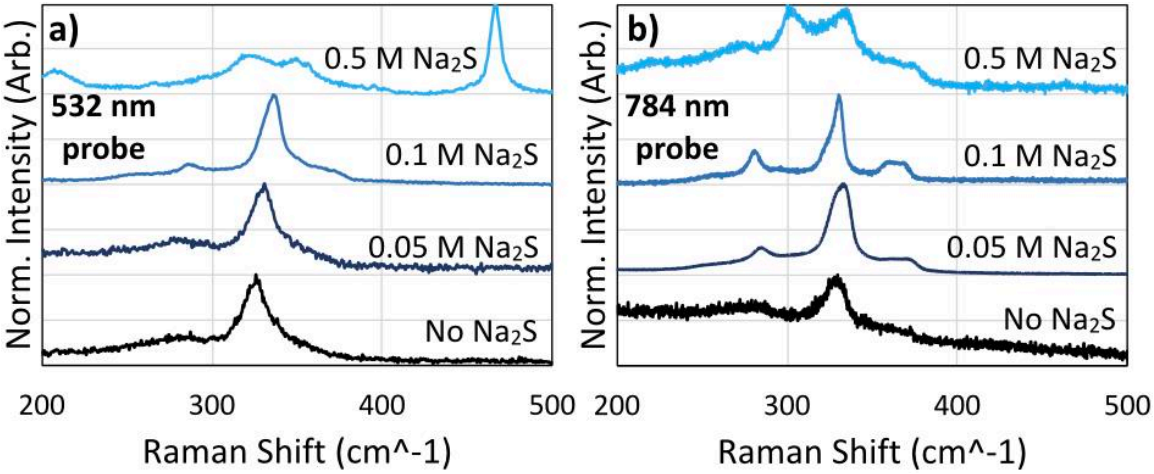

Figure 25: Raman spectra from samples annealed after dipping in Na_2S solutions of 0, 0.05, 0.1, and 0.5 M. a) Shows Raman spectra collected using 532 nm probe laser, b) shows spectra collected using 785 nm probe.

longer-range order, indicated by the slight blue-shift and increase in sharpness of the peaks in the spectra. The spectra collected using the 785 nm Raman probe contrast with those collected using the 532 nm Raman probe, in that there is less signal from more disordered CZTS (0 M Na_2S sample) — the spectra are normalized to themselves, but the increased noise and reduced distinction from the background are show this. The features to the right of the dominant CZTS peak in the 0.1 M Na_2S sample in the 785 nm probe spectrum are indicative of cation-ordering within the CZTS phase and can only be adequately characterized using a 785 nm Raman probe. There will be extensive discussion of these features in the next chapter.

Similar to that which was suggested by the morphology of the 0.5 M Na_2S-dipped sample (Fig. 24), the structural composition of the sample is segregated phases from CZTS, like SnS_2, Cu_2SnS_3, and Cu_2S. ZnS is difficult to characterize using Raman spectroscopy under the same acquisition parameters needed to characterize these other sulfide phases without thermal damage. That Cu_2S (~474 cm^{-1}) can be seen in the 532 nm Raman probe spectrum and not in the 785 nm Raman probe spectrum (spectra acquired from different spots on the same sample) suggests the massive degree of inhomogeneity in this film, since the spectrum is acquired over a large area.

Indeed, EDS maps collected from this 0.5 M Na_2S-dipped sample show clear segregation of the different cation elements in the film (Fig. 26). In these maps, it appears that copper and tin tend to segregate to similar areas, and zinc tends to segregate separately. Given that ZnS is known to be immiscible with Cu_2S and SnS_2, while the latter two are miscible with each other,[32] this observation is not unexpected. This clear

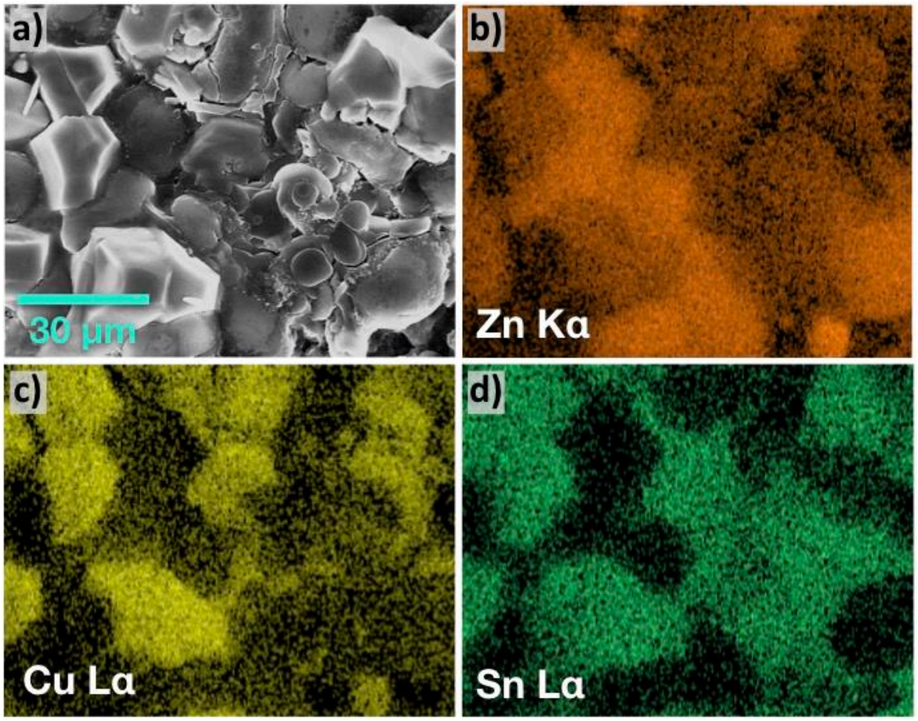

Figure 26: a) SEM image of sample annealed after dipping in 0.5 M Na_2S solution and corresponding EDS maps indicating the presence of Zn (b), Cu (c), and Sn (d) atoms.

segregation at a large scale indicates that the excess presence of sodium catalyzes a high level of solid-state cation diffusion during the annealing process. This has been hypothesized to be the reason that the presence of sodium enhances grain growth in CZTS films during annealing.[2,33] In contrast, EDS maps collected from the 0.1 M Na_2S-dipped sample shows no obvious elemental cation segregation (Fig. 27), suggesting that there is an upper limit to the concentration of sodium that can be incorporated as a dopant in CZTS before its presence induces material degradation and phase segregation, a conclusion shared by Gershon *et al.*[33]

In sum, we have demonstrated two methods — partial particle oxidation and Na_2S incorporation — of generating what we may call “optimal” CZTS thin films by annealing

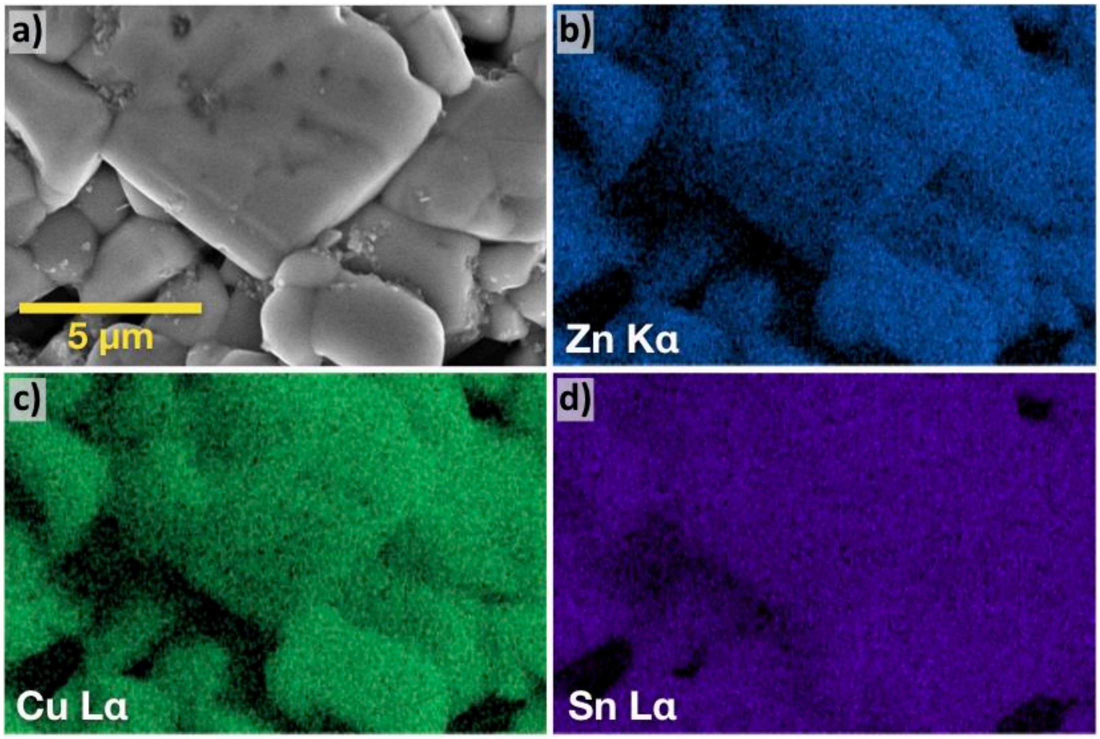

Figure 27: a) SEM image of sample annealed after dipping in 0.1 M Na_2S solution and corresponding EDS maps indicating the presence of Zn (b), Cu (c), and Sn (d) atoms.

coatings of CZTS nanoparticles. While we can argue for different explanations of why these techniques yield positive results, questions regarding material dynamics during the ever-crucial annealing process remain. *In situ* characterization of samples during this process is essential to gaining a better understanding of this material.

4.8: References

(1) Khare, A.; Willis, A. W.; Ammerman, L. M.; Norris, D. J.; Aydil, E. S. Size Control and Quantum Confinement in Cu2ZnSnS4 Nanocrystals. *Chemical Communications*, **2011**, *47*(42), 11721-11723.

(2) Johnson, M.; Baryshev, S. V.; Thimsen, E.; Manno, M.; Zhang, X.; Veryovkin, I. V.; Leighton, C.; Aydil, E. S. Alkali-Metal-Enhanced Grain Growth in Cu2ZnSnS4 Thin FIlms. *Energy & Environmental Science*, **2014**, *7*(6), 1931-1938.

(3) Exarhos, S.; Bozhilov, K. N.; Mangolini, L. Spray Pyrolysis of CZTS Nanoplatelets. *Chemical Communications*, **2014**, *50*(77), 11366-11369.

(4) Huse, N. P.; Dive, A. S.; Mahajan, S. V.; Sharma, R. Facile, One Step Synthesis of Non-Toxic Kesterite Cu2ZnSnS4 Nanoflakes Thin Film by Chemical Bath Deposition for Solar Cell Application. *Journal of Materials Science: Materials in Electronics*, **2018**, 1-10.

(5) Courel, M.; Andrade-Arvizu, J. A.; Guillén-Cervantes, A.; Nicolás-Marín, M. M.; Pulgarín-Agudelo, F. A.; Vigil-Galán, O. Optimization of Physical Properties of Spray-Deposited Cu2ZnSnS4 Thin Films for Solar Cell Applications. *Materials & Design*, **2017**, *114*, 515-520.

(6) Deepa, K. G.; Chandrabose, G.; Jampana, N. Tailoring the Properties of Cu2ZnSnS4 Thin Films Grown by Ultrasonic Spray Pyrolysis. *Journal of Analytical and Applied Pyrolysis*, **2016**, *120*, 356-360.

(7) Mitzi, D. B.; Gunawan, O.; Todorov, T. K.; Wang, K.; Guha, S. The Path Towards a High-Performance Solution-Processed Kesterite Solar Cell. *Special Issue: Thin Film and Nanostructured Solar Cells*, **2011**, *95*(6), 1421-1436.

(8) Cheng, A.-J.; Manno, M.; Khare, A.; Leighton, C.; Campbell, S. A.; Aydil, E. S. Imaging and Phase Identification of Cu2ZnSnS4 Thin Films Using Confocal Raman Spectroscopy. *Journal of Vacuum Science & Technology A*, **2011**, *29*(5), 051203.

(9) Rau, H.; Kutty, T. R. N.; Guedes de Carvalho, J. R. F. High Temperature Saturated Vapour Pressure of Sulphur and the Estimation of its Critical Quantities. *The Journal of Chemical Thermodynamics*, **1973**, *5*(2), 291-302.

(10) Chernomordik, B. D.; Béland, A. E.; Deng, D. D.; Francis, L. F.; Aydil, E. S. Microstructure Evolution and Crystal Growth in Cu2ZnSnS4 Thin Films Formed by Annealing Colloidal Nanocrystal Coatings. *Chemistry of Materials*, **2014**, *26*(10), 3191-3201.

(11) Sardashti, K.; Haight, R.; Gokmen, T.; Wang, W.; Chang, L.-Y.; Mitzi, D. B.; Kummel, A. C. Impact of Nanoscale Elemental Distribution in High-Performance Kesterite Solar Cells. *Advanced Energy Materials*, **2015**, *5*(10), 1402180.

(12) Haight, R.; Shao, X.; Wang, W.; Mitzi, D. B. Electronic and Elemental Properties of the Cu2ZnSn(S,Se)4 Surface and Grain Boundaries. *Applied Physics Letters*, **2014**, *104*(3), 033902.

(13) Chen, S.; Gong, X. G.; Walsh, A.; Wei, S.-H. Crystal and Electronic Band Structure of Cu2ZnSnX4 (X=S and Se) Photovoltaic Absorbers: First-Principles Insights. *Applied Physics Letters*, **2009**, *94*(4), 041903-041906.

(14) Ennaoui, A.; Lux-Steiner, M.; Weber, A.; Abou-Ras, D.; Kötschau, I.; Schock, H.-W.; Schurr, R.; Hölzing, A.; Jost, S.; Hock, R.; Voß, T.; Schulze, J.; Kirbs, A. Cu2ZnSnS4 Thin Film Solar Cells from Electroplated Precursors: Novel Low-Cost Perspective. *Thin Solid Films*, **2009**, *517*(7), 2511-2514.

(15) Liley, P. E.; Thomson, G. H.; Friend, D. G.; Daubert, T. E.; Buck, E. *Physical and Chemical Data, Section 2*. The McGraw-Hill Companies, Inc., **1999**.

(16) Logan, T. S. Textbook Errors: Guest Column XVI: The Vapor Pressure of Hydrated Cupric Sulfate. *Journal of Chemical Education*, **1958**, *35*(3), 148.

(17) Gamsjäger, H.; Gajda, T.; Sangster, J.; Saxena, S. K.; Voigt, W. Chemical Thermodynamics of Tin, *Organization for Economic Co-Operation and Development*, **2012**.

(18) Martin, T. R.; Katahara, J. K.; Bucherl, C. N.; Krueger, B. W.; Hillhouse, H. W.; Luscombe, C. K. Nanoparticle Ligands and Pyrolyzed Graphitic Carbon in CZTSSe Photovoltaic Devices. *Chemistry of Materials*, **2016**, *28*(1), 135-145.

(19) Liu, X.; Huang, J.; Zhou, F.; Liu, F.; Sun, K.; Yan, C.; Stride, J. A.; Hao, X. Understanding the Key Factors of Enhancing Phase and Compositional Controllability for 6% Efficient Pure-Sulfide Cu2ZnSnS4 Solar Cells Prepared from Quaternary Wurtzite Nanocrystals. *Chemistry of Materials*, **2016**, *28*(11), 3649-3658.

(20) Wang, W.; Shen, H.; Wong, L. H.; Su, Z.; Yao, H.; Li, Y. A 4.92% Efficiency Cu2ZnSnS4 Solar Cell from Nanoparticle Ink and Molecular Solution. *RSC Advances*, **2016**, *6*(59), 54049-54053.

(21) Bree, G.; Coughlan, C.; Geaney, H.; Ryan, K. M. An Investigation into the Selenization Mechanisms of Wurtzite CZTS Nanorods. *ACS Applied Materials & Interfaces*, **2018**, *10*(8), 7117-7125.

(22) Clark, J. A.; Uhl, A. R.; Martin, T. R.; Hillhouse, H. W. Evolution of Morphology and Composition during Annealing and Selenization in Solution-Processed Cu2ZnSn(S,Se)4. *Chemistry of Materials*, **2017**, *29*(21), 9328-9339.

(23) Huang, T. J.; Yin, X.; Tang, C.; Qi, G.; Gong, H. A Low-Cost, Ligand Exchange-Free Strategy to Synthesize Large-Grained Cu2ZnSnS4 Thin-Films Without a Fine-Grain Underlayer from Nanocrystals. *Journal of Materials Chemistry A*, **2015**, *3*(34), 17788-17796.

(24) Alvarez Barragan, A.; Malekpour, H.; Exarhos, S.; Balandin, A. A.; Mangolini, L. Grain-to-Grain Compositional Variations and Phase Segregation in Copper-Zinc-Tin-Sulfide Films. *ACS Applied Materials & Interfaces*, **2016**, *8*(35), 22971-22976.

(25) Nakada, T.; Iga, D.; Ohbo, H.; Kunioka, A. Effects of Sodium on Cu(In,Ga)Se2-Based Thin Films and Solar Cells. *Japanese Journal of Applied Physics*, **1997**, *36*(1), 2.

(26) Rockett, A. The Effect of Na in Polycrystalline and Epitaxial Single-Crystal CuIn1-xGaxSe2. *Thin Solid Films*, **2004**, *480-481*, 2-7.

(27) Prabhakar, T.; Jampana, N. Effect of Sodium Diffusion on the Structural and Electrical Properties of Cu2ZnSnS4 Thin Films. *Solar Energy Materials and Solar Cells*, **2011**, *95*(3), 1001-1004.

(28) Hlaing Oo, W. M.; Johnson, J. L.; Bhatia, A.; Lund, E. A.; Nowell, M. M.; Scarpulla, M. A. Grain Size and Texture of Cu2ZnSnS4 Thin Films Synthesized by Cosputtering Binary Sulfides and Annealing: Effects of Processing Conditions and Sodium. *Journal of Electronic Materials*, **2011**, *40*(11), 2214-2221.

(29) Li, J. V.; Kuciauskas, D.; Young, M. R.; Repins, I. L. Effects of Sodium Incorporation in Co-Evaporated Cu2ZnSnSe4 Thin-Film Solar Cells. *Applied Physics Letters*, **2013**, *102*(16), 163905.

(30) Exarhos, S.; Palmes, E.; Xu, R.; Mangolini, L. Oxide-Induced Grain Growth in CZTS Nanoparticle Coatings. *RSC Advances*, **2017**, *7*(41), 25575-25581.

(31) Tiong, V. T.; Hreid, T.; Zhang, S.; Bell, J.; Wang, H. Morphology Evolution and Stability of Cu2ZnSnS4 Nanocrystals in Sodium Halides Salt Solution. *Thin Solid Films*, **2016**, *615*, 305-310.

(32) Just, J.; Sutter-Fella, C. M.; Lützenkirchen-Hecht, D.; Frahm, R.; Schorr, S.; Unold, T. Secondary Phases and Their Influence on the Composition of the Kesterite Phase in CZTS and CZTSe Thin Films. *Physical Chemistry Chemical Physics*, **2016**, *18*, 15988-15994.

(33) Gershon, T.; Shin, B.; Bojarczuk, N.; Hopstaken, M.; Mitzi, D. B.; Guha, S. The Role of Sodium as a Surfactand and Suppressor of Non-Radiative Recombination at Internal Surfaces in Cu2ZnSnS4. *Advanced Energy Materials*, **2015**, *5*(2), 1400849.

Chapter 5: *In Situ* Raman Characterization of CZTS Nanoparticle Sintering

5.1: *In Situ* CZTS Characterization

In this chapter, I present a system with which to conduct *in situ* Raman characterization of a CZTS nanoparticle coating during high temperature annealing in a closed sulfur atmosphere. This system allows for studying the material dynamics of the material in an effective facsimile of what I have determined to be the optimal annealing conditions for these films. I highlight two experiment designs demonstrating the usefulness of this system. First, I monitor the shift in Raman frequencies with increasing temperature in SnS_2, Cu_2S, and CZTS nanoparticle coatings. Raman frequencies red-shift in linear proportionality with temperature, so by comparing peak shifts with this proportionality I ascertain information about the development of material structure *in situ*. Second, I monitor the development of cation-site ordering in CZTS films as they are cooled past a critical order/disorder transition temperature at different rates. Ordering parameters are calculated and compared to *ex situ* values to demonstrate the power of my *in situ* technique. Data collected from these and similar experiments can be used to identify transition points in inter- and intra-structural dynamics during thermal processing, providing a basis for more finely-targeted future studies.

An extensive body of literature exists that details the gradual optimization of the sulfur-annealing process for high-quality CZTS thin films. It is known that for a high temperature of >500 ºC must be used,[1-3] that the inclusion of a diffusive alkali source is needed,[4-7] that a low-pressure sulfur atmosphere is needed,[8-10] and that the sample must be cooled very slowly.[11-15] Most of these details have been developed through a combination of theoretical predictions and experimental observations. However, applications of *in situ* characterization techniques have yielded data that allows not only for more expedient optimization of annealing parameters, but also for a deeper understanding of the material dynamics at high temperature.[2,3,16]

At the 600 ºC annealing temperature used in this and other works, kesterite-CZTS should be unstable in off-stoichiometric compositions and should decompose into binary and ternary sulfide phases.[10] Additionally, the presence of any secondary phases — noted as prevalent by Alvarez *et al.*[17] — will influence the composition of kesterite-CZTS in single-grain domains.[18,19] Huang and Persson, however, note that theoretically the formation of certain stoichiometry-dependent intrinsic point defects stabilizes the crystal structure,[20] a result confirmed experimentally by Valle Rios *et al.*[18] The copper-poor and zinc-rich stoichiometry is used to promote the formation of (Zn_{Cu} + V_{Cu}) and (Zn_{Cu} + Cu_{Zn}) defect complexes relative to other defect structures.[18,20] Further, these complexes form in conjugation with each other to maintain the electron structure in kesterite, which helps explain why the band gap of this off-stoichiometric kesterite-CZTS is close to that for stoichiometric CZTS.[20] These defect complexes also promote charge transport in the bulk material, explaining why this off-stoichiometric condition is desirable for producing efficient PV devices.[20-23]

Comprehensive studies by Lund *et al.*[13] and Du *et al.*[1] indicate the importance of tin content as well. An excess of tin will result in a high degree of disorder in the kesterite lattice [13,19] while also contributing to a quenching effect of the PL signal.[1] Just *et al.* report empirically that the minority charge-carrier transport dynamics for an off-stoichiometric copper-poor, zinc-rich, tin-poor material should not hinder performance of CZTS-based PVs.[24]

Here, we show results from three series of *in situ* Raman experiments in order to characterize evolution in CZTS films during sulfur-annealing. First, by monitoring the CZTS Raman peak position during heating and comparing the behavior to that for simpler binary sulfide phases, we qualitatively observe the onset and development of large crystal domains at high temperatures. Second, we quantitatively characterize the development and reversibility of cation order/disorder via a low-temperature secondary sulfur-annealing process. Third, we study the effect of varying sodium content on the characteristics observed from the first two experiments.

5.2: A Novel System for *In Situ* Raman Characterization of Volatile Materials

In this work, a specialized furnace was constructed to facilitate Raman spectroscopy measurements of samples in sealed environments at high temperature, a schematic of which is shown in Fig. 1. The heating element in the furnace was designed to provide stable temperatures up to ~700 ºC and to accommodate the glass ampoules with outer diameter 0.64 cm (0.25 in.) and length 20 cm (8.0 in.) already used to anneal CZTS films in prior work,[3,5] and is thermally insulated via high-temperature cement bricks. A thermocouple is placed underneath the ampoule beneath the optical aperture to provide feedback to allow temperature control. The optical aperture is a 1.9 cm-diameter (0.75 in.) hole bored through the thermal insulation, and the sample can be manipulated inside the ampoule to sit directly beneath the aperture. The diameter of the aperture was

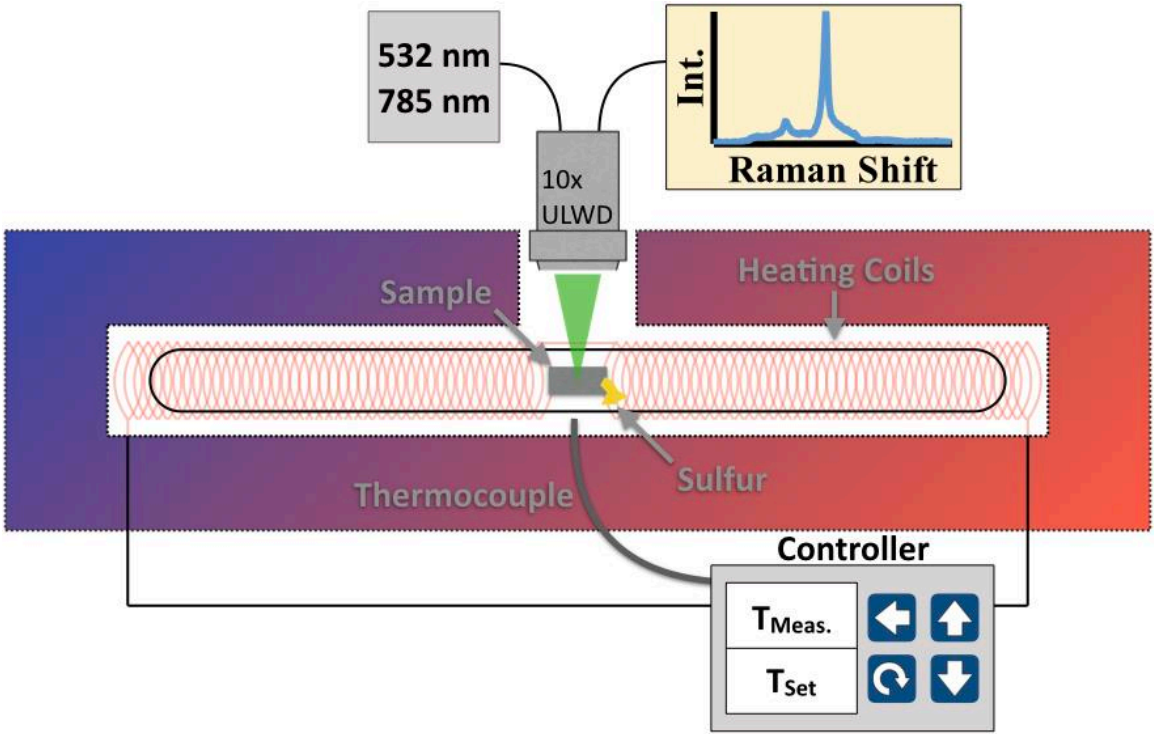

Figure 1: Schematic of in situ Raman system used to characterize CZTS films.

chosen such that an objective could be lowered to a distance sufficiently close to the sample in accordance with the focal length of the objective. For these experiments, a 10x Mitutoyo ML ultra-long working distance finite bright-field objective with a working distance of 51 mm was used. This allowed for Raman characterization at high temperatures while maintaining some separation between the objective and the heating element. Throughout the course of these experiments, no damage or variation in quality was observed in the objective. The objective was affixed to the confocal Raman spectroscopy system described in Section 4.4, in which 532 nm and 785 nm laser probes can be used.

Spectra were collected and analyzed with the LabSpec6 software package. With the 532 nm probe, a single spectrum was acquired and saved every 300 s using 60 mW laser power, 25% volume filter, 1,800 lines/mm grating, and a focused "spot" measuring ~5 µm wide by ~50 µm long — the curved ampoule glass acts like a cylindrical lens and distorts the laser beam into a line. With the 785 nm probe, a single spectrum was acquired and saved every 300 s using 120 mW laser power, 25% volume filter, 600 lines/mm grating, and a focused "spot" measuring ~5 µm wide by ~50 µm long. Due to the long acquisition time, spikes attributed to cosmic rays were prevalent in the spectra, and were computationally removed using the single spectrum de-spike method in LabSpec6. These parameters correspond with the standard annealing temperature profile used in this study: 20 ºC-600 ºC in 30 minutes, 600 ºC-600 ºC in 60 minutes, and 600 ºC-20 ºC in 193 min. (at a rate of 3 ºC/min.). There were different temperature profiles used for different experiments, and spectrum acquisition times were adjusted to accord with the desired temperature resolution for each experiment, which will be described in more detail further on. A representation of the data acquired from one *in situ* Raman experiment and the corresponding temperature profile for this experiment is shown in Fig. 2.

5.3: High Temperature Characterization

Sayed *et al*. (XRD), Wang *et al*. (Raman), and van Duren *et al*. (Raman) have studied the crystallization and decomposition of kesterite-CZTS at high temperature using *in situ* characterization on samples undergoing sulfur-free annealing.[2,3,16] In all three of these works, characterization of CZTS films at high temperature was performed in inert nitrogen at or near atmospheric pressure,[2,3,16] while under standard processing parameters, films are annealed in either a low pressure closed or flow system with some

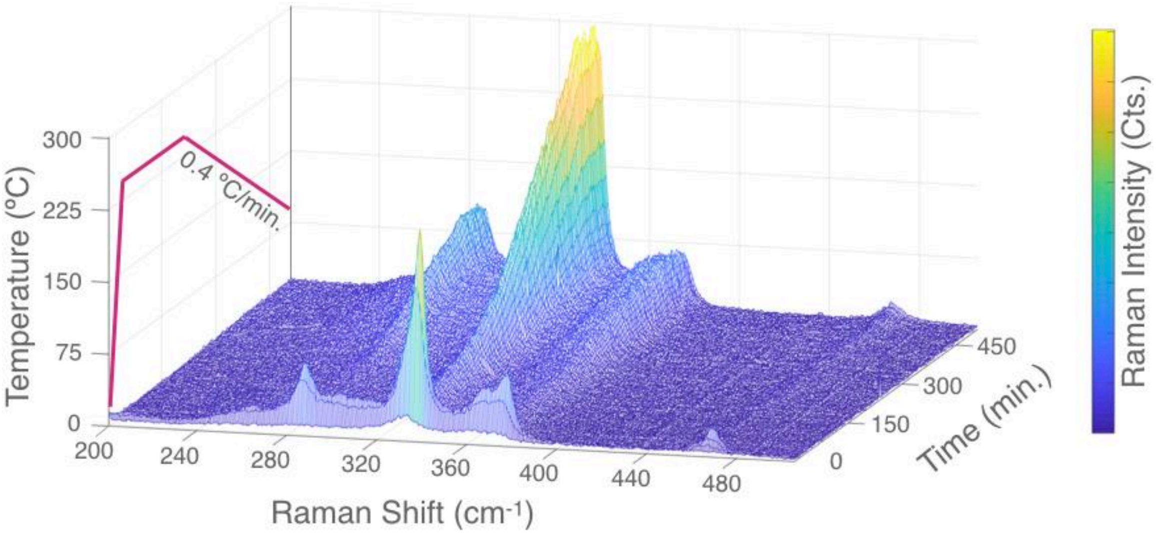

Figure 2: Sample data collected from in situ Raman system. Shows series of spectra collected during the course of one experiment with temperature ramp applied to the sample in.

elemental sulfur or H_2S gas. Nevertheless, these works help illuminate the importance of the established annealing parameters. Namely, CZTS crystallizes just below 400 ºC [2,3,16] and a tetragonal (kesterite/stannite) phase is thermodynamically favorable relative to hexagonal (wurtzite) phase above 526 ºC.[3]

In their *in situ* XRD characterization, Sayed *et al*. observe grain growth in CZTS nanoparticles only during the initial heating ramp, though there was no diffusive alkali source to promote large-scale grain growth, so their crystal grains grew only a small amount.[3] Similarly, both van Duren *et al*. and Wang *et al*. observe minimal grain growth beyond crystallization into kesterite-CZTS in their *in situ* monitoring of the crystallization of CZTS precursors.[2,16]

In Raman spectroscopy, crystal grain domain growth at the nanoscale can be characterized to some extent by comparing different vibrational modes in a material's characteristic spectrum.[25] This is often imprecise, though, because the extinction of phononic vibrations by grain boundaries cannot be differentiated from that by defects, stacking faults, or twinned crystals, not to mention by phase inhomogeneities.[25] In *in situ* Raman characterization of CZTS, though, temperatures at which crystal growth occurs (>350 ºC) [2,3] differs from that at which cation ordering in the kesterite phase occurs (<300 ºC),[12] suggesting that both crystal grain growth and cation ordering can be characterized.

In this section, we utilize *in situ* Raman spectroscopy to document the shift in Raman peak positions of SnS_2, Cu_2S, and CZTS nanoparticle coatings after dipping in 0.1 M Na_2S solution and during annealing in sulfur at high temperatures. We expect a linear red-shift in peak position with temperature similar to that observed van Duren *et al.* in the dominant Raman modes for each material.[16] Any deviations from this linear trend are indicative of phase transformation, large scale defect formation, or crystal grain growth.[25] Additionally, the comparison of CZTS to the simpler binary sulfide phases allows for the deconvolution of variables regarding the complex cation defect structures inherent to CZTS.

Each of the SnS_2, Cu_2S, and CZTS nanoparticle samples were prepared using the same aerosol spray pyrolysis apparatus described in Chapter 4, but with the requisite precursors and optimized furnace temperatures. The particles were coated, dipped, and annealed under the same parameters used to generate the CZTS film shown in Fig. 24c (Ch. 4) with Raman spectra acquired using the procedure in Section 4.4 and with the 532 nm laser probe. Peak positions are assigned to the dominant Raman modes for each phase

(315 cm^{-1} for SnS_2, 474 cm^{-1} for Cu_2S, 339 cm^{-1} for CZTS) and are accurate within a measurement uncertainty of 1.5 cm^{-1}.

In Fig. 3a-c, the peak positions for each of the three phases are plotted as a function of temperature during the initial heating ramp of the annealing process. In Fig. 6a, corresponding with the SnS_2 sample, the peak position red-shifts following the linear trend we expect with a slope of -0.016 cm^{-1}/ºC, similar to that observed by van Duren *et al.*[16] In Fig. 3b and c, corresponding with Cu_2S and CZTS respectively, the peak position follows the linear trend with the same slope, but the peak position deviates above some critical temperature — ~400 ºC for Cu_2S and ~500 ºC for CZTS. These values are not quantitatively valid due to the temperature resolution of these scans, but qualitatively effect is clear.

It must be noted that in both the Cu_2S and CZTS samples prior to any thermal

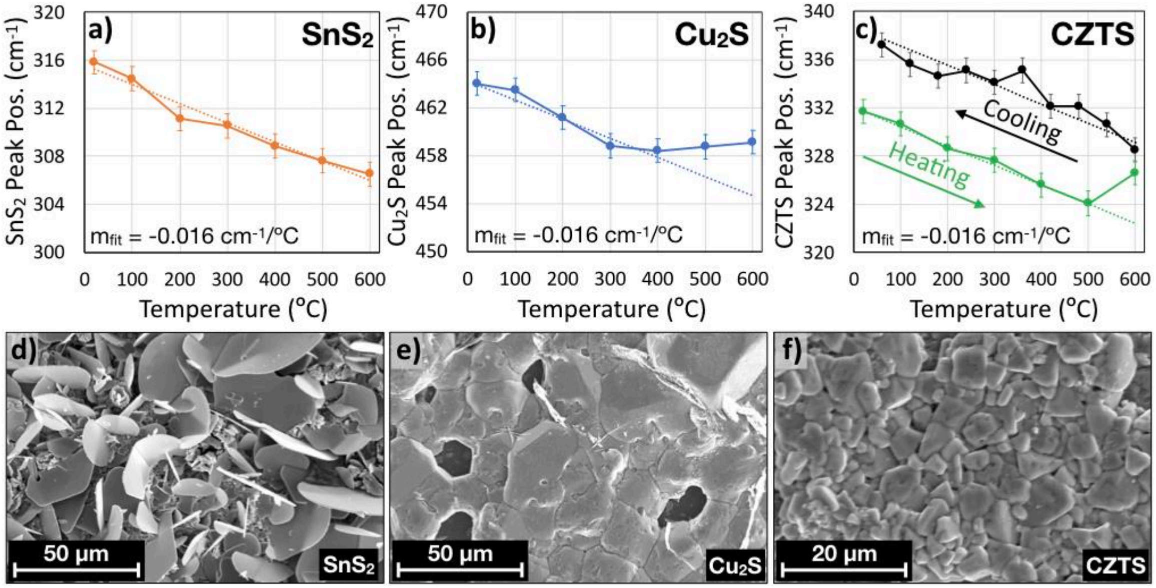

Figure 3: Shows trends in Raman peak position vs. temperature for SnS2 (a), Cu2S (b), and CZTS (c) films. Also shown are *ex situ* SEM images of annealed SnS_2 (d), Cu_2S (e), and CZTS (f) films after dipping in 0.1 M Na_2S.

treatment, the peak positions are red-shifted from standard values. We attribute this to the small crystal domain size in the initial nanoparticle coatings.[25] Fig. 3c also includes the CZTS peak position as a function of temperature during the cooling ramp. The peak position follows the same linear trend observed for all three samples during the heating ramp, but it is offset, and upon reaching room temperature, the position is in accordance with standards for long-range ordered CZTS crystals.

Comparing the post-anneal morphology of these films (Fig. 3d-e) provides further insight to the trends in peak positions for each sample. While all three samples exhibit large-scale grain growth (~500x in CZTS to ~5,000x in Cu_2S), SnS_2 grows in a quasi-two-dimensional morphology (Fig. 3d), while Cu_2S and CZTS grow three-dimensionally (Fig. 3e, f). These SnS_2 structures grow similarly to other two-dimensional dichalcogenide materials like MoS_2 and WS_2.[26] Crucially for this experiment, the SnS_2 Raman mode tracked during the anneal is associated with phonon vibrations normal to the two-dimensional plane,[26] meaning there is less significant growth in the direction of phonon resonance, and there are negligible contributions to the peak position from crystal grain growth.

Being that the behavior of CZTS and Cu_2S peak positions resemble each other and that the majority of order/disorder and defect development dynamics occur at low temperatures (<300 ºC) in CZTS, we infer that we are observing the same phenomenon occurs in both phases. In Cu_2S, the most likely explanation for the discrepancy from this linear trend is a significant increase in crystal grain domain size, as there are no complex cation-substitution defect structures that can form to hinder phonon transport.[25] Applying the same logic to CZTS, we may identify a temperature regime in which significant crystal grain growth occurs. With the present experiment, we can only say this temperature exists somewhere between 500 and 600 ºC, but the result stresses the importance of the relatively high annealing temperature used in this and other works.

5.4: Low Temperature Characterization

At low temperatures, it has been demonstrated that defect structures in kesterite CZTS can be characterized using Raman spectroscopy, and an estimate for the degree of cation ordering in the material can be produced. In kesterite CZTS, the most likely defects occur at copper and zinc sites in the z = 1/4 and 3/4 planes due to the atoms' shared valence charge and similar atomic size and mass.[27] Scragg *et al.* identified an second order order/disorder transition (ODT) at a critical temperature near 260 ºC, where cation ordering in a CZTS film is established depending on the rate of cooling in accordance with Vineyard's theory of order in a solid.[12,28] The model is a thermodynamic rate equation, where there is some finite probability of copper atoms residing in copper lattice sites (P_{Cu}^{Cu}) and zinc atoms residing in zinc lattice sites (P_{Zn}^{Zn}), yielding an order parameter S:

$$S = 2\left(P_{Cu}^{Cu} - \frac{1}{2}\right) = 2\left(P_{Zn}^{Zn} - \frac{1}{2}\right) \qquad \text{(Eq. 1)}$$

where $S = 1$ denotes a fully ordered sample.[29] The atoms have some likelihood of interchanging with their nearest neighbors dependent on the thermodynamic conditions (k_BT), indicating that the rate of ordering can be controlled in conjunction with the rate of change in k_BT.[29]

Rudisch *et al*. have demonstrated that the order parameter *S* is linearly proportional to values (Q, Q′) that can be deduced from the ratios of different CZTS peaks in Raman spectra using a near-resonance probe (785 nm is near-resonant with the CZTS conduction band gap),[14] where:

$$Q = \frac{I_{288}}{I_{305}} \qquad \text{Eq. 2}$$

$$Q = \frac{I_{339}}{I_{368}+I_{377}} \qquad \text{Eq. 3}$$

An example fit of a Raman spectrum collected from a reasonably well-ordered CZTS sample is shown in Fig. 4a, and Q is calculated to be 2.11 while Q′ is calculated to be ~1.94. Paris *et al*. argue that physically Q and Q′ are representative of different defect complexes, and can be used to characterize the CZTS as "A-type" (containing predominantly [V_{Cu}+Zn_{Cu}] complexes) or "B-type" (containing predominantly [$2Zn_{Cu}$+Zn_{Sn}] complexes).[29] B-type CZTS has been used in efficient PV devices, and is more commonly reported than A-type. B-type character is indicated by Q ~ Q′ and Q < 2.8.[14,29] In the work by Rudisch *et al*., however, an *ex situ* Raman characterization

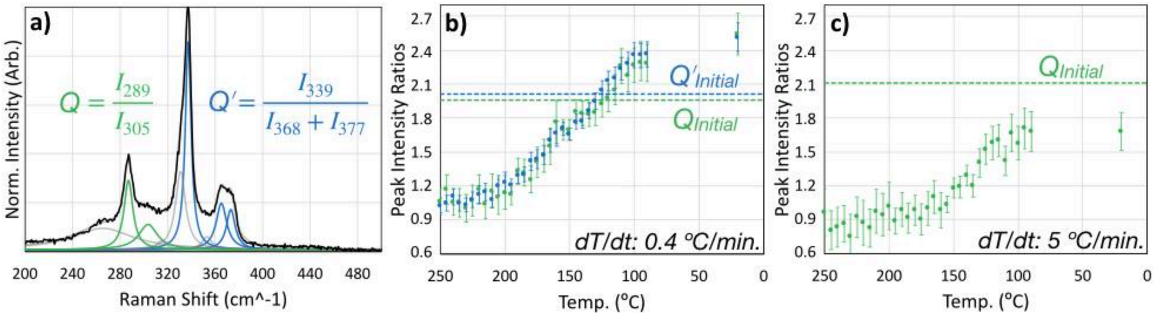

Figure 4: a) Sample Raman spectrum collected using 785 nm probe laser with peaks needed to calculate Q and Q' shown fit in green and blue, respectively. Also shows evolution in Q parameters over time for sample cooled at 0.4 ºC/min. (b) and 5 ºC/min. (c).

method was used,[14] and so the processing of multiple samples at increasingly slow cooling rates will have been lengthy and arduous. The ability to observe cation-order evolution *in situ* yields similar results from a single sample, as we demonstrate in this section.

We present experiments observing *in situ* the development of cation-ordering in CZTS films in a low temperature anneal using near-resonance Raman spectroscopy. In these experiments, two CZTS samples that have already been annealed using standard parameters after a 0.1 M Na_2S dip are used. These samples already exhibit a relatively high degree of cation ordering, with Q values of 2.11 and 1.96 and Q′ values of 1.94 and 2.01, respectively.

It should be noted that these three samples were processed in the same manner and all were cooled during the initial sulfur anneal at a rate of 3 ºC/min. For these experiments, the samples were re-sealed in ampoules with elemental sulfur, heated to steady state at 250 ºC, and then cooled at different rates in an attempt to change the cation-ordering in the kesterite CZTS. Using the 785 nm Raman probe to monitor the material structure, Q and Q′ are calculated for spectra acquired at continuous points during the cooling process. The sample in Fig. 4b was cooled at a rate of 0.4 ºC/min. and the sample in Fig. 4c was cooled at a rate of 5 ºC/min..

The values for both Q and Q′ are shown only in Fig. 4b, where they are approximately equivalent for all spectra measured. This indicates the material is B-type CZTS, matching the material used by Rudisch *et al.*[14] Q′ is not shown in Fig. 4c for clarity of the data, but the same character is assigned to each material.

The first observation is that the cation ordering in these samples is reversible according to the rate of cooling via a low-temperature annealing process, a result observed *ex situ*.[14,23,30] In Fig. 4b, the value of Q is 1.96 ± 0.14 after the initial anneal in which the sample was cooled at a rate of 3 ºC/min. After the secondary anneal with a cooling rate of 0.4 ºC/min., the value of Q is increased to 2.47 ± 0.15. Conversely, in Fig. 4c, the value of Q is 2.11 ± 0.15 after cooling at 3 ºC/min., and is reduced to 1.68 ± 0.13 after cooling at 5 ºC/min. This result is expected from Vineyard's theory of order, as the rate of order development (dS/dt ~ dQ/dt) is dependent on the rate of cooling (dT/dt).

Additionally, the development of cation order is different in the two samples. While other groups have asserted that cation-ordering begins upon cooling past a critical ODT temperature at ~260 ºC,[12,14,15,31] we observe the onset at different temperatures for each sample: ~210 ºC for the sample cooled at 0.4 ºC and ~165 ºC for the sample cooled at 5 ºC/min.

In considering the kinetics of a second order phase transformation, this variability in the temperature of the onset of ordering is not unexpected.[32] Additionally, noting that the rate of ordering as the samples are cooled (the slopes of the apparently linear increase in order with temperature) are the same, we may assert that the delayed onset of ordering in the sample cooled at 5 ºC/min. is physically analogous to the effect of quenching to suppress a first order phase transformation according to Ehrenfest's standard classification scheme.

5.5: Effect of Sodium Content on Material Evolution

In the experiments discussed in Sections 5.3 and 5.4, the films were all processed after dipping in a 0.1 M Na_2S solution. Given our ability to control the sodium content and the structural evolution of the film by changing the sodium content (Figs. 24 and 25 in Ch. 4), the samples dipped in higher Na_2S concentration solutions are interesting candidates for these *in situ* studies.

In both CZTS and CIGS, the presence of sodium is known to benefit both morphology development during thermal processing [4-7,33] and charge transport.[4,34,35] Gershon *et al*. studied the morphology and electrical performance in CZTS thin films with different amounts of sodium by deposition of a controllably thin sputtered NaF layer on the substrate prior to CZTS growth.[4] They note that sodium diffuses to internal and external surfaces in the material, effectively passivating large non-radiative defects. Crucially, though, they observed that this surface passivation effect was likely a separate phenomenon from the large-scale grain growth attributable to sodium, as the two effects were observed with different critical amounts of sodium in the film.[4] While the observation of sodium diffusion to surfaces is an important clue, there still has not been a clear and conclusive explanation for why sodium promotes grain growth in CZTS films. This is a question that can potentially be answered using a well-designed series of *in situ* experiments. While this work is not devoted to answering this question, we provide some preliminary data to suggest that our system could be applied effectively to give some insight into sodium-enhanced grain growth.

Similar to the experiments discussed in Sections 5.3 and 5.4 in which samples that had been dipped in 0.1 M Na_2S were studies, the same experiments were conducted on samples that were dipped in 0.5 M Na_2S. From Figs. 24 and 25 (in Ch. 4), this condition yields samples consisting of large crystal grains with a combination of CZTS and other phases resultant from CZTS decomposition. In the initial high-temperature sulfur anneal, the CZTS peak position was monitored as a function of temperature (like in Fig. 3). After the initial annealing process, the sample was annealed again at low temperature, and the development of cation order was observed (like in Fig. 4). Noting that there is significant phase-inhomogeneity in the film after the first anneal, in the second anneal, the sample was manipulated to find a spot with a significant contribution from CZTS to the Raman spectrum. The results of these studies may be compared with those from Sections 5.3 and 5.4 to draw conclusions from the differences observed.

In Fig. 5a, we may compare the critical temperature at which the peak position

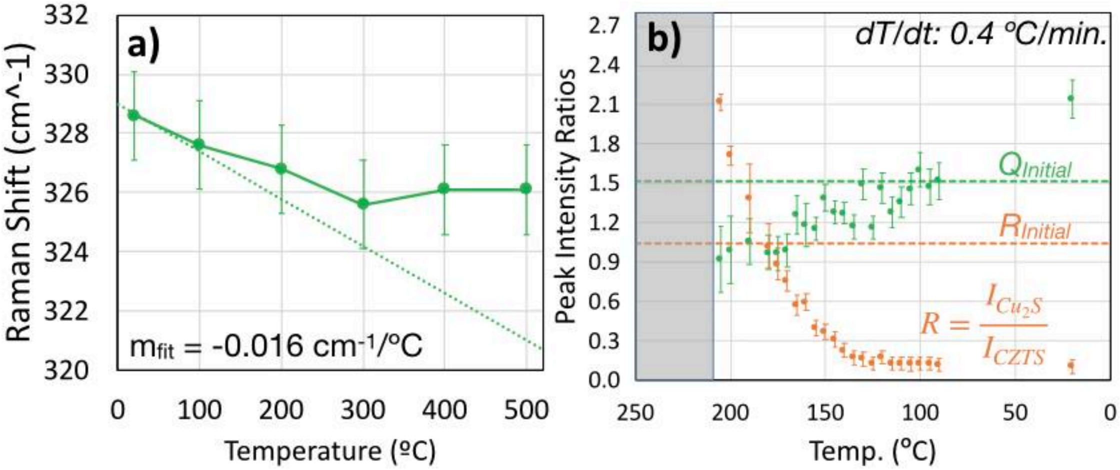

Figure 5: a) Shows measured CZTS peak position vs. temperature for 0.5 M dipped sample. b) Shows development of cation ordering (Q) and phase homogeneity (R) during cooling ramp of secondary low temperature anneal process.

deviates from the linear trend shown by the dashed line with that for the sample dipped at lower Na_2S concentration. While in Fig. 3c, the critical temperature we assign to be an indication of crystal domain growth is near 500 ºC, in the higher dip concentration sample, this critical temperature appears to have been reduced to near 300 ºC. Also, it is necessary to note that above 500 ºC, all discernible features in the Raman spectrum disappeared, and upon cooling the sample, very little contribution to the spectrum from CZTS was seen (like in the 0.5 M dipped sample in Fig. 25 in Ch. 4). From these and other *ex situ* observations of this sample, it is likely there is more contributing to the deviation in peak position from what we expect with increasing temperature, like phase decomposition or large-scale defect complex formation.

There is, however, previous work that indicates the increased presence of sodium may be significantly altering the surface energy of the CZTS crystal grains, thereby changing the thermodynamic activation energy for grain growth in different phases or along different crystal plane orientations. All conclusions are predicated on sodium diffusing to and aggregating at surfaces and grain boundaries during thermal processing. Hlaing Oo *et al.* observed the preferential growth of CZTS crystal grains normal to the ⟨112⟩ direction with the presence of sodium, while there was no preferential growth with no sodium.[33] The reduction of nucleation and growth activation energy in this orientation is inferred, which may be attributed to a reduction in surface energy associated with sodium bonding to sulfur or contaminant oxygen in the system.[33-35]

Additionally, Rockett notes that in the CIGS system, where sodium has a similar effect on grain morphology and electrical properties to CZTS, sodium acts to enhance or suppress nucleation processes or atomic diffusivity.[35] Though much experimental work is conflicting due to the nature of the experimental setup, Rockett claims that sodium acts to increase activation energies to suppress grain growth kinetics in CIGS,[35] which is the converse of what we observe here in CZTS. Additionally, the presence of sodium may have a similar effect on the nucleation kinetics of defects in bulk crystal grains, where the high sodium diffusivity in the material leads to the formation of defect clusters.[34,35] These clusters are passivated in a similar manner to grain boundaries in the presence of sodium, and thus have minimal effect on device performance.

In sum, using the *in situ* Raman technique described here, it appears we can characterize the effect of sodium on grain growth kinetics, and our preliminary data suggests that sodium causes a reduction in surface energies that enhance grain growth kinetics in CZTS. However, to characterize the nucleation and growth of defects and defect clusters, the experiment must be optimized to yield enhanced signal at high temperatures to allow for the comparison of different CZTS modes, rather than the detection of only the dominant mode at 339 cm^{-1}, similar to the low-temperature observation of defect evolution we described in Section 5.4.

We observe the evolution of defects and cation ordering in the 0.5 M Na_2S-dipped sample in Fig. 5b as well. While we acknowledge the structure is highly inhomogeneous both structurally and morphologically prior to the secondary anneal (Figs. 24 and 25 in Ch. 4), the observation of a specific location containing a relatively high CZTS phase-composition gives us insight into the effect of excess sodium on both the intra- and inter-phase dynamics of the material. Shown in Fig. 5b are values for Q at different temperatures during the slow-cooling process (cooled at the same 0.4 ºC as the sample in Fig. 4b). We also introduce a new term, R, which we use to represent the ratio of the intensity of the Cu_2S peak at 474 cm^{-1} to the intensity of the CZTS peak at 339 cm^{-1}. This allows a qualitative observation of the relative phase composition of the sample during the cooling ramp.

The initial values for Q and R prior to the secondary anneal are 1.51 and 1.04, respectively. In this sample, all features in the Raman spectra disappeared during the 90-minute hold at 250 ºC. This may be attributable to a number of causes including laser-induced effects, so will not be considered in detail here. During the cooling ramp, spectral features reappeared at 205 ºC, with the Q value of 0.92 indicating fully cation-disordered CZTS. The R value of 2.12 at this temperature point likely indicates substantial phase decomposition even from this low temperature thermal process, which was not observed in samples dipped at lower Na_2S concentrations. However, during the remainder of the cooling ramp, the R value decreases continuously until it reaches a minimum asymptote at T ~ 135 ºC, indicating the sample is approximately phase-pure CZTS.

The cation ordering within the CZTS phase is increased to be fairly high at the conclusion of the process as well with Q at 2.14, though the progression of the ordering is less statistically clear than it was for the sample in Fig. 4b. This result has a very important implication: that not only is the cation ordering within kesterite CZTS reversible via a low temperature annealing process, but structural homogeneity may be reversible at low temperatures as well by controlling sodium content in the sample and the cooling rate.

To show the significance of this implication, we have included SEM images and EDS maps indicating the distribution of Zn, Cu, and Sn in the 0.5 M dipped sample after the initial anneal (Fig. 6a-d) and after the second low temperature anneal (Fig. 6e-h). These are not the same spots, but they are representative of the samples at each point. After the initial anneal, the sample is compositionally inhomogeneous, as expected from the Raman spectrum (Fig. 25 in Ch. 4). Highlighted in Fig. 6a-d are spots in which each of Zn, Cu, and Sn can be observed independently from the other two cation elements, though there is some mixing of the elements as well. This implies the sample consists of a mixture of ZnS, Cu_xS, SnS_x, Cu_xSn_yS, and CZTS. In Fig. 6e, however, the film is re-homogenized morphologically, and Fig. 6f-h show the atomic distribution is more homogenous as well, corroborating the phase-pure CZTS structure apparent from the Raman spectrum.

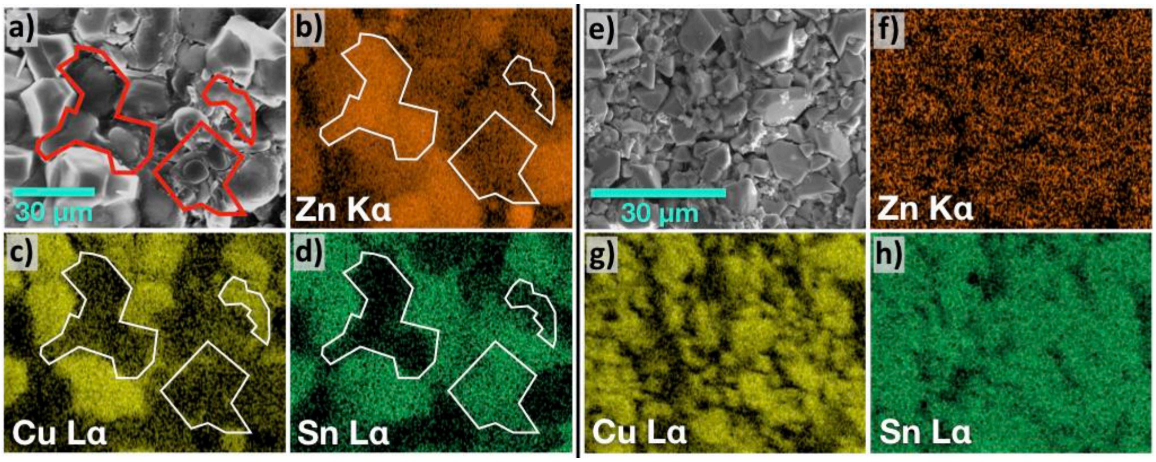

Figure 6: Shows SEM images of 0.5 M dipped sample after initial anneal (a) and after secondary anneal (e). Also shows EDS maps indicating composition distribution of Zn, Cu, and Sn in each sample.

5.6: Conclusions

In this work, we have demonstrated the application of *in situ* Raman spectroscopy conducted on CZTS thin film samples as they are processed at high temperatures in volatile sulfur atmospheres. A technique was developed to controllably process CZTS nanoparticle coatings into uniform large grain films for potential use as the absorber layer in thin film PVs by means of a facile Na_2S solution-dip followed by thermal annealing in a closed system of low-pressure sulfur vapor. Varying the concentration of the Na_2S solution allows a straightforward means of controlling morphology and structural-phase evolution during the annealing process, as characterized by standard *ex situ* methods.

Using the *in situ* Raman characterization process described here, we have demonstrated the ability to monitor the development of long-range crystal domains in CZTS. We have also demonstrated an application of Vineyard's theory of order to quantify the degree of order with respect to copper and zinc lattice-site distribution in the kesterite CZTS crystal lattice. Observing the development of order *in situ* allows us to characterize the kinetics of the second-order phase transition more accurately than is possible using *ex situ* techniques, in particular how the kinetics are controlled by changing the cooling rate of the sample. Finally, we demonstrated how our *in situ* technique may provide experimental evidence to develop more complete theories on the effect of sodium on structural and morphological development during thermal processing of CZTS. We have additionally confirmed that both cation disorder in kesterite CZTS and structural homogeneity in a CZTS film are reversible via a low temperature thermal process.

5.7: References

(1) Du, H.; Yan, F.; Young, M.; To, B.; Jiang, C.; Dippo, P.; Kuciauskas, D.; Chi, Z.; Lund, E. A.; Hancock, C.; Hlaing Oo, W. M.; Scarpulla, M. A.; Teeter, G. Investigation of Combinatorial Coevaporated Thin Film Cu2ZnSnS4. I. Temperature Effect, Crystalline Phases, Morphology, and Photoluminescence. *Journal of Applied Physics*, **2014**, *115*(17), 173502.

(2) Wang, Z.; Elouatik, S.; Demopoulos, G. Understanding the Phase Formation Kinetics of Nano-Crystalline Kesterite Deposited on Mesoscopic Scaffold via In-Situ Multi-Wavelength Raman-Monitored Annealing. *Physical Chemistry Chemical Physics*, **2016**, *18*, 29435-29446.

(3) Sayed, M. H.; Brandl, M.; Chory, C.; Hammer-Riedel, I.; Parisi, J.; Gütay, L.; Hock, R. In-Situ XRD Investigation of Re-Crystallization and Selenization of CZTS Nanoparticles. *Journal of Alloys and Compounds*, **2016**, *686*, 24-29.

(4) Johnson, M; Baryshev, S. V.; Thimsen, E.; Manno, M.; Zhang, X.; Veryovkin, I. V.; Leighton, C.; Aydil, E. Alkali-Metal-Enhanced Grain Growth in Cu2ZnSnS4 Thin Films. *Energy & Environmental Science*, **2014**, *7*, 1931-1938.

(5) Gershon, T.; Shin, B.; Bojarczuk, N.; Hopstaken, M.; Mitzi, D. B.; Guha, S. The Role of Sodium as a Surfactant and Suppressor of Non-Radiative Recombination at Internal Surfaces in Cu2ZnSnS4. *Advanced Energy Materials*, **2015**, *5*, 1400849.

(6) Sutter-Fella, C. M.; Stückelberger, J. A.; Hagendorfer, H.; La Mattina, F.; Kranz, L.; Nishiwaki, S.; Uhl, A. R.; Romanyuk, Y. E.; Tiwari, A. N. Sodium Assisted Sintering of Chalcogenides and Its Application to Solution Processed Cu2ZnSn(S,Se)4 Thin Film Solar Cells. *Chemistry of Materials*, **2014**, *26*, 1420-1425.

(7) Tiong, V. T.; Hreid, T.; Zhang, S.; Bell, J.; Wang, H. Morphology Evolution and Stability of Cu2ZnSnS4 Nanocrystals in Sodium Halides Salt Solution. *Thin Solid Films*, **2016**, *615*, 305-310.

(8) Alvarez, A.; Exarhos, S.; Mangolini, L. Tin Disulfide Segregation on CZTS Films Sulfurized at High Pressure. *Materials Letters*, **2016**, *165*, 41-44.

(9) Chernomordik, B. D.; Béland, A. E.; Deng, D. D.; Francis, L. F.; Aydil, E. S. Microstructure Evolution and Crystal Growth in Cu2ZnSnS4 Thin Films Formed by Annealing Colloidal Nanocrystal Coatings. *Chemistry of Materials*, **2014**, *26*, 3191-3201.

(10) Just, J.; Sutter-Fella, C. M.; Lützenkirchen-Hecht, D.; Frahm, R.; Schorr, S.; Unold, T. Secondary Phases and Their Influence on the Composition of the Kesterite

Phase in CZTS and CZTSe Thin Films. *Physical Chemistry Chemical Physics*, **2016**, *18*, 15988-15994.

(11) Schorr, S. Structural Aspects of Adamantine Like Multinary Chalcogenides. *Thin Solid Films, Proceedings of Sympodium O on Thin Film Chalcogenide Photovoltaic Materials, EMRS 2006 Conference*, **2006**, *515*(15), 5985-5991.

(12) Scragg, J. J. S.; Choubrac, L.; Lafond, A.; Ericson, T.; Platzer-Björkman, C. A Low-Temperature Order-Disorder Transition in Cu2ZnSnS4 Thin Films. *Applied Physics Letters*, **2014**, *104*, 041911.

(13) Lund, E. A.; Du, H.; Hlain Oo, W. M.; Teeter, G.; Scarpulla, M. A. Investigation of Combinatorial Coevaporated Thin Film Cu2ZnSnS4. II: Beneficial Cation Arrangement in Cu-Rich Growth. *Journal of Applied Physics*, **2014**, *115*(17), 173503.

(14) Rudisch, K.; Ren, Y.; Platzer-Björkman, C.; Scragg, J. Order-Disorder Transition in B-Type Cu2ZnSnS4 and Limitations of Ordering Through Thermal Treatments. *Applied Physics Letters*, **2016**, *108*(23), 231902.

(15) Rey, G.; Weiss, T. P.; Sendler, J.; Finger, A.; Spindler, C.; Werner, F.; Melchiorre, M.; Hála, M.; Guennou, M.; Siebentritt, S. Ordering Kesterite Improves Solar Cells: A Low Temperature Post-Deposition Annealing Study. *Solar Energy Materials and Solar Cells*, **2016**, *151*, 131-138.

(16) Duren, S. Van; Ren, Y.; Scragg, J.; Just, J.; Unold, T. In Situ Monitoring of Cu2ZnSnS4 Absorber Formation with Raman Spectroscopy During Mo/Cu2SnS3/ZnS Thin-Film Stack Annealing. *IEEE Journal of Photovoltaics*, **2017**, *7*, 906-912.

(17) Alvarez Barragan, A.; Malekpour, H.; Exarhos, S.; Balandin, A. A.; Mangolini, L. Grain-to-Grain Compositional Variations and Phase Segregation in Copper-Zinc-Tin-Sulfide Films. *ACS Applied Materials & Interfaces*, **2016**, *8*(35), 22971-22976.

(18) Valle Rios, L. E.; Neldner, K.; Gurieva, G.; Schorr, S. Existence of Off-Stoichiometric Single Phase Kesterite. *Journal of Alloys and Compounds*, **2015**, *657*, 408-413.

(19) Exarhos, S.; Palmes, E.; Xu, R.; Mangolini, L. Oxide-Induced Grain Growth in CZTS Nanoparticle Coatings. *RSC Advances*, **2017**, *7*(41), 25575-25581.

(20) Huang, D.; Persson, C. Band Gap Change Induced by Defect Complexes in Cu2ZnSnS4. *Thin Solid Films*, **2013**, *535*, 265-269.

(21) Ng, T. M.; Weller, M. T.; Kissling, G. P.; Peter, L. M.; Dale, P.; Babbe, F.; Wild, J. de; Wenger, B.; Snaith, H. J.; Lane, D. Optoelectronic and Spectroscopic

Characterization of Vapour-Transport Grown Cu2ZnSnS4 Single Crystals. *Journal of Materials Chemistry A*, **2017**, *5*, 1192-1200.

(22) Valentini, M.; Malerba, C.; Menchini, F.; Tedeschi, D.; Polimeni, A.; Capizzi, M.; Mittiga, A. Effect of the Order-Disorder Transition on the Optical Properties of Cu2ZnSnS4. *Applied Physics Letters*, **2016**, *108*, 211909.

(23) Krämmer, C.; Huber, C.; Zimmermann, C.; Lang, M.; Schnabel, T.; Abzieher, T.; Ahlswede, E.; Kalt, H.; Hetterish, M. Reversible Order-Disorder Related Band Gap Changes in Cu2ZnSn(S,Se)4 via Post-Annealing of Solar Cells Measured by Electroreflectance. *Applied Physics Letters*, **2014**, *105*, 262104.

(24) Just, J.; Nichterwitz, M.; Lützenkirchen-Hecht, D.; Frahm, R.; Unold, T. Compositional Dependence of Charge Carrier Transport in Kesterite Cu2ZnSnS4 Solar Cells. *Journal of Applied Physics*, **2016**, *120*(22), 225703.

(25) Gouadec, G.; Colomban, P. Raman Spectroscopy of Nanomaterials: How Spectra Relate to Disorder, Particle Size and Mechanical Properties. *Progress in Crystal Growth and Characterization of Materials*, *Elsevier*, **2007**, *53*, 1-56.

(26) Huang, Y.; Sutter, E.; Dadowski, J. T.; Cotlet, M.; Monti, O. L. A.; Racke, D. A.; Neupane, M. R.; Wickramaratne, D.; Lake, R. K.; Parkinson, B. A.; Sutter, P. Tin Disulfide—An Emerging Layered Metal Dichalcogenide Semiconductor: Materials Properties and Device Characteristics. *ACS Nano*, **2014**, *8*, 10743-10755.

(27) J.J. Scragg, T. Ericson, T. Kubart, M. Edoff, and C. Platzer-Björkman. *Chemistry of Materials*, 2011, 23(**20**), 4625-33.

(28) Vineyard, G. H. Theory of Order-Disorder Kinetics. *Physical Review*, **1956**, *102*(4), 981-992.

(29) Paris, M.; Choubrac, L.; Lafond, A.; Guillot-Deudon, C.; Jobic, S. Solid-State NMR and Raman Spectroscopy to Address the Local Structure of Defects and the Tricky Issue of the Cu/Zn Disorder in Cu-Poor, Zn-Rich CZTS Materials. *Inorganic Chemistry*, **2014**, *53*, 8646-8653.

(30) Scragg, J. J. S.; Larsen, J. K.; Kumar, M.; Persson, C.; Sendler, J.; Siebentritt, S.; Platzer Björkman, C. Cu-Zn Disorder and Band Gap Fluctuations in Cu2ZnSn(S,Se)4: Theoretical and Experimental Investigations. *Physica Status Solidi (B)*, **2016**, *253*, 247-254.

(31) Többens, D. M.; Gurieva, G.; Levcenko, S.; Unold, T.; Schorr, S. Temperature Dependency of Cu/Zn Ordering in CZTSe Kesterites Determined by Anomalous Diffraction. *Physica Status Solidi (B)*, **2016**, *253*(10), 1890-1897.

(32) Lifshitz, I. M. Kinetics of Ordering During Second-Order Phase Transitions. *Soviet Physics JETP*, **1962**, *15*, 939-942.

(33) Oo, W. M. H.; Johnson, J. L.; Bhatia, A.; Lund, E. A.; Nowell, M. M.; Scarpulla, M. A. Grain Size and Texture of Cu2ZnSnS4 Thin Films Synthesized by Cosputtering Binary Sulfides and Annealing: Effects of Processing Conditions and Sodium. *Journal of Electronic Materials*, **2011**, *40*, 2214-2221.

(34) Rudmann, D.; Brémaud, D.; Zogg, H.; Tiwari, A. N. Na Incorporation into Cu(In,Ga)Se2 for High-Efficiency Flexible Solar Cells on Polymer Foils. *Journal of Applied Physics*, **2005**, *97*, 084903.

(35) Rockett, A. The Effect of Na in Polycrystalline and Epitaxial Single-Crystal CuIn1-xGaxSe2. *Thin Solid Films*, **2005**, *480-481*, 2-7.

Chapter 6: Zirconium Nitride Nanoparticle Synthesis and Characterization

6.1: Introduction

Localized surface plasmon resonance (LSPR) has garnered interest in a variety of fields recently, such as photocatalysis,[1] photovoltaics,[2] solar thermophotovoltaics,[3] biophotonics,[4] spectroscopy,[5] sensing,[6] and wave-guiding.[7] LSPR is correlated with the density of free charge carriers,[8] so metals tend to have the highest LSPR frequency within the visible spectrum. Gold and silver nanostructures have been applied in all of the fields mentioned above because of the ease with which they can be produced at the lab scale.[9–11] However, concerns related to cost, material abundance, and thermal stability motivate the search for alternative plasmonic materials. Among such alternatives, group IVB transition-metal nitrides show particular promise.[12–14]

Group IVB transition-metal nitrides have been well studied in hard-coating applications due to their high thermal stability and ceramic-like mechanical properties.[13] These materials exhibit metal-like electronic properties — they have high charge carrier concentrations that contribute to high-frequency LSPR behavior.[8,15] Further, these materials can be stably produced with a variety of metal-to-nitride stoichiometric ratios, which in turn allows a degree of tunability of the resonant plasmonic frequency.[12] In comparison, tuning the resonant plasmonic frequency in precious metal nanoparticles requires tuning the size, shape, or morphology of the structures.[11,16–18] Among Group IVB nitrides, titanium nitride (TiN) thin films and nanoparticles have recently attracted significant attention.

While several theoretical and experimental studies have demonstrated plasmonic extinction in transition-metal nitrides, particularly for TiN in the near-infrared region of the spectrum, the absorption component of the extinction is significantly larger than the scattering component, particularly for small nanoparticles.[14,19–21] This has implications for the intended application of the material. Scattering mechanisms are more well suited for near-field enhancement applications like surface enhanced Raman scattering (SERS) or plasmon-driven catalysis.[22,23] In contrast, absorption mechanisms lend well to localized thermal applications like solar thermophotovoltaics,[24] photo-thermal cellular therapy,[25] or heat-assisted magnetic recording.[26] The refractory nature of these transition-metal nitride materials in combination with their high absorption efficiency indicate their suitability for new absorption-mediated applications where standard nanostructured metal devices are only suitable for use at low temperatures.[13]

For high energy transition-metal nitride plasmonics applications, a blue-shifted plasmonic resonance relative to that exhibited by TiN nanoparticles would be preferred. This blue shift can be accomplished by replacing the transition-metal cation with larger Group IVB atoms like zirconium or hafnium.[27] Lalisse *et al.*, Guler *et al.*, and others offer theoretical validation for the near-field enhancement properties of small (5-10 nm) spherical ZrN nanoparticles at resonant wavelengths around 500 nm, with thermoplasmonic properties equivalent to or exceeding those of gold.[12,14,28]

There has been little work experimentally studying LSPR in zirconium nitride (ZrN) thin films, and only one previous work experimentally studying LSPR in ZrN nanoparticles by Reinholdt *et al.*,[29] though the nanoparticles were not free-standing but deposited onto a silica substrate. Reinholdt *et al.* used laser ablation of a compacted ZrN powder target in an N_2 atmosphere to produce monodisperse ZrN nanoparticles with sizes less than 10 nm.[29] These particles were characterized *in situ* by optical transmission spectroscopy and exhibited a plasmonic extinction within the visible spectrum.[29] ZrN nanoparticles have also been made by zirconium wire explosion in a nitrogen atmosphere,[30] by pulsed wire discharge,[31] and by microwave-mediated synthesis.[32] None of these latter three processes succeeded in creating uniform small ZrN nanoparticles, and none of these particles were characterized optically.[30–32]

In the course of our group's experimentation with synthesizing both TiN and ZrN nanoparticles, we have identified that oxidation plays a significant role in the materials' LSPR behavior, a conclusion shared by other experimental works.[20,21,29] With small nanoparticles in particular, controlling oxidation may be more significant than controlling stoichiometry in determining the material's plasmonic behavior, because the native surface oxidation that occurs upon exposure to air is takes up an increasingly large fraction of particles as the bulk volume of the particles decreases. The stability of ZrN against oxidation is contingent on the relative compositions of zirconium and nitrogen in the material, as off-stoichiometric compositions are less stable than ZrN with a near-unity molar ratio.

Oxidation in bulk transition-metal nitride coatings intended for use as hard protective coatings in mechanical applications has been well-studied,[33] and various solutions have been proposed.[34–38] One solution of particular interest is to incorporate non-metallic elements such as silicon into the material.[38] In these ZrN thin films and coatings, silicon tends to form a SiN_x phase, which surrounds the transition-metal nitride crystal grains in an amorphous matrix, as the silicon is more likely to form covalent Si-N bonds than metallic alloy bonds.[37–39] This work has inspired the incorporation of a silicon-derived oxidation barrier to reduce detrimental oxidation of the produced ZrN nanoparticles. Further elaboration on the mixed effects the coating lends to the LSPR in the ZrN nanoparticles described in this work is discussed later on.

In this chapter, I demonstrate the synthesis of plasmonic ZrN nanoparticles using a scalable non-thermal plasma process. I produce surface-ligand-free spherical nanoparticles with uniform size distributions between 5-10 nm. The material is characterized structurally, compositionally, and optically to compare the material I produce to theoretically predicted behavior for ZrN nanoparticles. Through intensive material characterization and finite-difference time-domain (FDTD) simulations of the LSPR behavior for pure ZrN and oxidized ZrN nanoparticles, I identify oxidation as the dominant factor differentiating the material I produce from the ideal material. Though oxidation plays a more significant role in the performance of the particles than anticipated, the modularity of the non-thermal plasma system allows us to easily introduce a conformal thin amorphous SiN_x coating to the particles to mitigate this effect. The coating significantly improves not only the optical response of the particles as-produced, but also significantly improves oxidation resistance at high temperatures. I then compare the stability of the LSPR behavior of both the coated and un-coated nanoparticles at high temperatures in oxidative environments. I conclude with a discussion on potential applications of this material and on implications for this field moving forward.

6.2: Non-Thermal Plasma Synthesis of Transition Metal Nitrides

Zirconium nitride, with a melting temperature of 2952 ºC,[40] is difficult to produce using thermal processes. Temperatures above 1,100 ºC are required for the reaction between $ZrCl_4$ and NH_3 to proceed to completion.[41] However, the highly reactive environment provided by a non-thermal plasma can effectively initiate reactions at room temperature that would otherwise require high temperature environments.[42–44]

Using a non-thermal plasma reactor design similar to that used to produce silicon quantum dots,[42] I ionize a mixture of vaporized anhydrous $ZrCl_4$ (Alpha Aesar), NH_3 (AirGas) and Ar to produce ZrN nanoparticles. A schematic of the reactor is shown in Fig. 1. The delivery of the zirconium precursor requires special attention, since $ZrCl_4$ has a relatively low vapor pressure and is solid at room temperature.[45] To precisely control the vapor pressure and the effective flow rate of $ZrCl_4$ in the system, the precursor is placed in an alumina boat inside a tube furnace upstream of the plasma reactor. Controlling the temperature of the furnace and the pressure inside the system allows

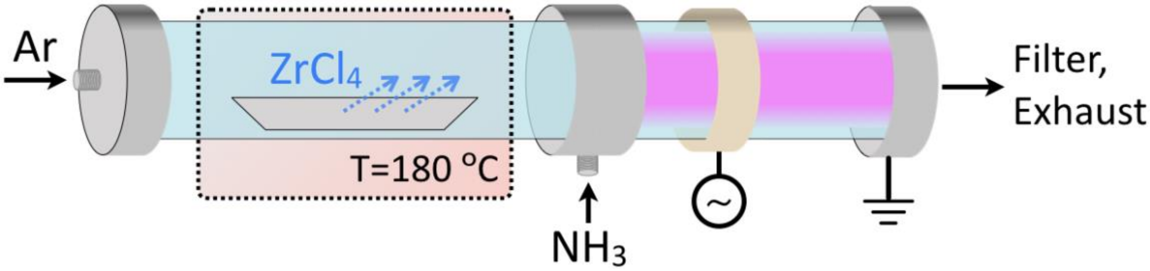

Figure 1: Schematic of non-thermal plasma system used to produce ZrN nanoparticles.

control of the effective $ZrCl_4$ flow rate (Fig. 2). For all samples discussed in this chapter, the furnace was held at 180 ºC and the pressure was 5 torr. For an argon carrier gas flow of 90 sccm, the estimated flow of $ZrCl_4$ introduced to the gas flow is 18 sccm. Correspondingly, the residence time in the plasma reactor, calculated based on the total gas flow velocity, is 230 ms (Fig. 3). 10 sccm of NH_3 is injected into the system downstream of the heated $ZrCl_4$ chamber and allowed to mix with the precursor vapors prior to entering the plasma. The gas mixture is flowed through a 2.5 cm-diameter quartz tube with a 5 cm-wide thin copper plate wrapped around as the electrode. The vacuum flange downstream of the electrode serves as electrical ground, with a distance of ~12.5 cm separating the downstream-edge of the electrode and the ground. The gas is ionized in a 180 W capacitively-coupled plasma driven by a 13.56 MHz (RF) power supply. Any

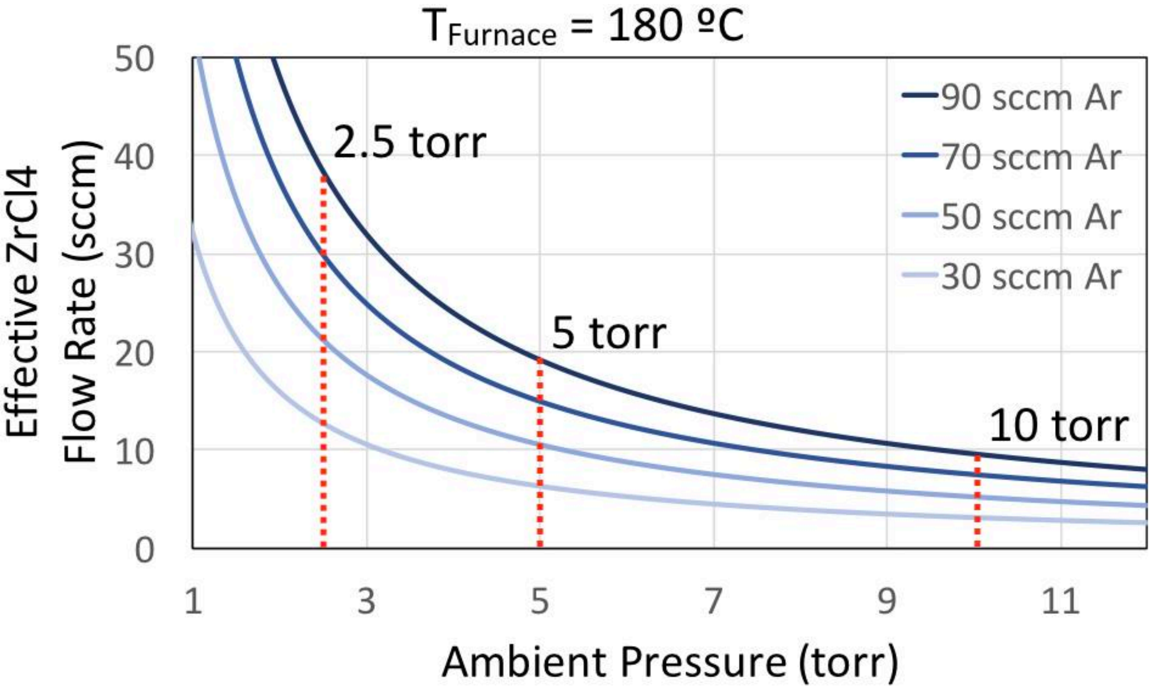

Figure 2: Estimated $ZrCl_4$ flow rate calculated from system pressure and Ar carrier gas flow rate.

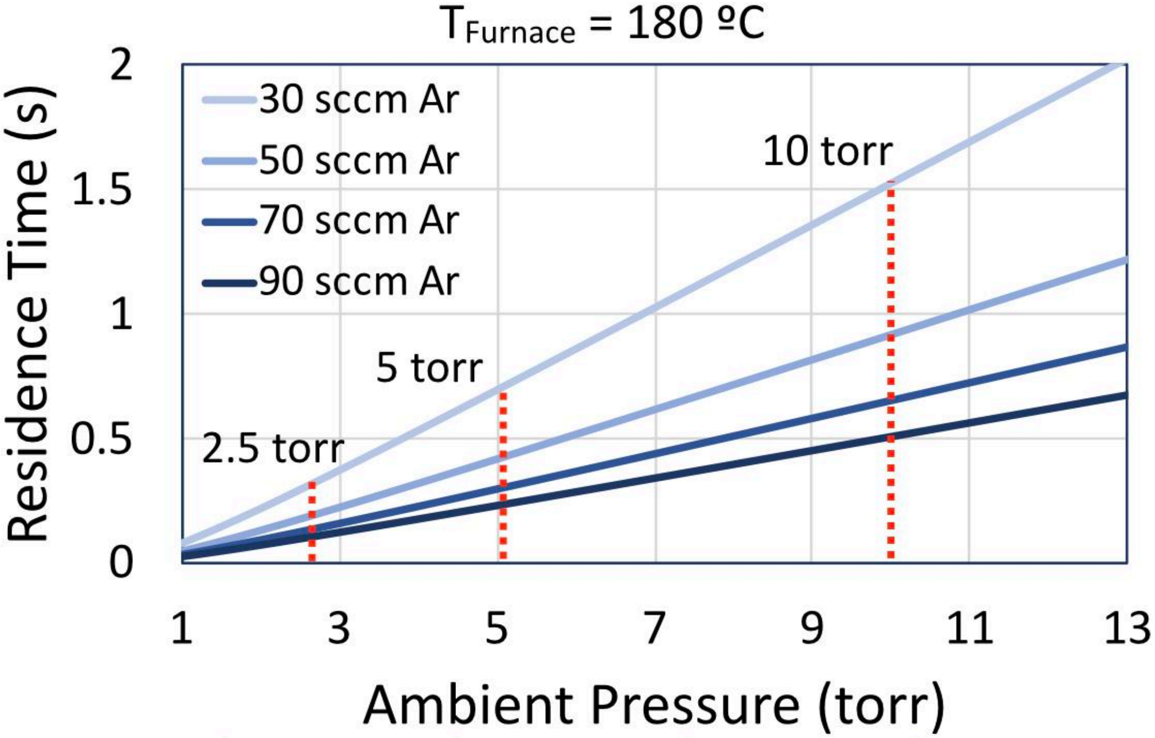

Residence time (s):	90 sccm Ar	70 sccm Ar	50 sccm Ar	30 sccm Ar
2.5 torr	0.099	0.127	0.178	0.296
5 torr	0.232	0.299	0.418	0.696
10 torr	0.509	0.654	0.915	1.524

Figure 3: Estimated plasma residence time calculated based on Ar carrier gas flow rate and system pressure. Numeric values are listed in the table below.

product is collected downstream on a stainless-steel mesh filter.

The product as-collected from this system is contaminated by ammonium salts, which are a by-product of the $ZrCl_{4,(v)}$-NH_3 reaction.[41] To isolate the produced ZrN nanoparticles, the mesh filter is annealed at 250 ºC and 0.30 torr in 90 SCCM of argon flow for one hour. X-Ray diffraction (XRD) of a produced sample shows a presence of NH_4Cl + ZrN before this annealing process, and pure cubic-ZrN afterwards (Fig. 4). With optimized or near-optimized operating conditions, the powder production rate is ~20

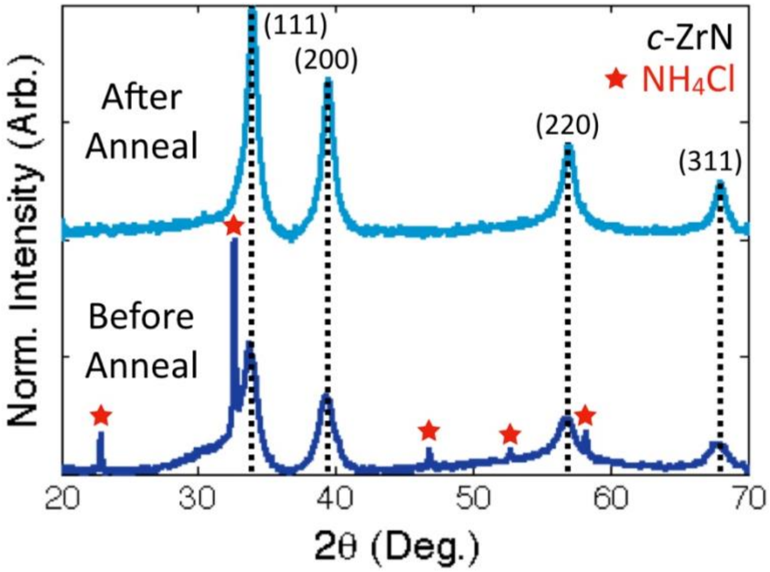

Figure 4: XRD patterns from ZrN product both before and after removal of NH_4Cl contaminant.

mg/hr (this value accounts for the mass of powder produced by the plasma process and does not account for the annealing treatment, in which several samples can be processed simultaneously).

The ZrN product is characterized with XRD, transmission electron microscopy (TEM), and UV/Vis/NIR spectrophotometry. XRD is performed on a PANalytical Empyrean X-Ray system using Cu Kα radiation with a wavelength of 1.54 Å. Standard TEM is performed using a Tecnai12 instrument with a standard accelerating voltage of 120 kV. High-resolution STEM imaging is performed with a FEI Titan Themis 300 instrument with energy dispersive X-ray spectroscopy (EDS) capability. EDS spectra were processed using Bruker Instruments Esprit 1.9 software. Quantification is based on the Cliff-Lorimer approach using calculated k-factors and correcting for thickness by estimating the size of the aggregated particles. Spectrophotometry was performed on dispersions of powder in polar solvents (deionized – DI – water, ethanol, and ethylene glycol were used in this work) with a Varian Cary 500 UV-Vis-NIR spectrophotometer. Samples were prepared by diluting 1 mg of powder in 5 mL of solvent and sonicating for 30 minutes, forming a stable dispersion. Stable dispersions (dispersions in which particle sedimentation occurs no sooner than three days after initial sonication) are possible in all polar solvents that I have tested.

6.3: Theoretical Methods

Simulations of the optical response from ZrN nanoparticles were conducted following the process described by Li *et al.*[46] Optical spectra were generated using an FDTD-solver for Maxwell's equations in the package: FDTD Solutions, v8.20 from Lumerical, Inc. The nanoparticles were modeled as a single sphere with 10 nm diameter, though I simulated various oxidized ZrN geometries and ZrN-Si3N4 core-shell particles as well. For the core-shell oxidized ZrN geometries used in the text below, I subtracted a conformal shell of a given thickness from the surface of a 10 nm diameter sphere and calculated the volume change that occurs in transforming ZrN to ZrO2, under the assumption that the number of Zr atoms remained constant. For the ZrN-Si3N4 core-shell geometries, I modeled a conformal shell of a given thickness on the surface of a 10 nm diameter ZrN particle. To calculate optical properties of a material, these simulations require the material's real and imaginary dielectric constant as a function of wavelength. For Si3N4, I used the data provided in the software package from Philip.[47] For ZrN and ZrO2, I calculated values spanning the wavelength range 300-1500 nm from the material database of Palik.[48] For homogeneous mixtures of ZrN and ZrO2, I calculated the real and imaginary parts of the dielectric function based on the Maxwell-Garnet model.[49,50] Total-field/scattered-field light source conditions were used in all simulations. The light was set to span 350 nm to 1500 nm in wavelength and was injected and polarized along the y-axis. A uniform mesh step of 0.25 nm was used in all simulations.

6.4: Characterization of ZrN Nanoparticles

Structural and morphological characterization of a ZrN sample produced under optimized conditions (furnace temperature 180 ºC, system pressure 5 torr, Ar carrier gas flow rate 90 sccm, NH_3 flow rate 10 sccm) is presented in Fig. 5. The TEM micrograph (Fig. 5a) shows the crystalline ZrN particles have a generally spherical shape and are fairly monodisperse in size. A particle size-distribution was generated from a series of low-magnification TEM images, showing an average particle size of 8.4 nm with a standard deviation of 2.3 nm (Fig. 6), which is comparable to that of other nanoparticles produced with a reactor of this type.[20,42] In Fig. 2b, the XRD pattern indicates the presence of cubic-phase ZrN. The high-resolution STEM image in Fig. 5c and the corresponding Fast-Fourier Transform (FFT) pattern (Fig. 5d) generated from the superimposed-line indicated in the image align with standards for the lattice spacing of the ZrN (111) plane.[51]

The diffraction pattern in Fig. 5b also indicates some oxidation evidenced by the broad shoulders of the (111) and (220) peaks. I have observed that exposing ZrN nanoparticles to air at elevated temperatures enhances the presence of this shoulder relative to the cubic ZrN diffraction pattern (Fig. 7). Additionally, in Fig. 5e, a high-

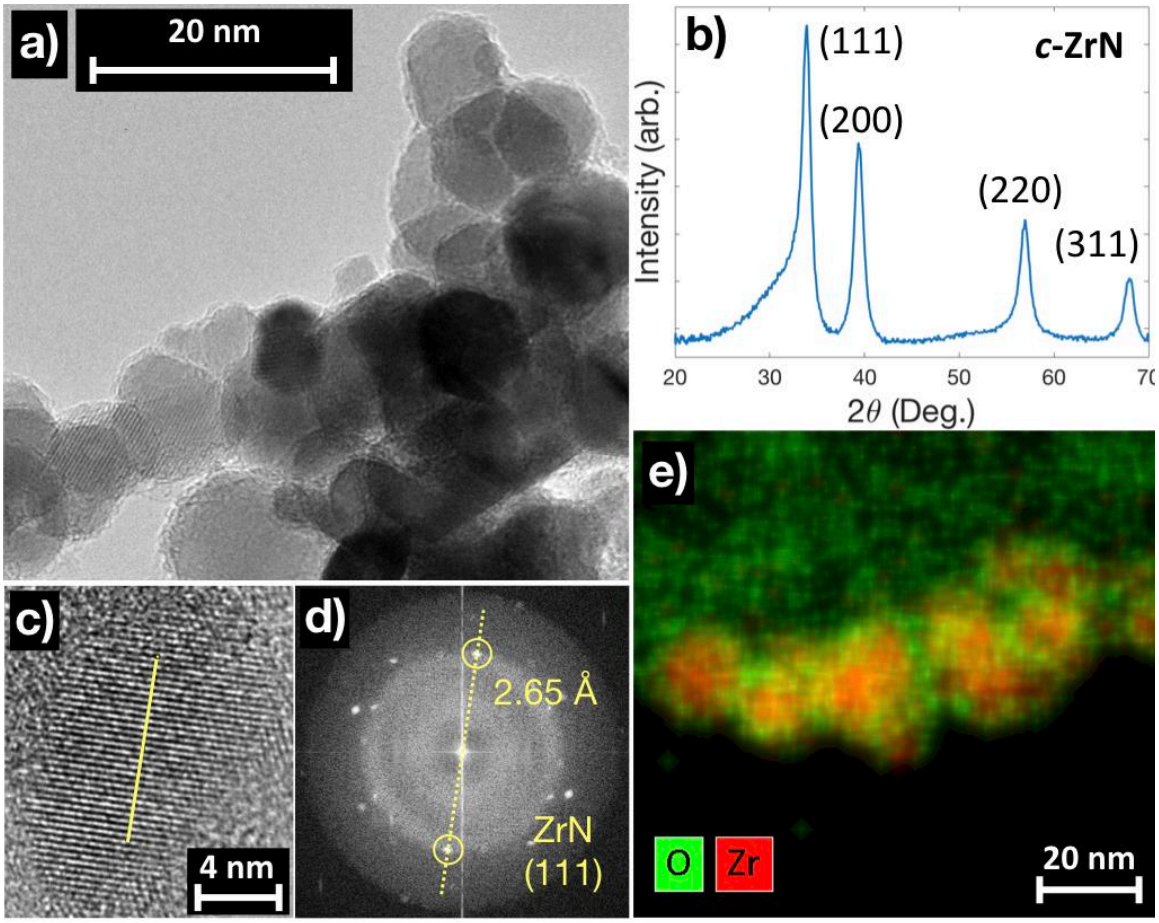

Figure 5: a) TEM image of ZrN particles, b) XRD pattern of produced particles, c) HRTEM image showing crystal plane fringes, d) FFT image showing repeat-spacing from lattice fringes in (c), e) TEM/EDS map showing distribution of elemental oxygen and zirconium in ZrN particles.

resolution EDS map of ZrN particles as-produced from the system shows the distribution of oxygen and zirconium in each particle. Oxygen aggregates at the surface of the particles in a conformal shell around a nitrogen- and zirconium-rich core, which explains the apparent amorphous coating on the surface of the particles seen in Fig. 5a. Additional maps showing elemental distributions of nitrogen, zirconium, and oxygen relative to each other for this sample can be found in Fig. 8. The surface-oxidation evident in Fig. 5 is a

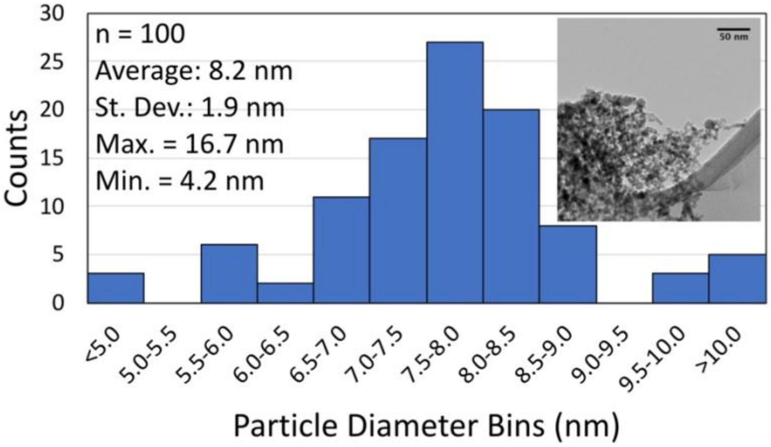

Figure 6: ZrN particle size distribution histogram measured from inset TEM image.

result of exposure to air and cannot be avoided without air-free processing, which is often impractical.

Fig. 9a shows the optical extinction spectrum for the same sample shown in Fig. 5, and the inset shows the deep blue color of the powder and the clear dispersion in DI water. There is a clear peak at 585 nm which I attribute to LSPR in the ZrN

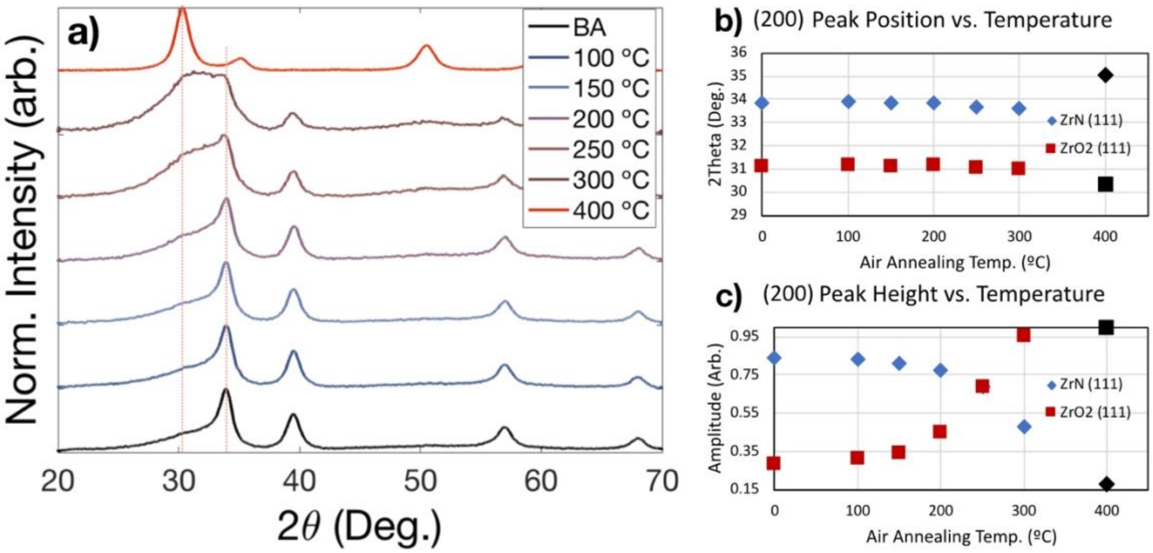

Figure 7: a) XRD patterns of ZrN sample annealed at incrementally increasing temperatures in air, b) Position of (111) peak vs. air annealing temperature, and c) intensity of (111) peak vs. air annealing temperature.

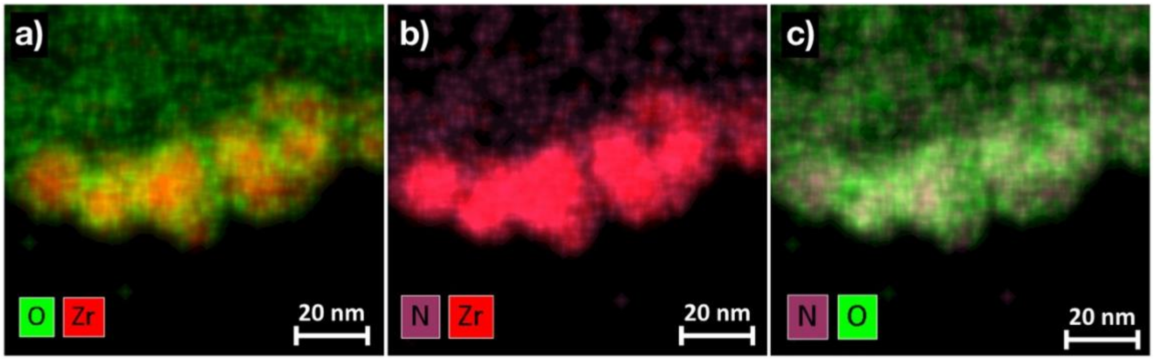

Figure 8: Additional TEM/EDS maps showing atomic distributions of (a) oxygen and zirconium, (b) nitrogen and Zirconium, and (c) nitrogen and oxygen in ZrN nanoparticles

nanoparticles, aligning well with the prior experimental data from Reinholdt *et al.*[29] Repeated spectroscopic measurements on the same sample yield a deviation in the peak position of 3 nm, and the spectrum is repeatable for different samples produced under the same conditions within a deviation of ~20 nm and moderate deviation in the peak intensity and width using the same operating conditions. I consider this to be the optimal material I have produced because it exhibits the highest energy LSPR and most intense peak relative to the UV-absorbance tail. By tuning processing parameters, I can produce material with an apparent LSPR with wavelengths as high as 650 nm, though the peak intensity generally decreases with this red-shift.

Classical Mie theory models of spherical 5 nm ZrN nanoparticles predict a plasmonic extinction peak at 2.60 eV (477 nm) with a half-width of 0.42 eV.[29] In their synthesis of plasmonic ZrN nanoparticles, Reinholdt *et al.* observed similar optical properties to what I observe: an extinction peak at 1.9 eV (653 nm) with a half-width of ~0.8 eV.[29] By extending their model to core-shell Mie theory,[52] Reinholdt *et al.* qualitatively replicated the observed extinction spectra using a system comprised of a ZrN core with a 1 nm thick $ZrN_{0.5}O_{0.5}$ shell.[29] They also showed that with increasing

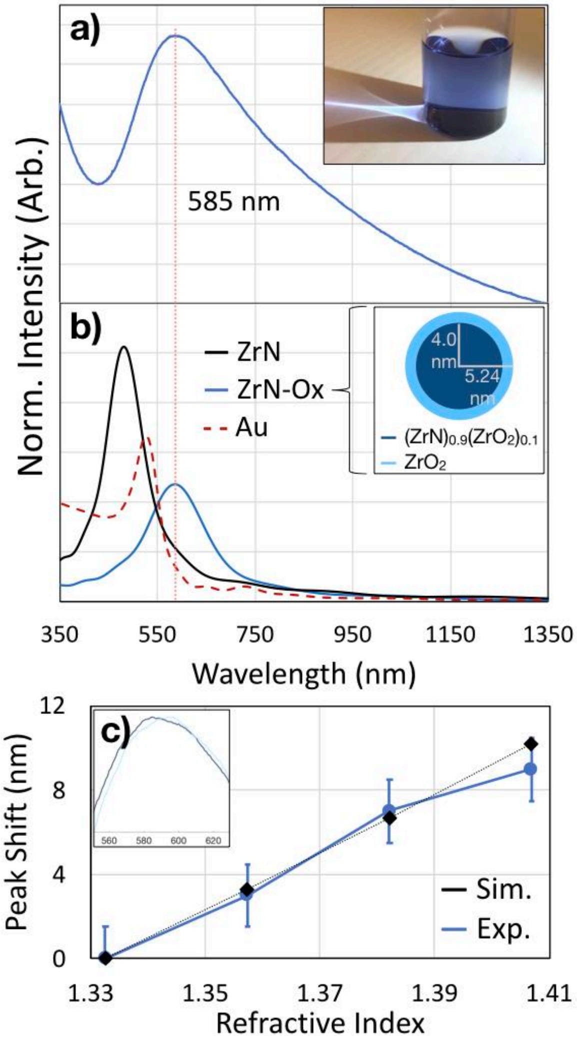

Figure 9: Experimental (a) and simulated (b) optical properties of ZrN nanoparticles. The black curve in (b) corresponds to 5 nm ZrN particles, the dashed red to 5 nm Au particles, and the blue to particles with the oxidation geometry demonstrated in the inset figure. c) Experimental (blue) and simulated (black) measurements of the shift in peak position with an increasing refractive index of the surrounding medium.

oxygen content the high-energy absorption tail in the absorption spectrum increases significantly.[29]

Furthermore, the diffraction pattern observed for all ZrN samples produced in this work exhibit the shoulder adjacent to the ZrN (111) peak as seen in Fig. 5b. I attribute this to the presence of some ZrO_2, though it is difficult to analyze the phase composition quantitatively due to the apparent disordered quality of the oxide phase. In Fig. 7, I demonstrate that after annealing ZrN nanoparticles in air at increasing temperatures, this shoulder grows in intensity relative to the ZrN (111) peak until it becomes fully crystalline ZrO_2 with no signature of the cubic nitride phase remaining. I hypothesize, then, that some degree of oxidation in the ZrN nanoparticles contribute to the red-shifting of the LSPR, following the same conclusion from Reinholdt *et al.*[29]

In Fig. 9b, I provide a comparison of FDTD-simulated optical properties of ideal ZrN nanoparticles (black), oxidized ZrN nanoparticles (blue), and gold nanoparticles (red) for reference (all with radii of 5 nm) against the experimental data from Fig. 9a. While the experimental data does not conform well with that predicted for pure ZrN nanoparticles, I am able to reproduce the observed experimental behavior by modeling a particle with an oxide-structure informed by the data in Fig 5. The experimental data is well-modeled using a core-shell particle structure, in which the core consists of a homogeneous mixture of 90% ZrN and 10% ZrO_2 (making $(ZrN)_{0.9}(ZrO_2)_{0.1}$), and the shell consists of pure ZrO_2. The thickness of the shell is adjusted to account for the volume change of a 1 nm-thick $(ZrN)_{0.9}(ZrO_2)_{0.1}$ shell transforming into pure ZrO_2 assuming no loss of zirconium atoms, yielding a new shell-thickness of 1.24 nm — a schematic of this geometry is shown in the inset to Fig. 9b.

In Fig. 10, I show the elemental composition for five different spots overlapping five particles from the EDS map seen in Fig. 5e. Though the quantification is very imprecise, due to the resolution of the measurement and the overlapping of particles on top of each other in the image, the measured Zr/N atomic ratio ranges from 1.16 to

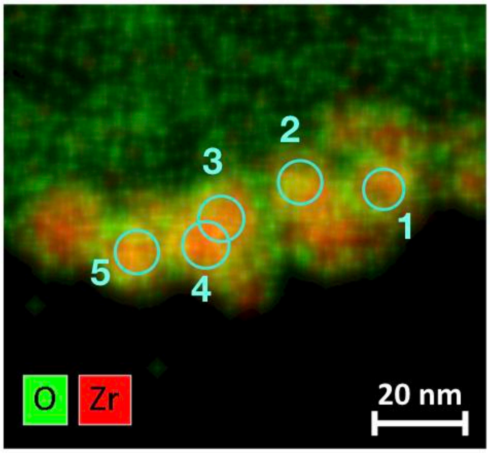

	At. % N	At. % O	At. % Zr	Zr/N
Spot 1	28.86	25.99	45.15	1.56
Spot 2	20.15	44.13	35.72	1.77
Spot 3	17.13	37.53	45.34	2.65
Spot 4	30.85	26.05	43.10	1.40
Spot 5	29.83	35.59	34.58	1.16

Figure 10: TEM/EDS map showing five spots from which elemental composition has been quantified (table on right).

2.65. This composition range also informs the geometry chosen for simulating oxidized ZrN particles. In the geometry indicated by the schematic in Fig. 9b, the Zr/N atomic ratio is 2.02 (at. % Zr = 39.90, at. % N = 19.71, at. % O = 40.39), which sits in the middle of the measured range of compositions.

In order to confirm the plasmonic nature of the extinction peaks shown in Figs. 9a, I have monitored the variation in peak position in solvents with varying refractive index. Mie theory predicts that the surface plasmon energy is sensitive to the refractive index of the surrounding medium.[8] I compare the extinction of particles from one ZrN sample dispersed in graded mixtures of DI water (n = 1.333) and ethylene glycol (n=1.474). The two solvents are miscible, and the refractive index of mixtures of the two solvents trends linearly with the weight fraction of the mixture between that of each pure solvent.[53] Simulations were run using the particle oxidation geometry shown in Fig. 9b with varied medium refractive index surrounding the particle. The experimental samples were all derived from a stock dispersion of ZrN in DI water. For each sample, some of this dispersion was diluted in increasing amounts of ethylene glycol, and the particle mass concentration was adjusted to be constant for each solvent mixture.

A plot showing both the experimental and simulated extinction peak position as a function of refractive index for 0, 25, 50, and 75 wt. % dilutions of ethylene glycol in DI water is shown in Fig. 9c. As expected for a plasmonic material, the extinction peak red-shifts with increasing refractive index. Using precious-metal nanostructures, a shift in peak position down to 1 nm has been correlated with a shift of 6×10^{-3} in refractive index.[54] I observe a weaker dependence for our material — both simulated and experimentally, which I attribute to the dielectric ZrO_2 layer at the surface of the particles.[29] In simulations of ZrN particles with some bulk oxidation but no oxide shell, the peak shift is approximately doubled in magnitude.

In sum, while I do observe LSPR in the ZrN nanoparticles shown here, the behavior is deficient relative to ideal ZrN nanoparticles of the same size. I attribute this discrepancy to oxidation, which I believe is primarily confined in a shell around a plasmonic ZrN core. To improve the plasmonic performance of this material, then, it is necessary to reduce =oxidation. This can be done by conducting completely air-free processing of the material, but I now demonstrate a more practical solution: coating the ZrN nanoparticles with a protective layer.

6.5: Synthesis and Characterization of SiO_xN_y-Coated ZrN Nanoparticles

Following from the extensive work studying oxidation and oxidation-mitigation in ZrN coatings and films,[38] I introduce a protective SiO_xN_y coating on the surface of the

ZrN particles. This is a straightforward addition to the non-thermal plasma system shown in Fig. 1, and the adapted system is shown in Fig. 11. The system remains predominantly the same, but downstream of the plasma reactor and upstream of the filter, I inject a flow of silane (SiH_4) gas at 2% dilution in argon and append an additional 2.5 cm quartz tube with a 2.5 cm-wide copper electrode set 1.3 cm downstream of the vacuum flange. The SiH_4:Ar mixture is injected at 25 sccm (0.5 sccm SiH_4) and second plasma is run at very low power (<10 W) and maintained in a very small volume, to avoid the nucleation of independent silicon nanoparticles.[42] The material is then collected and annealed to remove NH_4Cl contamination in the same manner as is done for un-coated ZrN nanoparticles. For distinction, the silicon-coated particles will henceforth be referred to as ZrN-Si.

Structural and morphological characterization of a representative ZrN-Si sample is shown in Fig. 12. The TEM image in Fig. 12a shows the coating is amorphous and is fairly conformal, with a uniform thickness of 1-2 nm coating all the crystalline ZrN nanoparticles. There is likely some particle agglomeration caused by the introduction of this amorphous matrix around the particles, which will be considered later on in the discussion of the material's optical properties. Fig. 12b shows a high-resolution EDS map

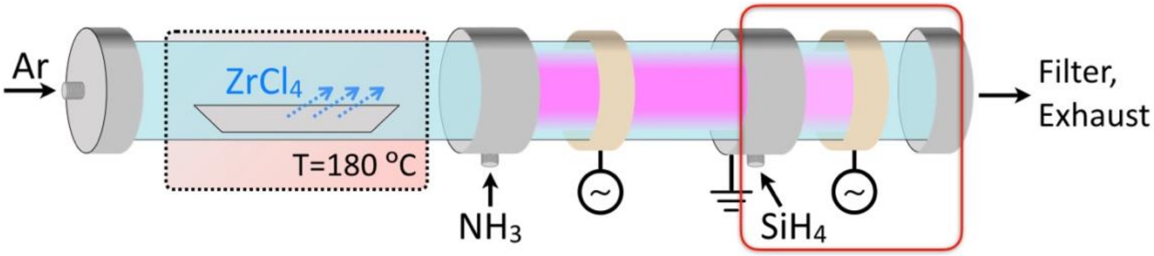

Figure 11: Schematic of non-thermal plasma system used to produce ZrN-Si nanoparticles.

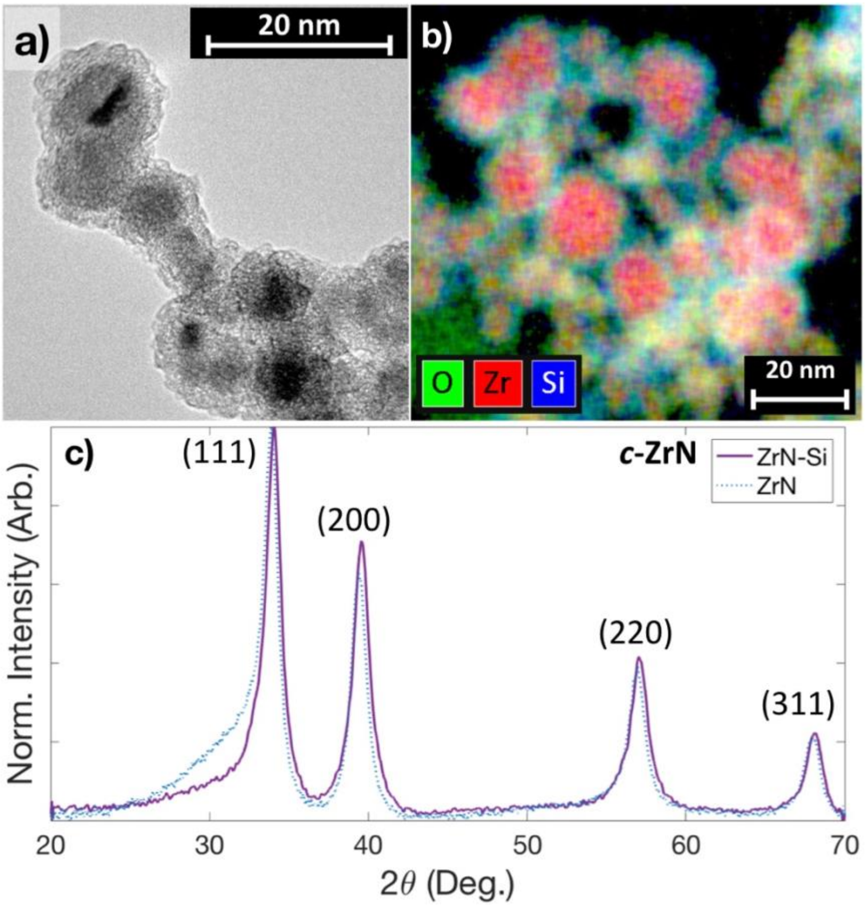

Figure 12: a) TEM micrograph of ZrN-Si nanoparticles. c) STEM-EDS map showing atomic oxygen (green), zirconium (red), and silicon (blue) distribution in a selected group of nanoparticles. c) XRD pattern of ZrN-Si sample (purple) confirming a cubic ZrN structure with no presence of silicon. Data overlaid on pattern for ZrN sample for comparison.

of ZrN-Si particles as-produced from the system shows the distribution of oxygen, zirconium, and in each particle. The map indicates a high concentration of silicon and oxygen surrounding a zirconium core with minimal oxygen and silicon. From prior work studying the interaction of silicon with zirconium nitride thin films, I anticipate no mixing of silicon into the ZrN lattice, and I also anticipate preferential bonding of oxygen with silicon and silicon nitride rather than with zirconium and zirconium nitride.[38]

Additional maps showing distributions of zirconium, nitrogen, oxygen, and silicon on the same spot are included in Fig. 13.

XRD of a ZrN-Si sample (Fig. 12c) confirms that the material is still crystalline ZrN, and there is no contribution from crystalline silicon or silicon nitride. In Fig. 12c, the diffraction pattern from ZrN-Si (solid purple line) is overlaid on a diffraction pattern from a ZrN sample (dashed blue line) for the sake of articulating two things: 1) the crystallite size and lattice parameter is effectively unchanged from the un-coated ZrN sample as indicated by the peak widths and diffraction angles, and 2) the shoulder adjacent to the ZrN (111) peak that I attribute to ZrO_2 is eliminated in the ZrN-Si sample.

In Fig. 14a, the optical extinction spectrum shows the effect this coating has on the plasmonic behavior, and the inset shows the now deep purple color of the powder and

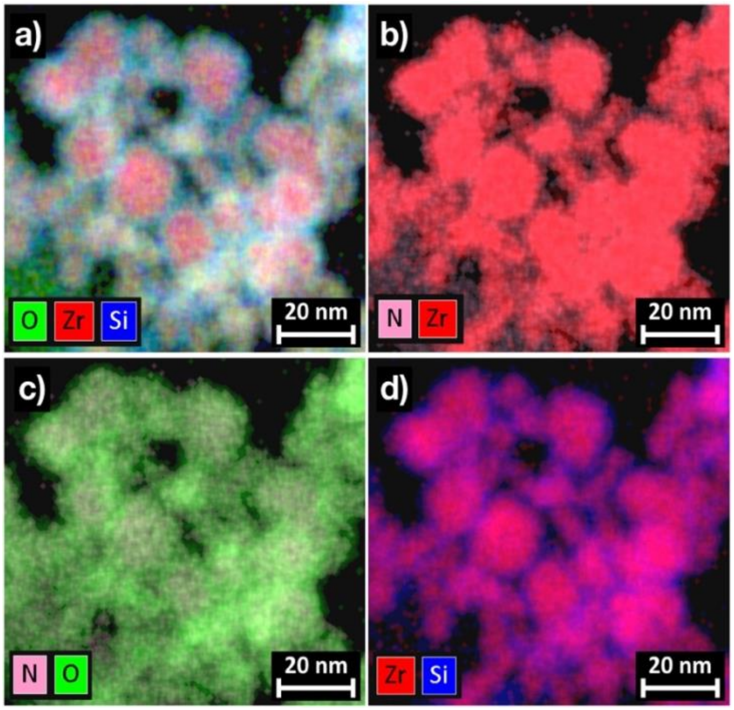

Figure 13: TEM/EDS maps indicating atomic distribution of (a) Zr, O, Si, (b) N, Zr, (c) N, O, and (d) Zr, Si.

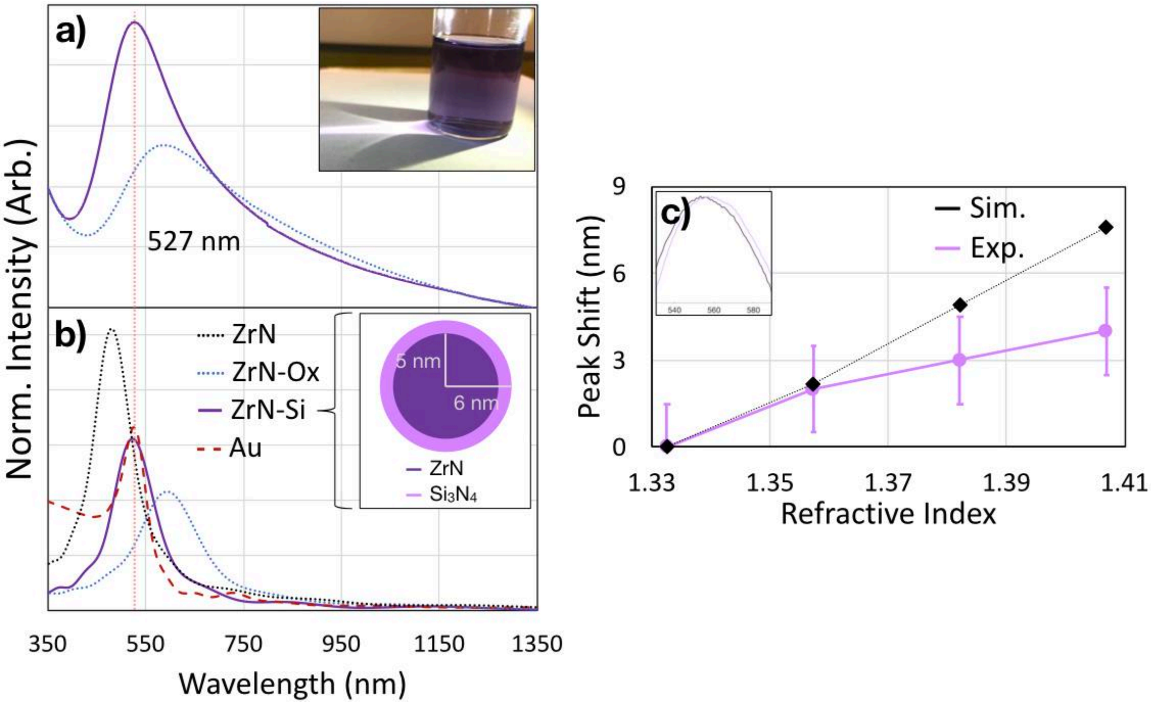

Figure 14: Experimental (a) and simulated (b) optical properties of ZrN-Si nanoparticles (purple lines). In (a), the extinction curve for ZrN is shown (dashed blue line) for comparison. The black curve in (b) corresponds to 5 nm ZrN particles, the dashed red to 5 nm Au particles, blue to particles with the oxidation geometry used in Fig. 9, and purple to ZrN-Si particles with structure demonstrated in the inset figure. c) Experimental (purple) and simulated (black) measurements of the shift in peak position with an increasing refractive index of the surrounding medium.

the clear dispersion in DI water. While I expect the peak to red-shift with the introduction of a high-refractive index medium on the surface of the plasmonic material (n ~ 2.01 for Si_3N_4), the peak is blue-shifted repeatably by 40-60 nm, the intensity is significantly increased, and the peak width is reduced. Again, the ZrN-Si extinction spectrum (solid purple line) is overlaid on the ZrN extinction spectrum (dashed blue line) for comparison, showing the LSPR is evidently improved to be closer to the theoretically predicted behavior with the addition of the coating.

In Fig. 14b, I show FDTD-simulated extinction behavior for ideal ZrN (black), oxidized ZrN with the same geometry used in Fig. 9b (blue), ZrN with a 1 nm Si3N4 shell (purple, schematic inset), and gold (red) for reference. All simulated particles are 5 nm in radius with the exception of the ZrN-Si, in which the ZrN core is 5 nm in radius. The geometry for the simulated ZrN-Si particle is likely not a good facsimile for the experimental reality, because from Figs. 12 and 13 I identify that the shell is amorphous SiO_xN_y, while I are simulating crystalline Si_3N_4. In lieu of precise characterization of the shell composition and corresponding optical constants for said material, I cannot model the system accurately.

A plot showing both the experimental and simulated extinction peak position as a function of refractive index for 0, 25, 50, and 75 wt. % dilutions of ethylene glycol in DI water is shown in Fig. 14c. The extinction peak does red-shift with increasing refractive index, though with a low degree of statistical significance. I observe a much weaker LSPR dependence on the surrounding refractive index for ZrN-Si relative to un-coated ZrN. This may have different causes: 1) the dielectric SiO_xN_y layer reduces the interaction between the plasmonic material and the solvent, and 2) the particles are likely somewhat agglomerated in a network of amorphous SiO_xN_y as is apparent in Fig. 12a. Hence while the LSPR character of ZrN-Si appears more significant than of un-coated ZrN, there remain questions about the effect this coating may have on the "usability" of the plasmonic behavior in real applications.

6.6: Comparison of Oxidation-Effect on LSPR in ZrN and ZrN-Si

Thus far, I have demonstrated the important role oxidation plays in determining the quality of the plasmonic ZrN nanoparticles I produce. Compositionally, I have argued that native oxidation occurs primarily at the surface of ZrN nanoparticles as evidenced by TEM/EDS mapping (Figs. 5e and 8) and FDTD simulations of particles with corresponding core-shell ZrN-ZrO_2 geometries (Fig. 9b). I have also demonstrated that it is possible to inhibit oxidation and improve the LSPR response of ZrN by means of a protective SiO_xN_y coating on the ZrN particles. Being that the ultimate function of the silicon-coating is to reduce oxidation in the plasmonic particles, I now compare the extent to which oxidation detrimentally affects LSRP in coated and un-coated ZrN particles.

Fig. 15a shows Zr 3d peaks from XPS spectra of ZrN and ZrN-Si nanoparticles, and Fig. 15b shows the Si 2p peak from the ZrN-Si sample. The Zr 3d feature is fit with four peaks, accounting for the 3d 5/2 and 3/2 doublets for Zr-O and Zr-N bond energies. The doublet peaks were fit in Origin with a Gaussian profile maintaining a standard 2.43 eV energy difference and a 0.66 peak area ratio between the 5/2 and 3/2 peaks, following

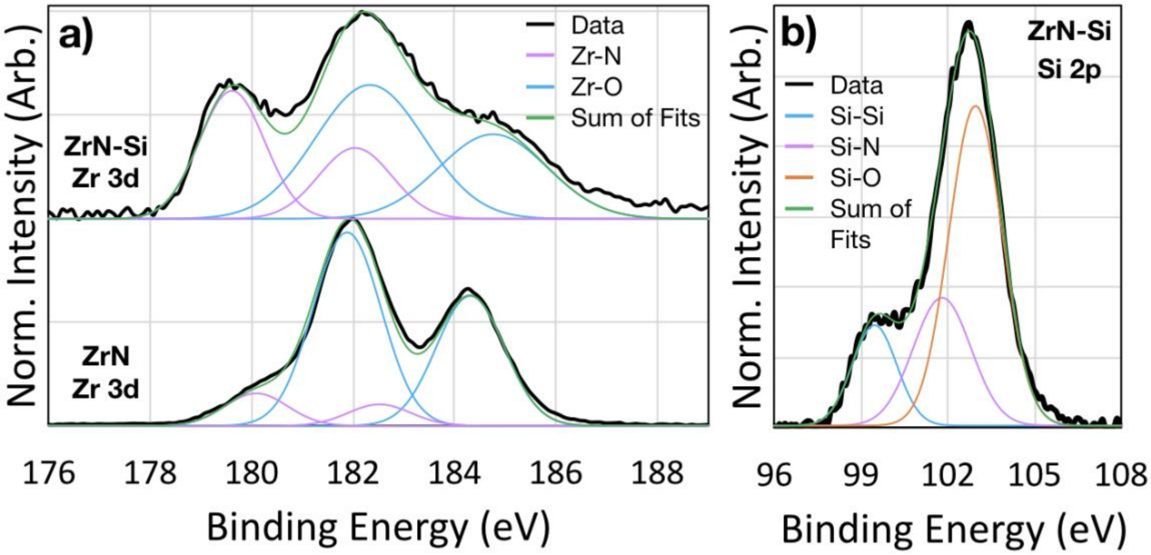

Figure 15: XPS spectra of ZrN and ZrN-Si samples. a) Shows Zr 3d peaks for both ZrN and ZrN-Si samples, with doublet peaks attributed to Zr-N and Zr-O bond energies fit. b) Shows Si 2p peaks for ZrN-Si sample, with peaks attributed to Si-Si, Si-O, and Si-N fit.

the standard procedure as described in prior work.[33] There is significantly less contribution from Zr-O bonds in the ZrN-Si sample relative to the ZrN sample, as indicated by the intensities of the Zr-O peaks (blue curve profiles) relative to the Zr-N peaks (pink curve profiles). The Zr-N peaks in the ZrN sample are also blue-shifted to higher energies than expected from standard values, indicating the bonding structure is likely closer to N-Zr-O rather than N-Zr-N.[33]

The silicon-bonding in the ZrN-Si sample inferred from the fitting of the Si 2p peak supports the conclusions from prior experiments studying silicon incorporation in ZrN coatings and films, namely that silicon preferentially forms covalent Si-N and Si-O bonds[39,55] (pink and orange lines in Fig. 15b, respectively) instead of alloying with the ZrN crystal structure.[38] This, along with diffraction and TEM/EDS studies of ZrN-Si indicates that the coating does not affect the underlying plasmonic ZrN nanocrystal, and is an effective oxidation-passivation technique. With the physical character of the ZrN and ZrN-Si nanoparticles produced by our non-thermal plasma technique well established, the remainder of the paper is a discussion on the plasmonic properties of these materials and a prospectus on the implementation of this material in plasmonics applications.

I conducted a study on the optical properties of coated and un-coated nanoparticles with increasing degrees of oxidation. For this experiment, I started with a large sample of both ZrN and ZrN-Si powder, split the sample into seven parts, and annealed each part at different temperatures in air for one hour. The material was then dispersed in DI water and characterized optically, with the results shown in Fig. 16. For

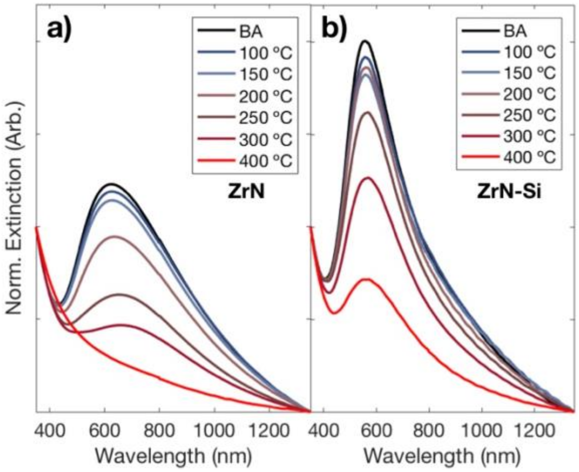

Figure 16: Extinction spectra for ZrN (a) and ZrN-Si (b) particles annealed in air for one hour at increasing temperatures. Spectra are normalized to have a value of "1" at 350 nm. The axes are the same for both (a) and (b) for ease of comparison.

ease of comparison, the spectra were normalized to be "0" at 1350 nm and "1" at 350 nm, and Fig. 16a and 16b are both plotted on the same vertical scales.

Fig. 16a shows the effect of oxidation on optical extinction in un-coated ZrN nanoparticles. The LSPR is relatively stable even after annealing in air at 150 ºC for one hour, but after annealing at higher temperatures the peak is significantly quenched, until it is completely eliminated after annealing at 400 ºC. This sample appears light blue/white and from XRD it appears to be crystalline ZrO_2 (Fig. 7). Fig. 16b shows the same experiment conducted with ZrN-Si nanoparticles. While the initial LSPR for the ZrN-Si particles is already improved from that for ZrN, the LSPR is retained under harsher oxidative conditions as well. In fact, the LSPR in ZrN-Si after annealing in air at 300 ºC for one hour approximates the same response from un-coated ZrN as-produced from the non-thermal plasma system.

Similar results have been observed for the case of TiN nanoparticles, with an increase in the degree of oxidation leading not only to a decrease in the plasmon peak intensity but also to a substantial red-shift in its position.[20] This suggests that there are fine but important differences in the way oxidation affects the optical response of ZrN and TiN nanoparticles, since no major red-shift in peak position is observed for ZrN nor for ZrN-Si. Nevertheless, these nitride nanoparticles are sensitive to oxidation in spite of their being refractory ceramics with very high melting temperatures.

6.7: Conclusions & Implications:

This work is intended to demonstrate the synthesis of ZrN and the characterization of plasmonic activity in the material. I conclude with a summary of our work followed by a short discussion on prospective applications in which this material could be used.

Using a modular and scalable non-thermal plasma system, I have synthesized ZrN nanoparticles. The particles as-produced under what I have determined to be optimal conditions are approximately 8.4 nm in size with a fairly narrow distribution, and they exhibit a cubic-ZrN crystal structure. Upon exposure to air, a thin native-oxide shell develops on the surface of the particles, though the bulk of the particle remains relatively free of oxygen. These particles exhibit LSPR within the visible spectrum at 585-600 nm. Simulations of pure ZrN nanoparticles of approximately the same size exhibit a much higher-energy LSPR, but by simulating a partially oxidized $(ZrN)_{0.9}(ZrO_2)_{0.1}$ core with a ZrO_2 shell, I am able to replicate the performance observed experimentally. The LSPR red-shifts for particles dispersed in incrementally increasing refractive index solvents commensurate with simulations of the partially oxidized particle geometry described above.

Having identified oxidation as a limiting factor to the plasmonic performance of the ZrN nanoparticles, I adapted the non-thermal plasma system to coat the particles in-flight with a conformal amorphous SiO_xN_y shell as an oxidation barrier making ZrN-Si. Structurally, the material produced is still ZrN; no nucleation of independent silicon or silicon nitride particles has been identified. In this material, oxidation is still primarily confined to the surface of the particles, but in the SiO_xN_y coating instead of in the ZrN itself. This material exhibits a substantially improved LSPR that falls much closer to that which is simulated for pure ZrN nanoparticles of the same size. The LSPR feature in this material still red-shifts when dispersed in solvents with increasing refractive index, but to a lesser extent than the uncoated particles. I attribute this in part to the dielectric layer separating the plasmonic material from the surrounding material, and in part to particle agglomeration caused by the coating.

From XPS, I show that the SiO_xN_y coating significantly reduces the relative composition of Zr-O bonds compared to Zr-N bonds at the particle surface. Further, examination of the Si 2p feature in the ZrN-Si sample indicates that silicon does not infiltrate the ZrN crystal lattice as there is no apparent Si-Zr bonding, which is consistent with prior studies on the interaction of silicon with ZrN thin films.

I have also demonstrated the effect increasing oxidation has on the LSPR in ZrN and ZrN-Si by annealing material at increasing temperatures in air for one hour. The uncoated particles show good oxidation resistance up to 200 ºC, but the LSPR is quenched at increased temperatures, and the material is fully oxidized to ZrO_2 after annealing at 400 ºC. The ZrN-Si demonstrates improved oxidation resistance relative to the ZrN, with a plasmonic feature still apparent after annealing at 400 ºC. This indicates the material is a good candidate for plasmonics applications at high temperatures in oxidative environments.

In the introduction, I mentioned various potential applications of transition metal-nitride materials in plasmonics devices. The nanoparticle material I discuss in this work is most suited to thermo-plasmonics applications, because for small particles such as these, the fraction of the extinction spectrum attributable to particle scattering is small relative to that attributable to absorption,[14] which is the case for gold and silver nanoparticles of this size as well. For this particle size, the absorption in ZrN nanoparticles has been predicted to be comparable or even improved to that in gold nanoparticles.[12,14] To understand the viability of this material, it will be necessary in future work to characterize thermal and/or scattering effects of excited plasmonic ZrN and ZrN-Si. I describe a preliminary experiment aimed at characterizing the effect of particle scattering below.

I have attempted to demonstrate the plasmonic enhancement of Raman scattering in Rhodamine 6G (R6G) dye (SigmaAldrich) using ZrN nanoparticles. The excitation of LSPR induces an evanescent electric field which enhances the Raman scattering of surrounding media within its decay length.[56] The enhancement is wavelength dependent and maximized when the laser excitation is in resonance with the plasmon oscillation. In my experiment, I use R6G adsorbed onto the surface of ZrN nanoparticles and excite its response with different laser wavelengths. I then monitor the excitation wavelength dependence in the Raman signal.

SERS measurements were performed using a Horiba LabRam HR Raman spectrometer with a 532 nm and a 785 nm probe wavelength. Additional measurements were performed by E. Aytan (Balandin group, Materials Science & Engineering Program, UCR) on a Renishaw inVia Raman spectrometer in the backscattering configuration with a 633 nm probe wavelength. With the 532 nm and the 785 nm probe lasers, the power used was 5 mW, the spot size was 3 μm, the grating was 600 lines/mm, and the spectra were acquired for 30 seconds with 2 averages. With the 633 nm probe laser, the excitation power was kept below 2 mW. Low powers were maintained to avoid local heating of the sample. Spectra were normalized to the laser power for each excitation energy and vertically offset for comparison. To prepare samples, ZrN nanoparticles were dispersed at a high concentration in methanol and drop-cast onto a cleaned quartz substrate to generate an optically opaque coating. The sample was dried in vacuum for >12 hours to ensure the full evaporation of the dispersing solvent. On the nanoparticle-coated substrate, 50 μL of a 10^{-3} M R6G in methanol solution was drop-cast on the surface and again dried.

The ZrN sample used for this study has peak extinction at 617 nm. Spectra were collected using three different Raman probe wavelengths: 532 nm, 633 nm, and 785 nm. In the inset in Fig. 17 these wavelengths are indicated in relation to the extinction of the ZrN sample. Shown in Fig. 17 are the Raman spectra for the R6G-on-ZrN/Quartz sample

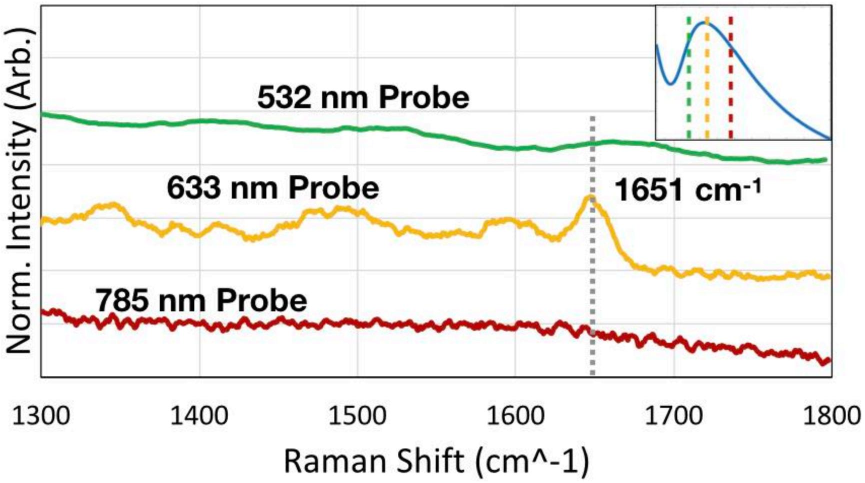

Figure 17: Raman spectra acquired from the same sample (R6G dye drop-cast on optically thick ZrN nanoparticle coating) using three different Raman probe wavelengths. The inset indicates the position between the probe wavelengths and the extinction spectrum for this ZrN sample. The 633 nm probe is near the peak extinction, while the 532 nm and 785 nm probe wavelengths fall on either side of the peak extinction. The spectra are normalized to the laser power and offset for clarity. Comparison of the spectra indicates SERS of the R6G peak at 1651 cm^{-1} using the 633 nm probe, with no enhancement in the spectra collected with the 532 nm or 785 nm probes.

using each of the three Raman probes. The spectra are normalized with respect to laser power to provide a direct comparison of the sensitivity of the measurement at different laser excitation wavelengths. The spectra are also vertically offset for clarity. R6G SERS has been successfully performed using a 532 nm probe laser in the past in spite of the dye fluorescence,[23] so the lack of signal observed here indicates that I am beneath the limit of sensitivity for detection at this probe wavelength. The poor absorbance of R6G at 785 nm leads to a lack of signal at this wavelength. On the other hand, a peak at 1651 cm^{-1} is observed using the 633 nm Raman probe. This peak associated with R6G as the most intense feature at low concentrations in SERS.[57] This is consistent with on-resonance LSPR excitation leading to an enhanced sensitivity of the Raman measurement.

While it is encouraging that I appear to be observing Raman scattering enhancement, which is associated with scattered light from the plasmonic substrate, the enhancement is small. In many of the experiments I conducted, the laser probe would “burn” the sample even with very short exposure time and very low laser power, which is indicative of a strong absorption and photo-heating effect. In future works, I intend to demonstrate the viability of this material as a narrow-band emitter in solar thermo-photovoltaic devices and as a photo-catalyst, applications in which a thermo-plasmonic effect is desirable. In any case, this work highlights a novel synthesis technique that makes future experimental studies on plasmonic ZrN nanoparticles accessible.

6.8: References

(1) Kale, M. J.; Avanesian, T.; Christopher, P. Direct Photocatalysis by Plasmonic Nanostructures. *ACS Catalysis*, **2014**, *4*, 116-128.

(2) Clavero, C. Plasmon-Induced Hot-Electron Generation at Nanoparticle/Metal-Oxide Interfaces for Photovoltaic and Photocatalytic Devices. *Nature Photonics*, **2014**, *8*, 95.

(3) Zhou, Z.; Sakr, E.; Sun, Y.; Bermel, P. Solar Thermophotovoltaics: Reshaping the Solar Spectrum. *Nanophotonics*, **2016**, *5*, 1-21.

(4) Hirsch, L. R.; Stafford, R. J.; Bankson, J. A.; Sershen, S. R.; Rivera, B.; Price, R. E.; Hazle, J. D.; Halas, N. J.; West, J. L. Nanoshell-Mediated Near-Infrared Thermal Therapy of Tumors under Magnetic Resonance Guidance. *Proceedings of the National Academy of Sciences of the United States of America*, **2003**, *100*(23), 13549-13554.

(5) Nie, S.; Emory, S. R. Probing Single Molecules and Single Nanoparticles by Surface-Enhanced Raman Scattering. *Science*, **1997**, *275*, 1102-1106.

(6) Liao, H.; Nehl, C. L.; Hafner, J. H. Biomedical Applications of Plasmon Resonant Metal Nanoparticles. *Nanomedicine*, **2006**, *1*, 201-208.

(7) Lal, S.; Link, S.; Halas, N. J. Nano-Optics from Sensing to Waveguiding. *Nature Photonics*, **2007**, *1*, 641.

(8) Luther, J. M., Jain, P. K., Ewers, T. & Alivisatos, A. P. Localized Surface Plasmon Resonances Arising from Free Carriers in Doped Quantum Dots. *Nature Materials*, **2011**, *10*, 361.

(9) Daniel, M.-C.; Astruc, D. Gold Nanoparticles: Assembly, Supramolecular Chemistry, Quantum-Size-Related Properties, and Applications toward Biology, Catalysis, and Nanotechnology. *Chemical Reviews*, **2004**, *104*, 293-346.

(10) Chan, G. H.; Zhao, J.; Hicks, E. M.; Schatz, G. C.; Van Duyne, R. P. Plasmonic Properties of Copper Nanoparticles Fabricated by Nanosphere Lithography. *Nano Letters*, **2007**, *7*, 1947–1952.

(11) Mock, J. J.; Barbic, M.; Smith, D. R.; Schultz, D. A.; Schultz, S. Shape Effects in Plasmon Resonance of Individual Colloidal Silver Nanoparticles. *Journal of Chemical Physics*, **2002**, *116*, 6755–6759.

(12) Naik, G. V.; Kim, J.; Boltasseva, A. Oxides and Nitrides as Alternative Plasmonic Materials in the Optical Range [Invited]. *Optical Materials Express*, **2011**, *1*, 1090–1099.

(13) Guler, U.; Shalaev, V. M.; Boltasseva, A. Nanoparticle Plasmonics: Going Practical with Transition Metal Nitrides. *Materials Today*, **2015**, *18*, 227–237.

(14) Lalisse, A.; Tessier, G.; Plain, J.; Baffou, G. Plasmonic Efficiencies of Nanoparticles Made of Metal Nitrides (TiN, ZrN) Compared with Gold. *Scientific Reports*, **2016**, *6*, 38647.

(15) Boltasseva, A.; Atwater, H. A. Low-Loss Plasmonic Metamaterials. *Science*, **2011**, *331*, 290–291.

(16) Link, S.; El-Sayed, M. A. Shape and Size Dependence of Radiative, Non-Radiative and Photothermal Properties of Gold Nanocrystals. *International Reviews in Physical Chemistry*, **2000**, *19*(3), 409–453.

(17) Jain, P. K.; Lee, K. S.; El-Sayed, I. H.; El-Sayed, M. A. Calculated Absorption and Scattering Properties of Gold Nanoparticles of Different Size, Shape, and Composition: Applications in Biological Imaging and Biomedicine. *Journal of Physical Chemistry B*, **2006**, *110*(4), 7238–7248.

(18) Kelly, K. L.; Coronado, E.; Zhao, L. L.; Schatz, G. C. The Optical Properties of Metal Nanoparticles: The Influence of Size, Shape, and Dielectric Environment. *Journal of Physical Chemistry B*, **2003**, *107*(3), 668–677.

(19) Guler, U.; Ndukaife, J. C.; Naik, G. V.; Nnanna, A. G. A.; Kildishev, A. V.; Shalaev, V. M.; Boltasseva, A. Local Heating with Lithographically Fabricated Plasmonic Titanium Nitride Nanoparticles. *Nano Letters*, **2013**, *13*(12) 6078–6083.

(20) Alvarez Barragan, A., Ilawe, N. V., Zhong, L., Wong, B. M. & Mangolini, L. A Non-Thermal Plasma Route to Plasmonic TiN Nanoparticles. *Journal of Physical Chemistry C*, **2017**, *121*(4), 2316-2322.

(21) Reinholdt, A.; Pecenka, R.; Pinchuk, A.; Runte, S.; Stepanov, A. L.; Weirich, Th E.; Kreibig, U. Structural, Compositional, Optical and Colorimetric Characterization of TiN-Nanoparticles. *The European Physical Journal D – Atomic, Molecular, Optical and Plasma Physics*, **2004**, *31*(1), 69–76.

(22) Guler, U.; Suslov, S.; Kildishev, A. V.; Boltasseva, A.; Shalaev, V. M. Colloidal Plasmonic Titanium Nitride Nanoparticles: Properties and Applications. *Nanophotonics*, **2015**, *4*(3), 269–276.

(23) Kneipp, K.; Moskovits, M.; Kneipp, H. *Surface-Enhanced Raman Scattering: Physics and Applications*. (Springer Science & Business Media, 2006).

(24) Wang, H.; Chen, Q.; Wen, L.; Song, S.; Hu, X.; Xu, G. Titanium-Nitride-Based Integrated Plasmonic Absorber/Emitter for Solar Thermophotovoltaic Application. *Photonics Research*, **2015**, *3*(6), 329–334.

(25) Govorov, A. O.; Richardson, H. H. Generating Heat with Metal Nanoparticles. *Nano Today*, **2007**, *2*(1), 30–38.

(26) Zhou, N.; Xu, X.; Hammack, A. T.; Stipe, B. C.; Gao, K.; Scholz, W.; Gage, E. C. Plasmonic Near-Field Transducer for Heat-Assisted Magnetic Recording. *Nanophotonics*, **2014**, *3*(3), 141–155.

(27) Guler, U.; Boltasseva, A.; Shalaev, V. M. Refractory Plasmonics. *Science*, **2014**, *344*(6181), 263–264.

(28) Guler, U.; Naik, G. V.; Boltasseva, A.; Shalaev, V. M.; Kildishev, A. V. Performance Analysis of Nitride Alternative Plasmonic Materials for Localized Surface Plasmon Applications. *Appied Physics B*, **2012**, *107*(2), 285–291.

(29) Reinholdt, A.; Detemple, R.; Stepanov, A. L.; Weirich, T. E.; Kreibig, U. Novel Nanoparticle Matter: ZrN-Nanoparticles. *Applied Physics B*, **2003**, *77*(6-7), 681–686.

(30) Schlegel, A.; Wachter, P.; Nickl, J. J.; Lingg, H. Optical Properties of TiN and ZrN. *Journal of Physics C: Solid State Physics*, **1977**, *10*(23), 4889.

(31) Sugunakar Reddy, R.; Kamaraj, M.; Kamachi Mudali, U.; Chakravarthy, S. R.; Sarathi, R. Generation and Characterization of Zirconium Nitride Nanoparticles by Wire Explosion Process. *Ceramics International*, **2012**, *38*(7), 5507–5512.

(32) Van Do, L.; Suematsu, H.; Ogawa, T. Characterization of ZrN, ZrO2 and β'–Zr7O11N2 Nanoparticles Synthesized by Pulsed Wire Discharge. *Journal of the American Ceramic Society*, **2017**, *100*(10), 4884-4892.

(33) Wiame, H.; Centeno, M.-A.; Picard, S.; Bastians, P.; Grange, P. Thermal Oxidation under Oxygen of Zirconium Nitride Studied by XPS, DRIFTS, TG-MS. *Journal of the European Ceramic Society*, **1998**, *18*(9), 1293–1299.

(34) Abadias, G.; Koutsokeras, L. E.; Siozios, A.; Patsalas, P. Stress, Phase Stability and Oxidation Resistance of Ternary Ti–Me–N (Me=Zr, Ta) Hard Coatings. *Thin Solid Films*, **2013**, *538*, 56–70.

(35) Chen, L.; He, L.; Xu, Y.; Zhou, L.; Pei, F.; Du, Y. Influence of ZrN on Oxidation Resistance of Ti–Al–N Coating. *Surface and Coatings Technology*, **2014**, *244*, 87–91.

(36) Wei, R.; Rincon, C.; Langa, E.; Yang, Q. Microstructure and Tribological Performance of Nanocomposite Ti–Si–C–N Coatings Deposited Using Hexamethyldisilazane Precursor. *Journal of Vacuum Science & Technology A*, **2010**, *28*(5), 1126–1132.

(37) Freitas, F. G. R.; Hübler, R.; Soares, G.; Conceição; A. G.; Vitória, E. R.; Carvalho, R. G.; Tentardini, E. K. Structural and Mechanical Properties of Zr-Si-N Thin Films Prepared by Reactive Magnetron Sputtering. *Materials Research*, **2015**, *18*, 30–34.

(38) Saladukhin, I. A.; Abadias, G.; Uglov, V. V.; Zlotski, S. V.; Michel, A.; Janse van Vuuren, A. Thermal Stability and Oxidation Resistance of ZrSiN Nanocomposite and ZrN/SiNx Multilayered Coatings: A Comparative Study. *Surface and Coatings Technology*, **2017**, *332*, 428-439.

(39) Diéguez, L.; Caballero, D.; Calderer, J.; Moreno, M.; Martínez, E.; Samitier, J. Optical Gratings Coated with Thin Si3N4 Layer for Efficient Immunosensing by Optical Waveguide Lightmode Spectroscopy. *Biosensors*, **2012**, *2*(2), 114–126.

(40) Haynes, W. M. *CRC Handbook of Chemistry and Physics, 95th Edition*. (CRC Press, 2014).

(41) Yajima, A.; Segawa, Y.; Matsuzaki, R.; Saeki, Y. Reaction Process of Zirconium Tetrachloride with Ammonia in the Vapor Phase and Properties of the Zirconium Nitride Formed. *Bulletin of the Chemical Society of Japan*, **1983**, *56*(9), 2638–2642.

(42) Mangolini, L., Thimsen, E. & Kortshagen, U. High-Yield Plasma Synthesis of Luminescent Silicon Nanocrystals. *Nano Letters*, **2005**, *5*(4), 655–659.

(43) Lopez, T.; Mangolini, L. Low Activation Energy for the Crystallization of Amorphous Silicon Nanoparticles. *Nanoscale*, **2014**, *6*(3), 1286–1294.

(44) Lopez, T.; Mangolini, L. On the Nucleation and Crystallization of Nanoparticles in Continuous-Flow Nonthermal Plasma Reactors. *Journal of Vacuum Science & Technology B, Nanotechnology and Microelectronics: Materials, Processing, Measurement, and Phenomena*, **2014**, *32*(6), 061802.

(45) Palko, A. A.; Ryon, A. D.; Kuhn, D. W. The Vapor Pressures of Zirconium Tetrachloride and Hafnium Tetrachloride. *Journal of Physical Chemistry*, **1958**, *62*(3), 319-322.

(46) Li, K.; Hogan, N. J.; Kale, M. J.; Halas, N. J.; Nordlander, P.; Christopher, P. Balancing Near-Field Enhancement, Absorption, and Scattering for Effective Antenna–Reactor Plasmonic Photocatalysis. *Nano Letters*, **2017**, *17*(6), 3710-3717.

(47) Philipp, H. R. Optical Properties of Silicon Nitride. *Journal of the Electrochem. Society*, **1973**, *120*(2), 295-300.

(48) Ribbing, C. G.; Roos, A. Zirconium Nitride (ZrN) Hafnium Nitride (HfN). in *Handbook of Optical Constants of Solids* (ed. Palik, E. D.) 351–369 (Academic Press, 1997).

(49) Gittleman, J. I.; Abeles, B. Comparison of the Effective Medium and the Maxwell-Garnett Predictions for the Dielectric Constants of Granular Metals. *Physical Review B*, **1977**, *15*(6), 3273-3275.

(50) Ruppin, R. Validity Range of the Maxwell-Garnett Theory. *Physica Status Solidi B*, **1978**, *87*(2), 619-624.

(51) Chieh, Y.-C.; Lo, W.-Z.; Lu, F.-H. Microstructure Evolution of ZrN Films Annealed in Vacuum. *Surface and Coatings Technology*, **2006**, *200*(10), 3336-3340.

(52) *The Mie Theory - Basics and Applications* | Wolfram Hergert | Springer.

(53) Tsierkezos, N. G.; Molinou, I. E. Thermodynamic Properties of Water + Ethylene Glycol at 283.15, 293.15, 303.15, and 313.15 K. *Journal of Chemical & Engineering Data*, **1998**, *43*(6), 989-993.

(54) Mock, J. J.; Smith, D. R.; Schultz, S. Local Refractive Index Dependence of Plasmon Resonance Spectra from Individual Nanoparticles. *Nano Letters*, **2003**, *3*(4), 485-491.

(55) Ténégal, F. *et al.* Structural Determination of Sintered Si3N4/SiC Nanocomposite Using the XPS Differential Charge Effect. *Journal of Electron Spectroscopy and Related Phenomena*, **2000**, *109*(3), 241-248.

(56) Pérez-Juste, J., Pastoriza-Santos, I., Liz-Marzán, L. M. & Mulvaney, P. Gold Nanorods: Synthesis, Characterization and Applications. *Coordination Chemistry Reviews*, **2005**, *249*(17), 1870-1901.

(57) Dong, Z.; Wei, H.; Chen, Y.; Wang, R.; Zhao, J.; Lin, J.; Bu, J.; Wei, Y.; Cui, Y.; Yu, Y. Surface Enhanced Raman Scattering Activity of TiN Thin Film Prepared via Nitridation of Sol-Gel Derived TiO_2 Film. In *9672*, 967209 (International Society for Optics and Photonics, 2015).

7: Conclusions & Prospectus

In this dissertation, I have demonstrated novel methods of synthesis, control, and characterization of YSZ, CZTS, and ZrN nanoparticles. I have focused primarily, though, on the fundamental chemistry and materials science associated with characterizing these materials for proposed applications. In this chapter, I comment on the commercial viability of each of these materials and their respective synthesis techniques.

In the project related to the synthesis of YSZ nanoparticles, the material was chosen because it has already proven to be effective in the proposed application, the "window to the brain." The ultimate challenge in this project has been to take a technique that already works — *i.e.* the sintering of commercially-supplied 8-YSZ nanoparticles into semi-transparent disks — and improve it by improving the basis nanoparticle matter. In Ch. 2, I demonstrated my spray pyrolysis technique used to produce YSZ nanoparticles. The technique not only makes it possible to produce material with controlled size and crystalline phase, but also to produce material at a large scale to facilitate expedient development of an optimized sintering process and, eventually, the commercial production of transparent YSZ disks sintered from these nanoparticles.

In Ch. 3-5, I discuss the processing of CZTS into uniform large crystal grain thin films for use as absorber layers in thin film photovoltaics. In this project, the material was chosen because it demonstrated theoretical promise as an alternative material that, if optimized, could lead to the eventual large-scale, low-cost implementation of photovoltaics in the United States electrical grid. In the past few years, though, other technologies and material systems have developed quickly while CZTS has stagnated, and a majority of CZTS research has now transitioned elsewhere. The main reason for this is that CZTS is an highly complex material system, and its structural, morphological, and electrical properties are difficult to control. In Ch. 3 and 4, I demonstrated that of the many thin film processing techniques we and other groups have experimented with, there is inevitably structural and compositional inhomogeneity in the product. Further, the techniques I have developed to produce uniform large grain films from nanoparticle coatings involve the addition of further complexity by means of dopants or a diffusion-passivating layer. While I contend that my techniques are readily scalable, any PV product would be inefficient and uncompetitive in the market.

Instead, I see this and other work with CZTS as a fundamental materials science exploration that will inform the development of complex electronic materials in the future. Up to now, as referenced in Ch. 1, much of the research and development in electronics and miniaturization has entailed optimization of device geometries and synthesis techniques. But with silicon-based transistors reaching a minimum possible size and new three-dimensional geometries maximizing space utilization on transistor chips, there are two paths forward for continued development. The first is in the development of entirely new paradigms of data storage and management. Some examples of these are quantum computers, in which data is stored at the sub-atomic scale in electron/quark spin state as opposed to the standard binary “ON” and “OFF” voltage cutoffs, and neural networks, which are inspired by the complexity and relative efficiency of the human brain. In the second path, new material systems can be developed that are more efficient than the commonly-used silicon- or gallium arsenide-based devices. These are very simple materials from a chemical standpoint, which makes them easy to work with and to mass-produce. Over time, however, it may become fiscally efficient to optimize these materials electronically by the incorporation of alloyed, multi-phase, or heaviliy doped materials. In this regard, CZTS may serve as an early case-study in the development and optimization of highly complex material systems. Techniques like the *in situ* Raman I demonstrated in Ch. 5 will be necessary in the early stage development of these material systems.

In Ch. 6, I discuss the synthesis of plasmonic ZrN nanoparticles. This project is centered on a material in early stage research, and is only the second successful demonstration of the production of plasmonic ZrN nanoparticles. The plasmonic properties in this material system have been discussed somewhat extensively on a theoretical basis, but experimental research on the system has been scant. With the advent of the non-thermal process outlined here, more extensive work studying the behavior and properties of plasmonic ZrN nanoparticles is attainable. As a prime example, our work demonstrates that oxidation is among the most significant factors to control experimentally in order to produce material with a significant plasmonic response, though this has been discussed little in prior theoretical works. In our group, we now seek to develop an extensive body of work demonstrating the viability of this material in various applications in which gold or silver nanoparticles are used now, as well as developing further understanding of how to control and optimize the material chemistry.